Spring 5-15-2022

Mechanisms of Voltage-Gated Sodium Channel (NaV1.5) Regulation by Intracellular FGFs

Paweorn Angsutararux
Washington University in St. Louis

WASHINGTON UNIVERSITY IN ST. LOUIS

McKelvey School of Engineering
Department of Biomedical Engineering

Dissertation Examination Committee:
Jonathan R. Silva, Chair
Jianmin Cui
Matthew Lew
Jeanne Nerbonne
Janice Robertson

Mechanisms of Voltage-Gated Sodium Channel ($Na_V1.5$) Regulation by Intracellular FGFs

by

Paweorn Angsutararux

A dissertation presented to The Graduate School
of Washington University in partial fulfillment of the
requirements for the degree of
Doctor of Philosophy

May 2022
St. Louis, Missouri

Table of Contents

List of Figures

List of Tables

Acknowledgments

I would like to thank my mentor Professor Jonathan Silva for his guidance and support throughout the end. I am grateful for the freedom you allowed me to explore on my project. Your optimism gives me confidence to try things without worrying too much. You always give me ideas and push me to become a better scientist. Thank you for being a wonderful mentor.

I would like to thank our collaborators, Dr. Jeanne Nerbonne and Dr. Amal Dutta for their fantastic mice works that are great complementary to my results. Their knowledge and expertise related to the topics of my thesis help guide me along the way and make my work more complete. I'm very grateful for your time and help. I also would like to thank Dr. David Ornitz for all wonderful ideas and suggestions he provided.

I want to thank all my committee members, Dr. Jianmin Cui, whose questioning led me to deeper understanding of my projects. Thank you for your thorough examination. Thank you, Dr. Matthew Lew and Dr. Janice Robertson who lend me expertise in the field of fluorescence imaging, to help improve my work. I received a lot of great advice and guidance that I'm truly appreciated.

I would like to thank the molecular team, our previous lab technicians, Taylor and Lily, and our current members Jingyi, Martina and Carlota for the help on making mutations and RNA. Thank you, Thao, for taking care of the cell culture for me.

I want to thank all my friends, previous and current lab members that make my time in the lab joyful. Thank you for the good memories we shared together. I'd like to give special thanks to Wandi and Billy. Wandi, who taught me a lot of techniques in the lab always give me ideas and is open to discussion even when she embarked on the new journey. Billy, thanks for working together on the FRET project. I wouldn't be able to complete this without your contribution. All the ideas you put forward and discussions we had are very helpful. Thank you, Kate, Emily, Lucy, Druv, Khrystyna, Guohui, Lulu, and Shashi for the wonderful friendship.

Finally, I would like to thank my family, my parents and my sister. It's been a long time since I've not seen them. I missed them a lot. Thank you for always being there for me and supporting me through this journey. You make being alone not feeling lonely here.

Paweorn (Eve) Angsutararux

Washington University in St. Louis

May 2022

This thesis is dedicated to my grandparents who passed away.

ABSTRACT OF THE DISSERTATION

Mechanisms of Voltage-Gated Sodium Channel ($Na_V1.5$) Regulation by Intracellular FGFs

by

Paweorn Angsutararux

Doctor of Philosophy in Biomedical Engineering

Washington University in St. Louis, 2022

Professor Jonathan R. Silva, Chair

Voltage-gated sodium channels (Na_V) conduct the inward current responsible for the initiation and propagation of the electrical signals in myocytes and neurons, known as action potentials (AP). Precise regulation of cardiac $Na_V1.5$ opening and closing is essential for maintaining a normal heart beat. A disruption of $Na_V1.5$ function, especially of its inactivation after opening, results in inherited cardiac arrhythmias such as Long QT Type 3 (LQT3) syndrome. This pathology is caused by an increase in the late I_{Na} that enters myocytes later in the AP and prolongs its duration. Late I_{Na} is also enhanced in acquired diseases such as heart failure (HF). Na_V channels are regulated by many auxiliary subunits, including intracellular Fibroblast Growth Factors (iFGFs). Each iFGF gene encodes multiple different isoforms, varying in their N-terminal sequences. The interaction between and regulation of iFGF and Na_V channels is isoform specific.

In this dissertation, I investigated the modulation of cardiac $Na_V1.5$ channels by iFGFs that are highly expressed in human and mouse hearts (FGF12B and FGF13VY). I discovered how the different iFGFs control $Na_V1.5$ voltage sensing and then modulate Na_V channel inactivation differently. I also demonstrated that FGF12A, which is upregulated in patients with HF, can convey

therapeutic benefits by inhibiting late I_{Na}. This result provides new insight into how differential expression of iFGF isoforms can modulate the adverse pharmacological responses that are observed in HF patients prescribed with anti-arrhythmic drugs. Lastly, I present a newly developed tool for studying inactivation dynamics and the interplay between the different components of Na_V channel involved in its inactivation, allowing deeper insight into this essential regulatory mechanism.

Chapter 1: Introduction

1.1 Cardiac electrical activity

The heart is an electrical organ that pumps blood throughout the body. Its function is regulated through coordinated electrical signals that drive synchronous contractions of the atria and the ventricles in a timely manner. The electrical impulse is generated by pacemaker cells in the sinoatrial (SA) node and propagates through the atrial and ventricular chambers (Nerbonne & Kass, 2005). An excitation of an individual myocyte results in an action potential (AP), which reflects the sequential activation and inactivation of multiple ion channels (Zipes et al., 2017). The waveform of AP varies within cardiac regions, as a result of different underlying ionic currents.

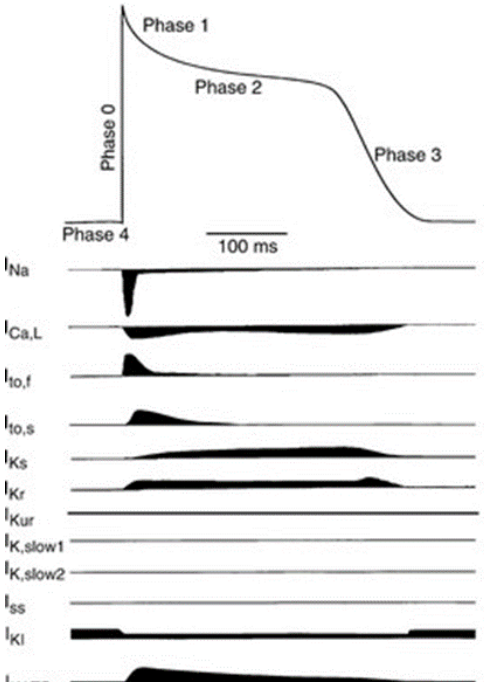

Figure 1.1: Ventricular AP and underlying ionic currents (Adopted from Nerbonne & Kass, 2005).

For ventricular myocytes **(Fig 1.1)**, during the upstroke of an AP, or phase 0, an activation of the voltage-gated sodium channel (Na_V) leads to a large inward current (I_{Na}) that depolarizes the membrane potential. Subsequent activation of the fast transient voltage-gated outward K^+ current (I_{to}) causes a transient repolarization in phase 1, seen as the AP notch. The activation of voltage-gated Ca^{2+} channels (Ca_V) by membrane depolarization facilitates Ca^{2+} influx during phase 2 plateau. This increase in intracellular Ca^{2+} is the main trigger of myocyte contraction. In the last phase of AP (phase 3), two predominant K^+ outward currents (I_{Ks} and I_{Kr}) repolarize the membrane potential to its resting value and terminates an AP. A proper regulation of these ion channels enables the rapid AP

propagation to maintain normal cardiac rhythms. Any disruption to this elaborated process can result in life-threatening arrhythmias.

1.2 Pathogenic late I_{Na}

Na_V channel fast inactivation happens within a few milliseconds after its activation and limits the amount of late I_{Na} that persists over long depolarization (Ulbricht, 2005). In a normal heart, the late I_{Na} presents only about 0.01 - 1% of the peak I_{Na} during an AP plateau phase (Antzelevitch & Nesterenko, 2014). An increase in the late I_{Na} leads to an AP prolongation and a dispersion of repolarization. Both are the substrate for early afterdepolarization (EAD) and predispose the heart to deadly arrhythmias. Increased intracellular Na^+ also reverses the mode of sodium calcium exchanger (NCX), from Ca^{2+} efflux to Ca^{2+} influx, leading to elevated intracellular Ca^{2+} or Ca^{2+} overload. As a result, there are more spontaneous Ca^{2+} releases from sarcoplasmic reticulum during diastole (a period of heart relaxation), which lead to more incidents of delayed afterdepolarization (DAD), another common cause of arrhythmias.

Increased late I_{Na} is a well-known pathogenic mechanism underlying many inherited and acquired diseased conditions. Some examples are discussed below.

1.2.1 Congenital long QT type 3 syndrome

An inherited cardiac arrhythmia that exhibits a prolonged QT interval in ECG recording is known as long QT (LQT) syndrome. LQT syndrome type 3 (LQT3) is often associated with the gain-of-function mutations in Na_V channels and proteins associated with its regulation. The mutations often impair Na_V fast inactivation and cause elevated late I_{Na}, either by delaying the fast inactivation kinetics or promoting the channel reopening after inactivation. The treatment with specific late I_{Na} inhibitors is often successful in preventing arrhythmias.

1.2.2 Heart failure

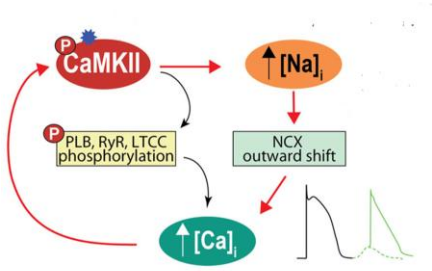

Figure 1.2: A positive feedback loop between late INa ([Na]) and CaMKII activation (Adapted from Grandi & Herren, 2014).

Heart Failure (HF) is a condition where the heart fails to pump blood efficiently. It is characterized by abnormalities in cardiac rhythm and contraction. An increase in late I_{Na} is an important mechanism contributing to diseased pathophysiology (Maltsev & Undrovinas, 2008). The likely cause of late I_{Na} is an increase in Na_V channel late openings, that can be triggered by multiple conditions such as an increase in oxidative stress, an elevated intracellular Ca^{2+} and the activation of protein kinases CaMKII. A positive feedback loop has been identified **(Fig 1.2)**. Increased late I_{Na} contributes to the high cellular Na^+ concentrations, which cause Ca^{2+} overload, leading to CaMKII activation. CaMKII then modulates Na_V channel resulting in further increase in late I_{Na}. The interruption of this feedback loop, either by reducing late I_{Na} or inhibiting CaMKII activation, shows the improved cardiac function in HF animal models. However, clinical results are less successful in reversing the end-condition such as death, myocardial infarction, and recurrent ischemia (Morrow et al., 2007).

1.3 Voltage-gated sodium channel

Na_V channels are macromolecular complexes that consist of primary α-subunits and several auxiliary subunits (de Lera Ruiz & Kraus, 2015). Humans have 9 different Na_V α-subunits ($Na_V1.1$-1.9), transcribed from genes *SCN1A*-*SCN9A*. Each Na_V subtype shows distinct gating kinetics and functional properties (Goldin, 2001). The expressions of Na_V subtypes also vary in different tissue. In the heart, $Na_V1.5$ is the predominant Na_V channel.

1.3.1 Structure of Na_V α-subunit

Mammalian Na_V α-subunit is transcribed as a single polypeptide with more than 2000 amino acids. Na_V α-

subunit is a pseudo-tetrameric protein that consists of 4 homologous repeats (I-IV) (Yu and Catterall, 2003). Each repeat contains 6 membrane segments (S1-S6). The following section will cover the important domains of a Na_V α-subunit **(Fig 1.3)**.

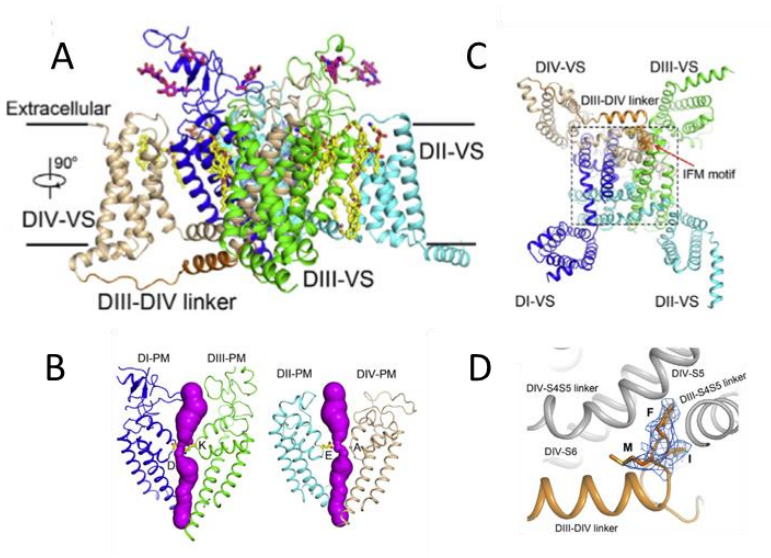

Figure 1.3: Cryo-EM structure of rat $Na_V1.5$ (Adapted from Jiang et al., 2020).
(A) Illustration of overall $Na_V1.5$ structure, showing VSD-I to VSD-IV and III-IV linker or the inactivation gate. **(B)** Structure of the pore module (PM) that forms channel central pore and ion selectivity filter (SF) bearing DEKA ring. **(C)** Bottom view of intracellular activation gate (in square) shows the IFMT motif binding to allosterically block the pore. **(D)** The IFMT motif binding to its receptor.

Voltage sensor domain

Helical segments S1-S4 from each repeat constitute the voltage sensor domain (VSD), an important module that enables Na_V channel to sense the change in membrane potential. On segment S4, every third position has a positively charged residue, usually either Arginine (R) and Lysine (K), which are also called *gating charges*. In a sliding helix or helical screw model, gating charges are held at negative resting membrane potentials by negatively charged residues in S1, S2 and/or S3 segments. Upon membrane depolarization or the change in membrane potential toward positive values, gating charges are transferred across the membrane from the intracellular to the extracellular side, across the hydrophobic constriction site (HCS). The outward displacement of the S4 helix is mediated by ion-pair interaction with countercharges in other segments of the VSD (Catterall et al., 2017). Though homologous, each VSD is distinct in its sequences and hence its activation kinetic. All VSDs, however, are highly coupled and work cooperatively to control Na_V channel gating.

Pore Module (PM)

The pore module (PM) is formed by S5, S6 segments and the connecting pore-loop (P-loop). It is arranged

next to the peripheral VSD in a domain-swapped architect. The VSD of one repeat is close to the PM of another. Together, PMs from all 4 repeats make the Na_V channel central pore. The inner selectivity filter (SF) is the narrowest part of the pore formed by P-loop. It contains 4 amino acids, aspartate (D), glutamate (E), lysine (K), and alanine (A) from repeat I-IV accordingly. This DEKA ring confers the channel selectivity to Na^+ ion by facilitating specific binding of hydrated Na^+ ions.

Activation gate

At the intracellular boundary of the channel pore, hydrophobic residues from the intracellular ends of S6 segments form a bundle crossing known as the activation gate. The activations of VSDs are propagated via an S4-S5 linker to cause conformational changes in S6 segments, leading to an opening of the activation gate in an iris-like dilation manner.

Inactivation gate

The fast inactivation gate is located in the intracellular linker between repeats III and IV (III-IV linker) (Smith and Goldin, 1997). The key hydrophobic IFMT motif plugs into the corner of the activation gate and causes an allosteric pore block (Pan et al., 2018). The IFMT binding site encompasses the S6 segment and the S4-S5 linkers of repeats III and IV. Extensive interactions were established along the III-IV helix with the S4-S5 of repeat IV.

C-terminal domain

The Na_V C-terminal domain (CTD) is the region following the S6 segment of repeat IV. The CTD consists of 6 α-helices, separated into two main domains: the proximal EF hand-like structure and the distal IQ motif, resembling a lollipop. The EF-like domain consists of α1- α5 and is the binding site of intracellular fibroblast growth factor (iFGF), whereas the IQ motif (α6) serves as the interaction site of Calmodulin (CaM). These two proteins, iFGF and CaM, are important Na_V channel auxiliary subunits that we will discuss later.

1.3.2 Na_V channel gating

Upon membrane depolarization, the VSD activation leads to conformational changes around the intracellular activation gate. Specifically, in human $Na_V1.5$, the activations of VSD-I, II and III lead to channel gate opening (Chanda and Bezanilla, 2002) (Varga et al., 2015). The activation of VSD-IV occurs slightly later to initiate the Na_V channel fast inactivation (Capes et al., 2013) (Goldschen-Ohm et al., 2013). The binding of IFMT motif to its receptor allosterically constricts the intracellular gate and limits Na^+ ions conductance. The interactions along the III-IV linker and the CTD stabilize an inactivation conformation (Deschenes et al., 2001) (Mantegazza et al., 2001) (Motoike et al., 2004). The unbinding of the IFMT motif, and the deactivation of the VSD-III and VSD-IV determine the recovery from inactivation (Cha et al., 1999) (Hsu et al., 2017). This open-state inactivation is crucial for controlling an AP duration. Until Na_V channels recover from an inactivation, they cannot be activated repeatedly.

Apart from an open-state inactivation, at hyperpolarized potentials, channels can inactivate directly from the closed-state conformation (Aldrich and Stevens, 1983) (Bean, 1981). This closed-state inactivation results in a smaller number of channels available to open, which can be measured as a steady-state inactivation (SSI) curve. The voltage-dependence of activation (G-V) curve measures the channel conductance at varying potentials. The overlap of these two curves presents the window current, or the fraction of channels that conducts I_{Na}.

1.4 Na_V auxiliary subunits

The Na_V α-subunit is regulated by multiple auxiliary subunits including β-subunit, Calmodulin, and intracellular fibroblast growth factor (iFGF) (Abriel, 2010).

1.4.1 β-subunits

The Na_V β subunits can regulate the Na_V channel function through multiple mechanisms, including the modulation of Na_V channel expression at the cell membrane, the alteration of Na_V channel kinetics, the mediation of cell adhesion, and the recruitment of cytosolic proteins (Calhoun and Isom, 2014). In humans, there are 5 isoforms of Na_V β-subunits (β1 – β4 and β1b), encoded by *SCN1B-SCN4B* (Winters and Isom, 2016). All β1-β4 subunits share the same topology with an extracellular N-terminal immunoglobulin (Ig) domain, a transmembrane segment, and an intracellular C-terminus. The β1b subunit contains only the N-terminal domain. The β2 and β4 subunits interact with Na_V α-subunit through covalent disulfide bonds, whereas β1 and β3 subunits interact with α-subunit non-covalently. In the human heart, the most abundant isoform is the β1 subunit. Other β isoforms have distinct subcellular localization with differential expression profiles over embryonic development.

1.4.2 Calmodulin

Calmodulin (CaM) is a Ca^{2+}-sensing protein consisting of two globular domains, N- and C-lobes. Each lobe contains 2 EF-hand motifs, responsible for Ca^{2+} binding. The binding of Ca^{2+} often leads to a change in CaM conformation, rendering CaM a candidate that regulates Ca^{2+}-dependent change in Na_V channel inactivation. These features, however, are debatable and multiple studies show opposing results. Under elevated Ca^{2+} concentration, CaM was reported to cause a depolarizing shift in SSI (Gabelli et al, 2016), possibly by facilitating recovery from inactivation (Johnson et al., 2018). Because of the complexity of CaM regulation that likely involves various facets of Na_V channels, its regulatory mechanisms remain unclear (Armstrong and Cota, 1991) (Kim et al., 2004).

Multiple models of CaM modulation of Na_V channel function were proposed based upon available structures of CaM under different conditions (i.e. high vs low Ca^{2+} concentration, the presence vs the absence of iFGF, etc.) (Pitt & Lee, 2016). A leading model proposed that CaM will interact with the Na_V III-IV linker under elevated Ca^{2+} concentration (Sarhan et al., 2012) (Gabelli et al., 2014) (Chogot et al., 2011). Usually within $Na_V1.5$, CaM binds to the IQ motif with high affinity under low Ca^{2+} conditions (Wang, 2012). An increase in

Ca^{2+} lowers the CaM binding affinities on the CTD, while raising its affinity towards the III-IV linker, potentially affecting the inactivation gate binding during Na_V inactivation.

$Na_V1.5$ mutations on the CTD that reduce CaM binding affinities were found in patients with inherited arrhythmias such as LQT3 and BrS (Liu et al., 2003) (Musa et al., 2015) (Hennessey et al., 2013). These mutations were associated with increased late I_{Na}, supporting the notion of CaM modulation of Na_V channel inactivation.

1.4.3 Intracellular Fibroblast Growth Factor

Intracellular fibroblast growth factors (iFGFs), also known as fibroblast growth factor homologous factors (FHFs), are a subfamily of the FGFs (Goldfarb, 2005). iFGFs consist of FGF11-FGF14 and share high similarities in sequences with other FGFs in the core domain. The lack of secretory signal sequences makes iFGF non-secreted. Studies have shown that iFGFs play a significant role in the regulation of Na_V channel function. Each iFGF gene can be transcribed into two or more isoforms, differing in the N-terminus. The regulation of Na_V channels is specific to both Na_V and iFGF isoforms. The expression of iFGFs also varies across different tissues. A mutation in FGF12B, which is highly expressed in the human heart, is linked to cardiac arrhythmia (Hennessey et al., 2013). A $Na_V1.5$ variant that affect the iFGF binding affinity also shows altered gating kinetics (Musa et al., 2015). So far, the regulatory mechanism of iFGF remains elusive, especially how different iFGFs cause differential modulatory effects.

1.5 References

Abriel, H. 2010. Cardiac sodium channel Na(v)1.5 and interacting proteins: physiology and pathophysiology. *J Mol Cell Cardiol.* 48:2–11. doi: 10.1016/j.yjmcc.2009.08.025

Antzelevitch, C., and Nesterenko, V. 2014. The role of late INa in development of cardiac arrhythmias. *Handb Exp Pharmacol*. 221:137-168.

Aldrich, R.W., Corey, D.P., and Stevens, C.F. (1983). A reinterpretation of mammalian sodium channel gating based on single channel recording. Nature. 303, 436-441. http://doi.org/10.1038/306436a0.

Armstrong C. M., and Cota G. 1991. Calcium ion as a cofactor in Na channel gating. *Proc Nat Acad Sci.* 88(15):6528-31.

Bean, B.P. 1981. Sodium channel inactivation in the crayfish giant axon. Must channels open before inactivating? *Biophys. J*. 35:595–614. doi:10.1016/S0006-3495(81)84815-1

Calhoun, J.D., and Isom, L.L. (2014). The role of non-pore-forming β subunits in physiology and pathophysiology of voltage-gated sodium channels. Hand. Exp. Pharmacol. 221, 51-89. http://doi.org/10.1007/978-3-642-41588-3_4.

Capes, D.L., Goldschen-Ohm, M.P., Arcisio-Miranda,M., Bezanilla, F., and Chanda, B. 2013. Domain IV voltage-sensor movement is both sufficient and rate limiting for fast inactivation in sodium channels. *J Gen Physiol*. 142:101–112.

Catterall, W.A. 2017. Forty years of sodium channels: structure, function, pharmacology, and epilepsy. *Neurochem Res*. 42(9):2495-2504.

Cha, A., Ruben, P.C., George, A.L.J., Fujimoto, E., and Bezanilla, F. 1999. Voltage sensors in domains III and IV, but not I and II, are immobilized by Na^+ channel fast inactivation. *Neuron.* 22:73-87. doi:10.1016/S0896-6273(00)80680-7. PMID:10027291

Chanda, B., and Bezanilla, F. 2002. Tracking voltage-dependent conformational changes in skeletal muscle sodium channel during activation. *J Gen Physiol.* 120:629–645. doi:10.1085/jgp.20028679

Chogot B., and Chazin W. J. 2011. Solution NMR structure of Apo-calmodulin in complex with the IQ motif of human cardiac sodium channel NaV1.5. *J Mol Biol.* 13:1881-1886.

De Lera Ruiz, M., and Kraus, R.L. 2015. Voltage-gated sodium channels: structure, function, pharmacology and clinical indications. *J Med Chem*. 58(18) :7093-7118.

Deschênes, I., Trottier, E., and Chahine, M. 2001. Implication of the C-terminal region of the α-subunit of voltage-gated sodium channels in fast inactivation. *J Membr Biol.* 183:103-114.

Gabelli S. B., Boto A., Kuhns V. H., Biancher M. A., Farinelli F., Aripirala S., Yoder J., Jakoncic J., Tomaselli G. F., and Amzel L. M. 2014. Regulation of the NaV1.5 cytoplasmic domain by calmodulin. *Nat Commun.* 5:5126.

Gabelli S. B., Yoder J. B., Tomaselli G. F., and Amzel M. 2016. Calmodulin and Ca2+ control of voltage gated Na+ channels. *Channels,* 10(1):45-54.

Goldfarb, M. 2005. Fibroblast growth factor homologous factors: evolution, structure, and function. *Cytokine Growth Factor Rev*. 16(2):215-220.

Goldin, A.L. 2001. Resurgence of sodium channel research. Annu Rev Phsyiol. 63:871-894.

Goldschen-Ohm, M.P., Capes, D.L., Oelstrom, K.M., and Chanda, B. 2013. Multiple pore conformations driven by asynchronous movements of voltage sensors in a eukaryotic sodium channel. *Nat Commun.* 4:1350. doi:10.1038/ncomms2356

Grandi, E., and Herren, A.W. 2014. CaMKII-dependent regulation of cardiac Na+ homeostasis. *Front Pharmacol*. 5:41.

Hennessey J. A., Marcou C. A., Wang C., Wei E. Q., Wang C., Tester D. J., … Pitt G. S. 2013. FGF12 is a candidate Brugada syndrome locus. *Heart Rhythm.* 10(12).

Hsu, E.J., Zhu, W., Schubert, A.R., Voelker, T., Varga, Z., and Silva, J.R. 2017. Regulation of Na^+ channel inactivation by the DIII and DIV voltage-sensing domains. *J Gen Physiol.* 14:389-403. doi:10.1085/jgp.201611678. PMID:28232510.

Johnson, C.N., Potet, F., Thompson, M.K., Kroncke, B.M., Glazer, A.M., Voehler, M.W., Knollmann, B.C., George, A.L., and Chazin, W.J. 2018. A mechanism, of calmodulin modulation of the human cardiac sodium channel. *Structure*. 26:683-694.

Kim J., Ghosh S., Liu H., Tateyama M., Kass R. S., and Pitt G. S. 2004. Calmodulin mediates Ca2+ sensitivity of sodium channels. *J Biol Chem.* 279(43):45004-45012.

Liu, C.J., Dib-Haji, S.D., Renganathan, M., Cummins, T.R., and Waxman, S.G. 2003. Modulation of the cardiac sodium channel NaV1.5 by fibroblast growth factor homologous factor 1B. *J Biol Chem*. 278(2):1029-1036.

Maltsev, V.A., and Undrovinas, A., 2008. Late sodium current in failing heart: friend or foe? *Prog Biophys Mol*. 96:421-451.

Mantegazza M., Yu F. H., Catterall W. A. and Scheuer T. 2001. Role of the C-terminal domain in inactivation of brain and cardiac sodium channels. *Proc Natl Acad Sci*, 98(26):15348-15353.

Morrow, D.A., Scirica, B.M., Karwatowska-Prokopczuk, E., Murphy, S.A., Budaj, A., Varshavsky, S., Wolff, A.A., Skene, A., McCabe, C.H., and Braunwald, E. 2007. Effects of Ranolazine on recurrent cardiovascular events in patients with non-ST-elevation acute coronary syndromes: The MERLIN-TIMI 36 randomized trial. *JAMA*. 297(16):1775-1783.

Motoike, H.K, Liu, H., Glaaser, I.W., Yang, A., Tateyama, M., and Kass, R.S. 2004. The Na channel inactivation gate is a molecular complex: a novel role of the COOH-terminal domain. *J Gen Physiol*. 123:155-165.

Musa H., Kline C. F., Sturm A. C., Murphy N., Adelman S., …., Mohler P. J. 2015. SCN5A variant that blocks fibroblast growth factor homologous factor regulation causes human arrhythmia. *Proc Natl Acad Sci.* 112(40):12528-12533.

Nerbonne, J.M., and Kass, R.S. 2005. Molecular physiology of cardiac repolarization. *Physiol Rev*. 85(4):1205-1253.

Pan, X., Li, Z., Zhou, Q., Shen, H., … and Yan, N. 2018. Structure of the human voltage-gated sodium channel $Na_v1.4$ in complex with β1. *Science*. 362(6412):eaau2486. doi: 10.1126/science.aau2486. PMID: 30190309.

Pitt, G.S., and Lee, S.Y. 2016. Current view on regulation of voltage-gated sodium channels by calcium and auxiliary proteins. *Protein Sci*. 25(9):1573-1584. doi:10.1002/pro.2960.

Sarhan M. F., Tung C. C., Petegem F. V., and Ahern C. A. 2012. Crystallographic basis for calcium regulation of sodium channels. *Proc Natl Acad Sci.* 109(9):3558-3563.

Smith, M.R., and Goldin, A.L. 1997. Interaction between the sodium channel inactivation linker and domain

III S4-S5. *Biophys J*. 73:1885-95. doi:10.1016/S0006-3495(97)78219-5. PMID:9336184

Ulbricht, W. 2005. Sodium channel Inactivation: Molecular Determinants and Modulation. *Phys Rev*. 85:1271-1301. doi.org/10.1152/physrev.00024.2004

Varga, Z., Zhu, W., Schubert, A.R., Pardieck, J.L., … and Silva J.R. 2015. Direct Measurement of Cardiac Na^+ Channel Conformations Reveals Molecular Pathologies of Inherited Mutations. *Circ Arrhythmia Electrophysiol*. 8:1228-39. doi:10.1161/CIRCEP.115.003155

Wang C., Chung B. C., Yan H., Lee S. Y., and Pitt G. S. 2012. Crystal structure of the ternary complex of a NaV C-terminal and calmodulin. *Structure.* 20:1167-1176.

Winters, J.J., and Isom, L.L. (2016). Developmental and regulatory functions of Na^+ channel non-pore-forming β subunits. Curr. Top. Membr. 78, 315-51. http://doi.org/10.1016/bs.ctm.2016.07.003.

Yu, F.H., and Catterall, W.A. 2003. Overview of the voltage-gated sodium channel family. *Genome Biol*. 4:207.

Zhu, W., Voelker, T.L., Varga, Z., Schubert, A.R., Nerbonne, J.M., and Silva, J.R. 2017. Mechanisms of noncovalent β subunit regulation of Na^+ channel gating. *J Gen Physiol*. 149(8):813-831. doi:10.1085/jgp.201711802

Zhu, W., Mazzanti, A., Voelker, T.L., Hou, P., … and Silva, J.R. 2019. Predicting Patient Response to the Antiarrhythmic Mexiletine Based on Genetic Variation. *Circ Res*. 124(4):539-552. doi:10.1161/CIRCRESAHA.118.314050. PMID: 30566038.

Zipes, D., Jalife, J., and Stevenson, W. 2017. *Cardiac Electrophysiology: From Cell to Bedside*. Elsevier, Inc.

Chapter 2: Mechanisms of intracellular fibroblast growth factor (iFGF) regulation of human cardiac sodium channel gating

2.1 Abstract

Voltage-gated sodium (Na_V) channels are responsible for the initiation and propagation of action potentials in neurons and myocytes. The Na_V channel α-subunit comprises 4 repeats (I-IV), that contain a voltage sensing domain (VSD) and a pore module. Na_V channel gating is regulated by myriad auxiliary subunits including intracellular fibroblast growth factors (iFGFs), designated FGF11-14. Their modulation of Na_V channel is iFGF gene specific. We investigated how FGF12B, which is highly expressed in human heart, regulates cardiac $Na_V1.5$ channel in the *Xenopus* oocyte heterologous expression system. We compared its regulation to FGF13VY, which is predominant in mouse heart, to examine iFGF differences in the regulatory mechanism. Both iFGFs induced depolarizing shifts in steady-state inactivation (SSI) and inhibited a slow component of inactivation. Relative to FGF12B, FGF13VY caused a larger voltage shift in SSI and a greater reduction in slower inactivation. Voltage-clamp fluorometry (VCF) revealed the iFGF modulation of VSD-IV activation, which has been previously linked to inactivation gating. FGF12B facilitated VSD-IV activation by causing a hyperpolarizing shift in half-maximal voltage ($V_{1/2}$), whereas FGF13VY accelerated its completion by increasing slope steepness. By observing $Na_V1.5$ regulation by iFGF chimeras of FGF12B and FGF13VY, we found a strong correlation between accelerated VSD-IV activation and the reduced slow inactivation component. Surprisingly, in native mouse myocytes, iFGF effects on shifting SSI matched oocyte data, but not the modulation of I_{Na} decay, suggesting that in native cells there are additional regulatory factors that may

act through VSD-IV to regulate Na_V channel inactivation gating.

2.2 Introduction

Voltage gated sodium (Na_V) channels are responsible for the excitation of cardiac myocytes. During the upstroke of an action potential (AP), the inward current conducted through cardiac $Na_V1.5$ depolarizes membrane potential and initiates an AP. Precise regulation of $Na_V1.5$ kinetics is essential for proper cardiac function, and disruption of Na_V channel inactivation predisposes the heart to arrhythmias (Noble and Noble, 2006) (Ton et al., 2021). Several mutations in the *SCN5A* gene that encodes $Na_V1.5$ are linked to congenital cardiac arrhythmias including long QT type 3 (LQT3) syndrome and Brugada syndrome (Ruan et al., 2009) (Zhu et al., 2019). The Na_V α-subunit is a pseudo-tetrameric protein, composed of 4 repeats. Each repeat contains 6 α-helical segments (S1-S6) that form voltage sensor domains (VSD) and a central pore module. The Na_V VSD, which contains S1-S4, can be activated upon membrane depolarization. Its activation is coupled to pore opening and inactivation kinetics (Varga et al., 2015). Evidence showed that the modulation of VSD activation by Na_V auxiliary subunits can affect Na_V channel gating (Zhu et al., 2017) (Angsutararux et al., 2021b).

The Na_V α-subunit associates with and is regulated by myriad auxiliary subunits (Abriel and Kass, 2005) (Meadows and Isom, 2005) (Abriel, 2010), including β-subunits (Calhoun and Isom, 2014), Calmodulin (CaM) (Gardill et al., 2019) and intracellular fibroblast growth factors (iFGFs) (Yang et al., 2016) (Pitt and Lee, 2016). iFGFs, also known as fibroblast growth factor homologous factors (FHFs) are a subfamily of the FGFs, and comprise FGF11-FGF14 (Olsen et al., 2003) (Goldfarb, 2005). iFGF regulation of Na_V channel function was previously demonstrated (Liu et al., 2001) (Liu et al., 2003) (Pablo and Pitt, 2016) (Goldfarb et al., 2007), and iFGF mutations are associated with inherited cardiac arrhythmias (Hennessey et al., 2013) (Li et al., 2017), and neurological disorders (Siekierska et al., 2016). Mutations in $Na_V1.5$ that disrupt iFGF

binding are also linked to cardiac disease (Musa et al., 2015). Each iFGF gene can generate 2 or more isoforms, distinct in their N-terminal sequences (Munoz-Sanjuan et al., 2000) (Pablo and Pitt, 2016). Past studies showed that modulation of Na_V channel function by iFGF was both gene and isoform specific (Munoz-Sanjuan et al., 2000) (Liu et al., 2003) (Goetz et al., 2009) (Wang et al., 2011b), and also depended on Na_V channel isoform. In the human heart, the dominant iFGF is FGF12B (Hennessey et al., 2013). To date, its regulatory mechanism of cardiac $Na_V1.5$ is unknown.

In this study, we investigated the molecular mechanism of FGF12B modulation of $Na_V1.5$ gating, with a focus on its effect on VSD activation. We compare its regulation to FGF13VY, which is highly expressed in mouse heart (Wang et al., 2011), to understand how different iFGF regulates Na_V channel function differently.

2.3 Results

2.3.1 FGF12B regulates $Na_V1.5$ kinetics via the modulation of VSD-IV activation

The *Xenopus* oocyte heterologous expression system allows us to study the effect of iFGF on $Na_V1.5$ kinetics with less complexity of other regulatory proteins including endogenous β-subunits. Ionic current recordings **(Fig 2.1A)** showed FGF12B modulation of Na_V channel gating. In comparison to $Na_V1.5$ alone, FGF12B co-expression shifted the voltage-dependence of activation (G-V) and steady-state inactivation (SSI) curves toward depolarizing potentials **(Table 2.1) (Fig 2.1B)**. Na_V channel recovery from inactivation was also faster in the presence of FGF12B, relative to $Na_V1.5$ alone ($Na_V1.5$: $T_{R,1}$ = 2.5 ± 0.2, $Na_V1.5$ + FGF12B: $T_{R,1}$ = 1.9 ± 0.3, p-value = 0.04) **(Table 2.2) (Fig 2.1C)**. Superimposed traces of I_{Na} **(Fig 2.1D, inset)** showed a faster decay in the presence of FGF12B. To quantify this observation, the normalized peak current decay was fitted to a bi-exponential function, which provides the better fit than a single exponential equation over all depolarizing potentials. The two inactivation time constants are in the timescale of a few and several milliseconds, corresponding to the fast and intermediate modes of inactivation after channel opening (Silva,

2014) (Silva and Goldstein, 2013a, b). We observed no difference in inactivation time constants **(Fig 2.1D)**, but in their amplitudes. The calculated fractional amplitude of slower inactivation component was significantly decreased with FGF12B co-expression **(Table 1) (Fig 2.1E)**. These findings imply FGF12B impaired a slower component of open-state inactivation.

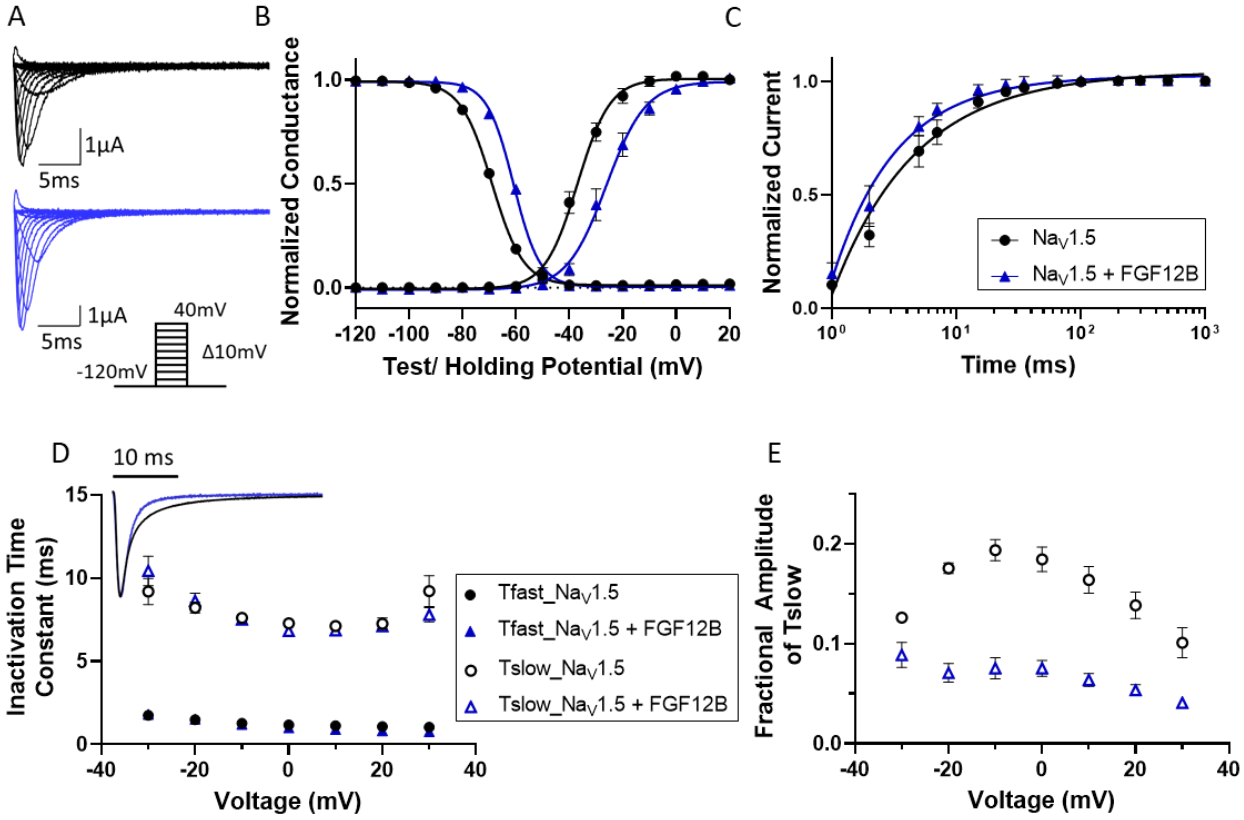

Figure 2.1: FGF12B modulation of hNa$_V$1.5 kinetics
(A) Exemplary I_{Na} traces of hNa$_V$1.5 alone (black) and with FGF12B co-expression (blue) during activation protocols from a holding potential of -120 mV, stepping up to 40 mV in an increment of 10 mV. **(B)** Voltage dependence of activation (G-V) and steady-state inactivation (SSI) curves were shifted towards depolarizing potentials by the co-expression of FGF12B, relative to hNa$_V$1.5 alone. **(C)** Recovery from inactivation curves showed an accelerated recovery from FGF12B co-expression. **(D)** An overlay of exemplary traces at -20 mV between hNa$_V$1.5 with and without FGF12B emphasizes the difference observed during peak current decay (inset). A fitting of peak current decay to a bi-exponential function yields two inactivation time constants (fast and slow) at various depolarizing potentials. **(E)** The fractional amplitude of slower inactivation time constant was calculated and compared between hNa$_V$1.5 alone and with FGF12B co-expression. FGF12B caused a reduction in the fractional amplitude of slower inactivation.

Next, we employed the voltage-clamp fluorometry (VCF) protocol (Mannuzzu et al., 1996) (Stefani and Bezanilla, 1998) (Gandhi and Olcese. 2008) (Rudokas et al., 2014) to investigate the mechanism of FGF12B modulation. A cysteine mutation was introduced into the extracellular linker S3-S4 in each VSD for

fluorophore (MTS-TAMRA) tagging. The movement of S4 upon membrane depolarization can be observed by the change in fluorescence emission reflecting an altered surrounding environment (Varga et a., 2015) (Zhu et al., 2016). To improve the sensitivity of the technique, the cysteine mutation was created in the background of WT-LFS (Large Fluorescence Signal), bearing Y1977A-C373Y mutations that ablate a ubiquitination site and prevent non-specific labeling (Varga et a., 2015). Our previous work showed that the LFS mutation does not substantially affect Na_V channel activation and inactivation kinetics. Specific sites of cysteine mutations for individual VSDs were based on our past studies (Varga et a., 2015) (Zhu et al., 2017). Voltage-dependent changes in the fluorescence signal (F-V) curve for each VSD can be used to estimate the conformational change during VSD activation.

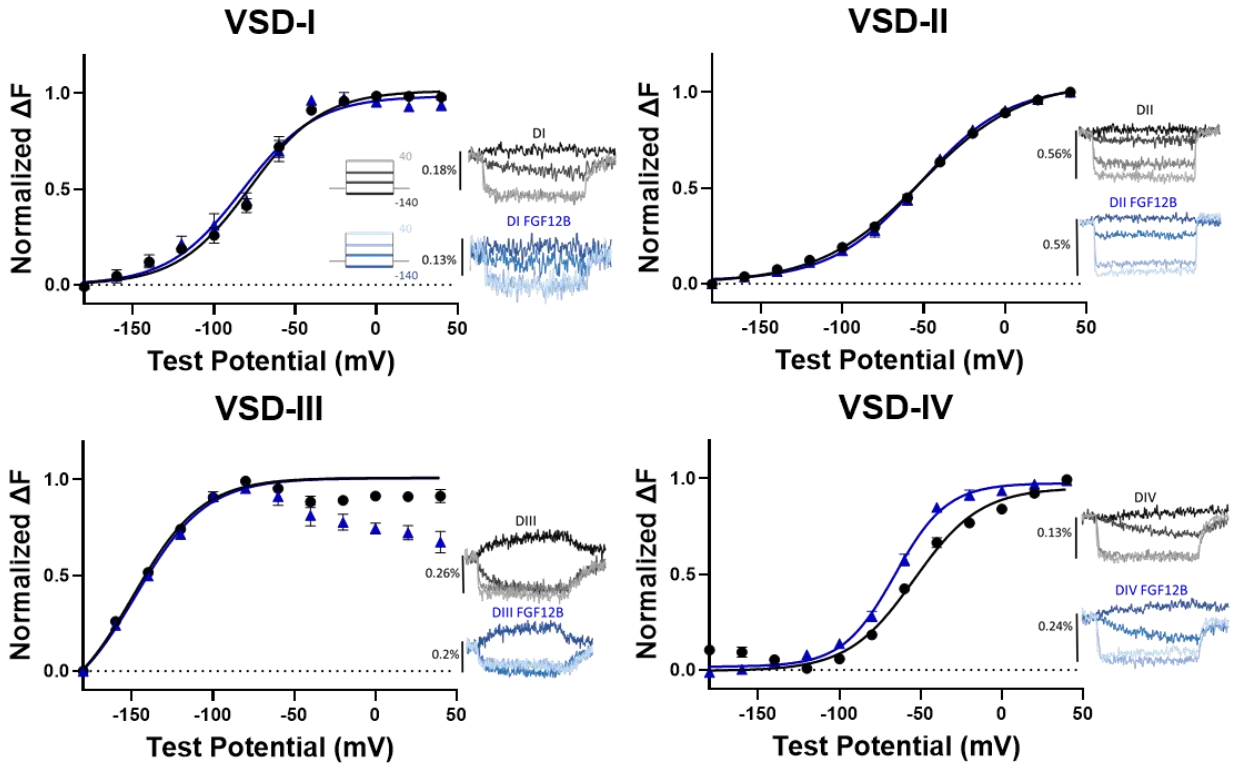

Figure 2.2: FGF12B regulation of individual VSD activation
Voltage-clamp fluorometry (VCF) protocol was used to measure the effect of FGF12B co-expression on the activation of individual VSD. The voltage-dependence of normalized fluorescence emission (F-V) graphs of VSD-I to VSD-IV were shown for $hNa_V1.5$ alone (black) or with FGF12B co-expression (blue). Exemplary fluorescence traces, corresponding to different depolarizing potentials, were included for each VSD recording. FGF12B shifts the activation of VSD-IV towards hyperpolarizing potentials.

The experimental results show that co-expression of FGF12B caused no change in the half-maximal voltages ($V_{1/2}$) of VSD-I, VSD-II and VSD-III F-V curves **(Fig 2.2)**. For VSD-III, however, we observed a change at potentials greater than -50 mV. Multiple lines of evidence suggest that VSD-III can activate in two discrete steps (Chanda and Bezanilla, 2002) (Hsu et al., 2017) (Zhu et al., 2017). Co-expression of FGF12B did not affect the initial activation at very hyperpolarized potentials. However, the second translation of VSD-III, observed as an opposite deflection, during depolarized potentials was affected by FGF12B **(Fig 2.2)**. This second VSD-III activation was proposed to regulate open-state inactivation (Angsutararux et al., 2021a).

FGF12B induced a significant change VSD-IV F-V, causing a hyperpolarizing shift in $V_{1/2}$ and a decrease in a slope factor (k) **(Table 2.2) (Fig 2.2)**. The voltage shift implies that the activation of VSD-IV is facilitated, whereas the steeper slope reflects an accelerated translation of VSD-IV to complete its activation at less depolarized potentials. Together these results suggest that FGF12B facilitation of VSD-IV activation underlies the change in $Na_V1.5$ inactivation.

2.3.2 FGF13VY shows differential modulation of $Na_V1.5$ kinetics and a distinct effect on VSD regulation

Next, we investigated the FGF13VY effect on $Na_V1.5$. An analysis of recorded ionic current **(Fig 2.3A)** comparing $Na_V1.5$ alone and $Na_V1.5$ co-expressed with FGF13VY revealed the shifts in SSI curve toward depolarizing potentials, with no effect on G-V **(Table 2.1) (Fig 2.3B)**. The change in SSI $V_{1/2}$ by FGF13VY, was larger in magnitude than an alteration by FGF12B ($Na_V1.5$ + FGF12B: SSI $\Delta V_{1/2}$ = 8.1 mV, $Na_V1.5$ + FGF13VY: SSI $V_{1/2}$ = 14.5 mV). The channel recovery from inactivation was also facilitated by FGF13VY ($Na_V1.5$: $T_{R,1}$ = 2.5 ± 0.2, $Na_V1.5$ + FGF13VY: $T_{R,1}$ = 1.3 ± 0.1, p-value < 0.001) **(Table 2.1) (Fig 2.3C)**. The altered current decay by FGF13VY **(Fig 2.3D, inset)** was due to a reduction in the slower component of inactivation, as shown by reduced fractional amplitude **(Fig 2.3E)**. Both fast and slower inactivation time constants remained unaffected **(Table 2.1) (Fig 2.3D)**. A comparison also showed a larger reduction of slower

inactivation component by FGF13VY than FGF12B, especially at more depolarized potentials.

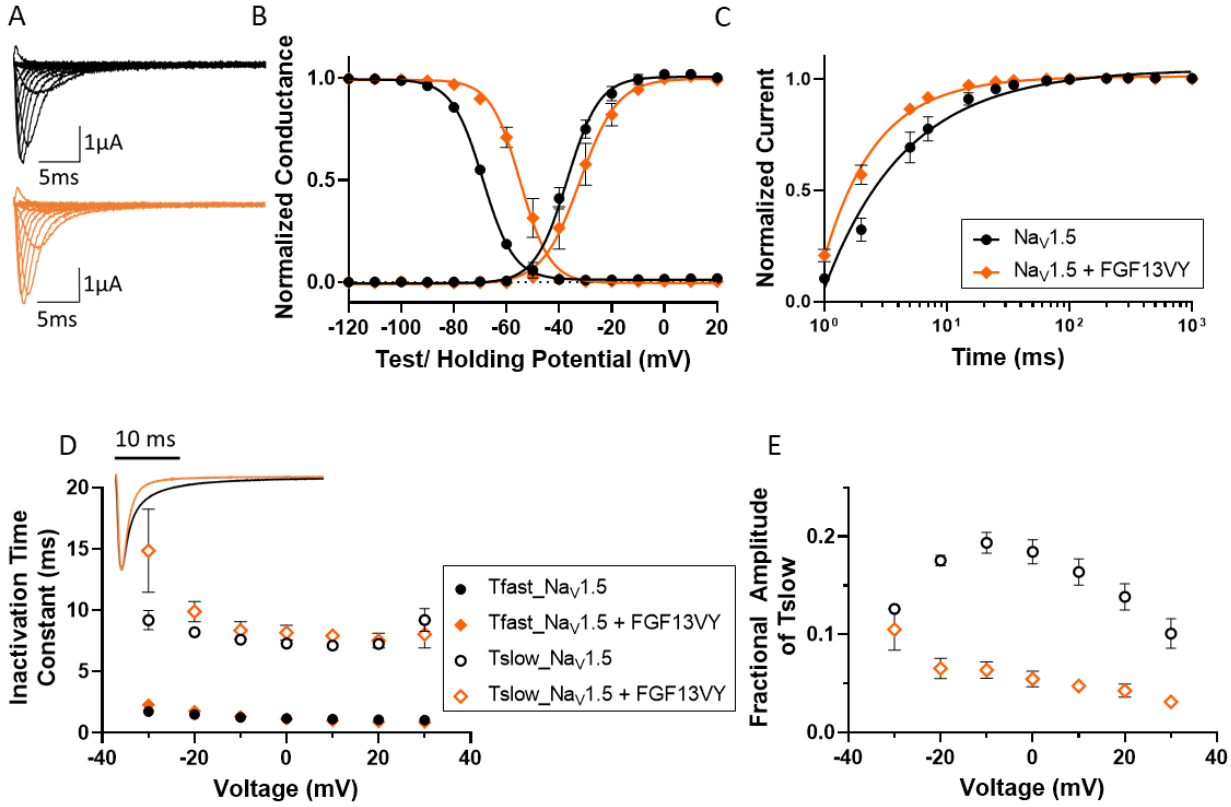

Figure 2.3: FGF13VY modulation of hNa$_V$1.5 kinetics
(A) Exemplary I_{Na} traces of hNa$_V$1.5 alone (black) and with FGF13VY co-expression (orange) during activation protocols. **(B)** The G-V and SSI curves revealed the depolarizing shifts in SSI by FGF13VY, relative to hNa$_V$1.5 alone. **(C)** Recovery from inactivation was accelerated by FGF13VY co-expression when compared to hNa$_V$1.5 alone. **(D)** An overlay of exemplary traces at -20 mV emphasizes the difference observed during peak current decay between hNa$_V$1.5 alone and with FGF13VY (inset). Two inactivation time constants (fast and slow) from the peak current decay fit were compared in hNa$_V$1.5 with and without FGF13VY. **(E)** The fractional amplitude of slower inactivation time constant was calculated. The plot showed the reduction in the fraction of slower inactivation time constants by FGF13VY, relative to hNa$_V$1.5 alone.

Investigation of individual VSD activation revealed the impact of FGF13VY on the VSD-I and VSD-IV F-V curves **(Table 2.2) (Fig 2.4)**. The VSD-I F-V curve was shifted towards positive potentials by FGF13VY co-expression, whereas the VSD-IV F-V curve showed an opposite shift in $V_{1/2}$ with additional increase in its slope steepness. The modulation of VSD-I is specific to FGF13VY, and hence is not likely the common mechanisms shared between iFGFs. Instead, we suspected this might be the result of longer FGF13VY N-terminus that can potentially affect activation gate. We will elaborate on this observation later in the discussion.

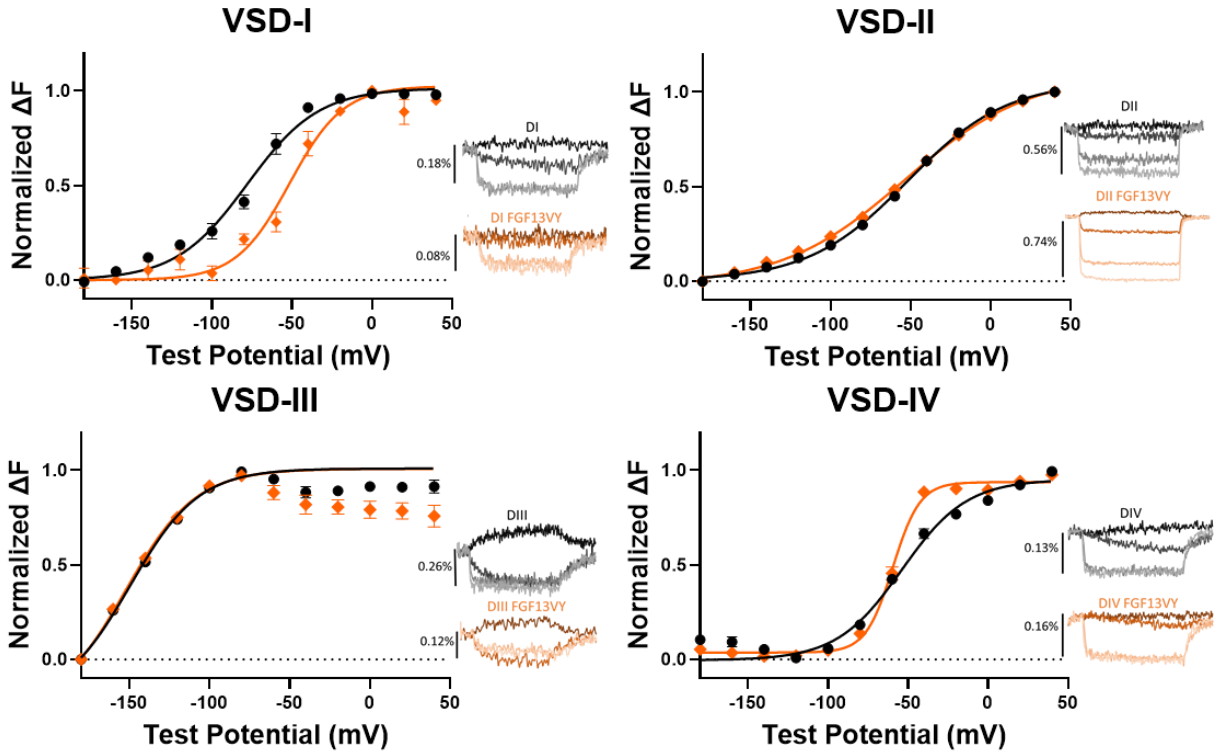

Figure 2.4: FGF13VY regulation of individual VSD activation
The VCF protocol was used to measure the effect of FGF13VY co-expression on the activation of individual VSD. The F-V graphs of VSD-I to VSD-IV were shown for $hNa_V1.5$ alone (black) or with FGF13VY co-expression (orange). Exemplary fluorescence traces were included for each VSD recording.

A comparison between VSD-IV F-V curves of FGF12B and FGF13VY revealed a clear distinction on their modulation. FGF13VY prominently reduced the slope factor (FGF12B: k = 16.5 ± 1.2, FGF13VY: k = 9.4 ± 1.0, p-value = 0.004), whereas FGF12B shifted $V_{1/2}$ to more negative potentials (FGF12B: $V_{1/2}$ = -66.2 ± 2.3 mV, FGF13VY: $V_{1/2}$ = -60.4 ± 1.3 mV, p-value = 0.04). The unique regulation of VSD-IV activation by different iFGFs suggests its significance in the differential effects of $Na_V1.5$ kinetics, which we will explore more in the following section.

Table 2.1: Fit parameters of $Na_V1.5$ compared to $Na_V1.5$ with FGF12B and FGF13VY co-expressions

Parameter		**$Na_V1.5$**	**$Na_V1.5$ + FGF12B**	**$Na_V1.5$ + FGF13VY**
GV				
	$V_{1/2}$ (n)	-37.0 ± 0.6 (5)	-26.2 ± 2.2 (6)	-32.3 ± 3.1 (6)
	p-value		0.012 (*)	0.30
	k	6.1 ± 0.3	6.6 ± 0.4	5.5 ± 0.5
	p-value		0.56	0.56
SSI				
	$V_{1/2}$ (n)	-69.0 ± 0.5 (9)	-60.9 ± 0.4 (7)	-54.5 ± 1.8 (6)
	p-value		<0.001 (***)	<0.001 (***)
	k	5.8 ± 0.3	4.9 ± 0.3	4.7 ± 0.4
	p-value		0.081	0.035 (*)
Recovery	**$T_{R,1}$ (n)**	2.5 ± 0.2 (8)	1.9 ± 0.3 (5)	1.3 ± 0.1 (5)
	p-value		0.04 (*)	<0.001 (***)
	$T_{R,2}$	15.8 ± 1.4	12.5 ± 1.3	8.5 ± 1.3
Peak decay				
At -30 mV	**T_{fast} (n)**	1.7 ± 0.2 (5)	1.8 ± 0.2 (6)	2.3 ± 0.3 (5)
	T_{slow}	9.2 ± 0.8	10.4 ± 0.9	14.9 ± 3.4
	A_{slow}	0.13 ± 0.004	0.09 ± 0.01	0.11 ± 0.02
At -20 mV	**T_{fast}**	1.5 ± 0.2	1.5 ± 0.1	1.8 ± 0.1
	T_{slow}	8.2 ± 0.3	8.6 ± 0.5	9.9 ± 0.8
	A_{slow}	0.18 ± 0.01	0.07 ± 0.01	0.07 ± 0.01
At -10 mV	**T_{fast}**	1.3 ± 0.1	1.2 ± 0.04	1.3 ± 0.1
	T_{slow}	7.6 ± 0.2	7.5 ± 0.2	8.4 ± 0.7
	A_{slow}	0.19 ± 0.01	0.08 ± 0.01	0.06 ± 0.01
At 0 mV	**T_{fast}**	1.2 ± 0.1	1.0 ± 0.005	1.1 ± 0.1
	T_{slow}	7.3 ± 0.3	6.8 ± 0.1	8.2 ± 0.6
	A_{slow}	0.18 ± 0.01	0.08 ± 0.008	0.05 ± 0.008
At 10 mV	**T_{fast}**	1.1 ± 0.1	0.9 ± 0.01	1.0 ± 0.05
	T_{slow}	7.1 ± 0.3	6.9 ± 0.1	7.9 ± 0.5
	A_{slow}	0.16 ± 0.01	0.06 ± 0.007	0.05 ± 0.008
At 20 mV	**T_{fast}**	1.1 ± 0.1	0.8 ± 0.02	0.9 ± 0.05
	T_{slow}	7.3 ± 0.3	7.1 ± 0.2	7.5 ± 0.6
	A_{slow}	0.14 ± 0.01	0.05 ± 0.006	0.04 ± 0.007
At 30 mV	**T_{fast}**	1.0 ± 0.1	0.8 ± 0.01	0.9 ± 0.05
	T_{slow}	9.2 ± 1.0	7.8 ± 0.4	8.0 ± 1.1
	A_{slow}	0.1 ± 0.02	0.04 ± 0.005	0.03 ± 0.005

Table 2.2: Fit parameters of voltage dependence of fluorescence (F-V) curves for all voltage sensor domains of $Na_V1.5$ alone, and with FGF12B and FGF13VY co-expression

Parameter		**$Na_V1.5$**	**$Na_V1.5$ + FGF12B**	**$Na_V1.5$ + FGF13VY**
VSD-I FV				
	$V_{1/2}$ (n)	-75.2 ± 3.6 (4)	-77.6 ± 4.6 (3)	-50.1 ± 3.1 (4)
	p-value		0.70	0.002 (**)
	k	19.4 ± 0.9	21.2 ± 2.7	13.7 ± 1.2
	p-value		0.49	0.009 (**)
VSD-II FV				
	$V_{1/2}$ (n)	-51.6 ± 1.8 (5)	-53.1 ± 2.9 (4)	-53.4 ± 1.7 (5)
	p-value		0.68	0.50
	k	33.0 ± 4.9	27.4 ± 2.0	38.7 ± 0.9
	p-value		0.36	0.24
VSD-III FV				
	$V_{1/2}$ (n)	-149.7 ± 1.6 (10)	-145.6 ± 2.1 (8)	-153.4 ± 4.3 (6)
	p-value		0.4	0.5
	k	21.4 ± 0.8	20.6 ± 0.7	22.0 ± 2.0
	p-value		0.84	0.90
VSD-IV FV				
	$V_{1/2}$ (n)	-52.9 ± 2.0 (8)	-66.2 ± 2.3 (8)	-60.4 ± 1.3 (8)
	p-value		<0.001 (***)	0.022 (*)
	k	20.5 ± 1.3	16.5 ± 1.2	9.4 ± 1.0
	p-value		0.044 (*)	<0.001 (***)

2.3.3 iFGF specific modulation of VSD-IV activation determines the slower component of $Na_V1.5$ inactivation

iFGFs consist of three main domains: the N-terminus, the β-trefoil core and the C-terminus. High similarities are shared among iFGFs in the core domain (Olsen et al., 2003), which serves as the interaction site with the Na_V C-terminal domain (CTD) (Goetz et al., 2009) (Wang et a., 2012) (Musa et al., 2015) (Hennessey et al., 2013). If all iFGFs are thought to bind to the same CTD location, it is unknown how iFGFs regulate Na_V channels differently. Previously, a role for the N-terminus on the FGF13 isoform-specific modulation of $Na_V1.5$ gating was suggested (Lou et al., 2005) (Laezza et al., 2009) (Yang et al., 2016) (Barbosa et al., 2017). An alignment of FGF12B and FGF13VY sequences showed the largest differences lie in N-terminus **(Fig S2.1A)**. We hence constructed the iFGF chimeras with swapped N-terminal sequences to test their specificity on VSD-IV regulation.

We switched the N-terminus of FGF13VY (aa1-72) and FGF12B (aa1-4) in FGF12B/13 (12NTD-13Core-13CTD) and FGF13VY/12 (13NTD-12Core-12CTD) chimeras **(Fig S2.1B)**. If the N-terminal domain alone is sufficient for distinct iFGF effect, we expect the shifts in VSD-IV F-V, G-V and SSI curves by FGF12B/13 and FGF13VY/12 chimeras to resemble FGF12B and FGF13VY accordingly. Instead, these iFGF chimeras showed distinct modulation of VSD-IV activation, as well as in G-V and SSI **(Table 2.3, 2.4) (Fig S2.1C)**. Further chimera experiments were conducted in a similar manner. We created 2 additional pairs of chimeras switching (1) the C-terminus and (2) both N- and C-termini, between FGF12B and FGF13VY. None of the chimera pairs replicated the regulation of the VSD-IV F-V curve by FGF12B and FGF13VY **(Table 2.3, 2.4) (Fig S2.2)**. The results suggest that all iFGF domains synergistically contribute to VSD-IV activation.
We used data obtained from these iFGF chimeras to further identify the contribution of unique VSD-IV regulation to $Na_V1.5$ gating. We measured the $V_{1/2}$ and k of G-V and SSI, and the fitted inactivation time constants and the amplitudes from the peak current decay **(Table 2.3)**. The activation of VSD-IV has been previously shown to facilitate Na_V channel fast inactivation (Chahine et al., 1994) (Horn et al., 2000) (Chanda

and Bezanilla, 2002) (Hsu et al., 2017), and the charge neutralization mutations on IV S4 significantly shift the SSI $V_{1/2}$ (Capes et al., 2013). Surprisingly, we found no such correlation between VSD-IV F-V and SSI on either $V_{1/2}$ or k ($V_{1/2}$: $R^2 = 0.055$, k: $R^2 = 0.39$) **(Fig 2.5A, B)**. Similarly, no relationship could be established between VSD-IV F-V and G-V either ($V_{1/2}$: $R^2 = 2.7x10^5$, k: $R^2 = 0.12$) **(Fig S2.3A, B)**. Instead, the slope factor (k) of VSD-IV F-V curve yielded a good correlation to the slower inactivation time constant and the fractional amplitude of slower inactivation time constants (T_{slow}: R^2 at 0, 10, 20 mV = 0.63, 0.62 and 0.46, fractional amplitude of T_{slow}: R^2 at 0, 10, 20 mV = 0.58, 0.56 and 0.62) **(Fig 2.5C, D)**. The correlation was not established for the $V_{1/2}$ of VSD-IV F-V curve (T_{slow}: R^2 at 0, 10, 20 mV = 0.29, 0.29 and 0.26, fractional amplitude of T_{slow}: R^2 at 0, 10, 20 mV = 0.004, 0.009 and 0.05) **(Fig S2.3C, D)**.

Together, the results suggest that the slope of VSD-IV F-V is a strong determinant of the slower component of Na_V inactivation. The two parameters from VSD-IV F-V ($V_{1/2}$ and k) can be used to predict the fractional amplitude of slower inactivation time constants, with more accuracy than the prediction of SSI $V_{1/2}$ (R^2 values between actual results and predicted values: $T_{slow} = 0.72$, SSI $V_{1/2} = 0.58$) **(Fig 2.5E, F)**. We showed a steeper VSD-IV F-V, corresponding to the earlier completion of VSD-IV activation at less depolarized potentials, contributes to an inhibited slower inactivation component. The lower predictability of SSI $V_{1/2}$ by VSD-IV F-V parameters implies an additional element is needed for iFGF modulation of SSI.

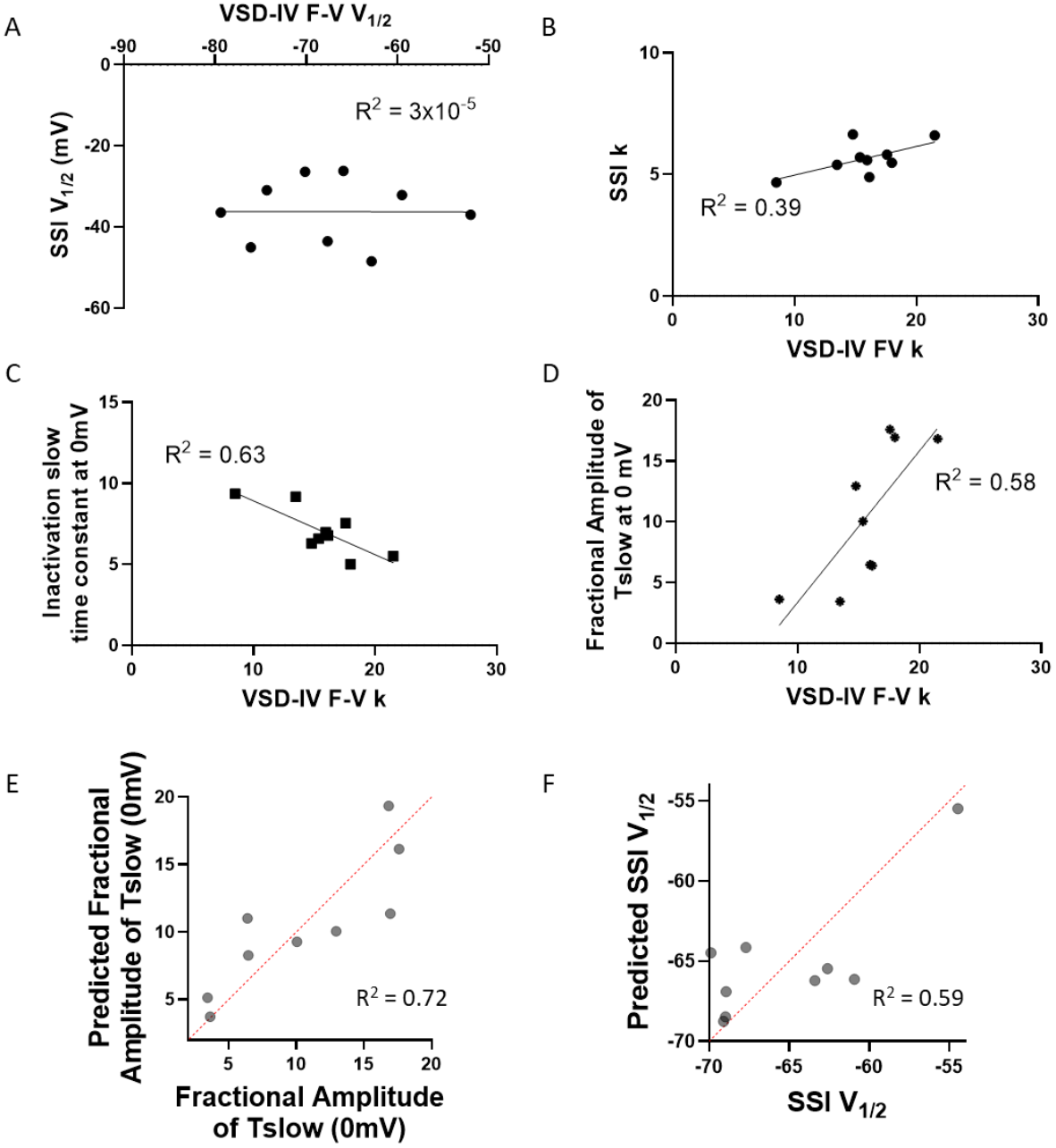

Figure 2.5: Regression analyses reveal a correlation between VSD-IV activation curve and Nav channel inactivation kinetics

Linear regression analysis was performed on the results of FGF12B, FGF13VY and iFGF chimeras co-expression. There is no relationship between VSD-IV F-V curve and SSI, in terms of either half-maximal voltage ($V_{1/2}$) **(A)** or slope factor (k) **(B)**. A relationship was found between the slope factor (k) of VSD-IV F-V curves and the slower inactivation time constant, shown as the representative at 0 mV depolarization **(C)**. Similar relationship was identified between the k of VSD-IV F-V curve and the fractional amplitude of slower inactivation time constant **(D)**. Both k and $V_{1/2}$ of VSD-IV F-V curves were used to predict the fractional amplitude of slower inactivation time constant better than SSI $V_{1/2}$, as shown by the plots between predicted and actual values in **(E)** and **(F)** accordingly.

Table 2.3: Fit parameters of $Na_V1.5$ co-expressed with iFGF chimeras

Parameter		**12NTD-13Core-13CTD**	**13NTD-12Core-12CTD**	**13NTD-13Core-12CTD**	**12NTD-12Core-13CTD**	**12NTD-13Core-12CTD**	**13NTD-12Core-13CTD**
GV							
	$V_{1/2}$	-48.5 ± 0.6	-45.6 ± 2.7	-43.6 ± 1.7	-36.32 ± 1.2	-45.1 ± 1.3	-26.4 ± 1.6
	k (n)	5.3 ± 0.4 (4)	7.4 ± 0.1 (5)	6.5 ± 0.4 (7)	6.7 ± 0.6 (5)	5.7 ± 0.4 (5)	6.5 ± 0.4 (7)
SSI							
	$V_{1/2}$	-69.9 ± 0.4	-63.4 ± 0.7	-60.7 ± 0.5	-69.0 ± 0.6	-69.1 ± 0.8	-67.7 ± 0.6
	k (n)	6.6 ± 0.3 (4)	5.4 ± 0.1 (13)	5.6 ± 0.1 (9)	5.4 ± 0.1 (7)	6.5 ± 0.1 (5)	5.3 ± 0.1 (6)
VSD-IV FV							
	$V_{1/2}$	-62.5 ± 2.2	-74.5 ± 2.2	-67.7 ± 1.7	-79.6 ± 2.1	-76.5 ± 2.9	-70.1 ± 0.9
	k (n)	14.5 ± 1.1 (9)	15.6 ± 1.0 (9)	15.2 ± 0.7 (5)	17.9 ± 0.7 (8)	20.9 ± 1.3 (6)	13.7 ± 0.7 (8)
Peak decay							
At -20 mV	**T_{fast} (n)**	1.21 ± 0.06 (6)	1.31 ± 0.05 (12)	1.41 ± 0.08 (8)	1.14 ± 0.04 (8)	1.12 ± 0.03 (4)	1.62 ± 0.15 (5)
	T_{slow}	6.48 ± 0.26	6.86 ± 0.51	7.55 ± 0.47	5.49 ± 0.14	6.37 ± 0.19	11.29 ± 1.70
	A_{slow}	14.8 ± 1.0	8.4 ± 1.0	12.0 ± 1.5	16.4 ± 0.6	16.7 ± 2.1	4.8 ± 0.6
At -10 mV	**T_{fast}**	1.08 ± 0.03	1.11 ± 0.03	1.21 ± 0.05	0.99 ± 0.02	0.98 ± 0.03	1.34 ± 0.09
	T_{slow}	6.35 ± 0.17	6.95 ± 0.48	7.23 ± 0.39	5.28 ± 0.14	5.92 ± 0.33	10. 67 ± 1.34
	A_{slow}	14.0 ± 1.0	7.3 ± 0.6	10.8 ± 1.3	17.5 ± 0.4	17.5 ± 1.7	3.6 ± 0.5
At 0 mV	**T_{fast}**	0.99 ± 0.02	1.00 ± 0.02	1.07 ± 0.05	0.91 ± 0.01	0.89 ± 0.02	1.09 ± 0.07
	T_{slow}	6.29 ± 0.03	6.98 ± 0.32	6.58 ± 0.41	5.01 ± 0.18	5.51 ± 0.39	9.17 ± 0.72
	A_{slow}	12.9 ± 1.2	6.5 ± 0.5	10.0 ± 1.0	16.9 ± 0.6	16.8 ± 1.7	3.4 ± 0.4
At 10 mV	**T_{fast}**	0.90 ± 0.02	0.92 ± 0.02	0.99 ± 0.04	0.85 ± 0.02	0.84 ± 0.03	0.94 ± 0.06
	T_{slow}	5.97 ± 0.06	6.93 ± 0.29	6.24 ± 0.34	4.68 ± 0.23	5.13 ± 0.45	8.84 ± 0.75
	A_{slow}	12.0 ± 1.1	5.7 ± 0.4	8.4 ± 0.8	16.0 ± 0.8	15.8 ± 1.7	3.2 ± 0.4
At 20 mV	**T_{fast}**	0.86 ± 0.02	0.86 ± 0.02	0.91 ± 0.04	0.79 ± 0.02	0.77 ± 0.03	0.87 ± 0.06
	T_{slow}	6.41 ± 0.33	6.99 ± 0.36	5.70 ± 0.41	4.36 ± 0.28	4.75 ± 0.51	9.39 ± 1.32
	A_{slow}	11.3 ± 1.0	5.1 ± 0.4	7.8 ± 0.9	14.7 ± 0.9	14.8 ± 1.7	2.8 ± 0.4

Table 2.4: Fit parameters of VSD-IV F-V curves for iFGF chimeras relative to FGF12B and FGF13VY were tested for the significance of N-terminus (FGF12B/13 and FGF13VY/12), C-terminus (FGF13VY/12CTD and FGF12B/13CTD) and both N- and C-terminal domains (FGF12B-13Core and FGF13VY-12Core) via ANOVA analysis.

	12NTD-13Core-13CTD	**13NTD-13Core-12CTD**	**12NTD-13Core-12CTD**
$\Delta V_{1/2}$ relative to FGF12B	-3.7 mV	1.4 mV	10.3 mV
p-value	0.48	0.96	0.01 (*)
Δk relative to FGF12B	2.0	1.3	-4.4
p-value	0.42	0.83	0.04 (*)
	13NTD-12Core-12CTD	**12NTD-12Core-12CTD**	**13NTD-12Core-13CTD**
$\Delta V_{1/2}$ relative to FGF13VY	14.1 mV	19.1 mv	-9.6 mV
p-value	< 0.001 (***)	< 0.001 (***)	0.002 (**)
Δk relative to FGF13VY	-6.1	-8.4	-4.3 mV
p-value	< 0.001 (***)	< 0.001 (***)	0.005 (**)

2.3.4 iFGF potentially modulates the inactivation gate kinetics, important for the regulation of $Na_V1.5$ SSI

The Na_V channel inactivation gate requires an IFMT motif on the III-IV linker that causes an allosteric block of the channel pore (West et al., 1992) (Pan et al., 2018) (Jiang et al., 2020) (Angsutararux et al., 2021a). A recent structure of eukaryotic Na_VPaS channel hints at possible direct interaction between Na_V CTD and III-IV linker (Shen et al., 2017), which was speculated to regulate Na_V inactivation (Gade et al., 2020) (Peters et al., 2020). iFGF binding was found near this interaction site (Wang et al., 2012) and may affect it.

We conducted a mutagenesis study to (1) remove an inactivation gate (IFM/IQM mutation) (Hartmann et al., 1994), and (2) sever the interaction between III-IV linker and Na_V CTD (E1784K mutation) (Shen et al., 2017) (Gardill et al., 2018) (Gade et al., 2020). We found that both mutations negate the iFGF-mediated alterations in SSI and GV, but not the VSD-IV F-V **(Table 2.5) (Fig 2.6)**. The mutations altered VSD-IV F-V curves, but specific modulatory effects of FGF12B and FGF13VY paralleled the results in WT VSD-IV. FGF12B still induced pronounced hyperpolarizing shift in $V_{1/2}$, while FGF13VY distinctly altered the slope factor. Together, this mutagenesis experiment indicated that the inactivation gate is not responsible for the regulation of VSD-IV, but instead, is essential for the iFGF-mediated shifts in SSI.

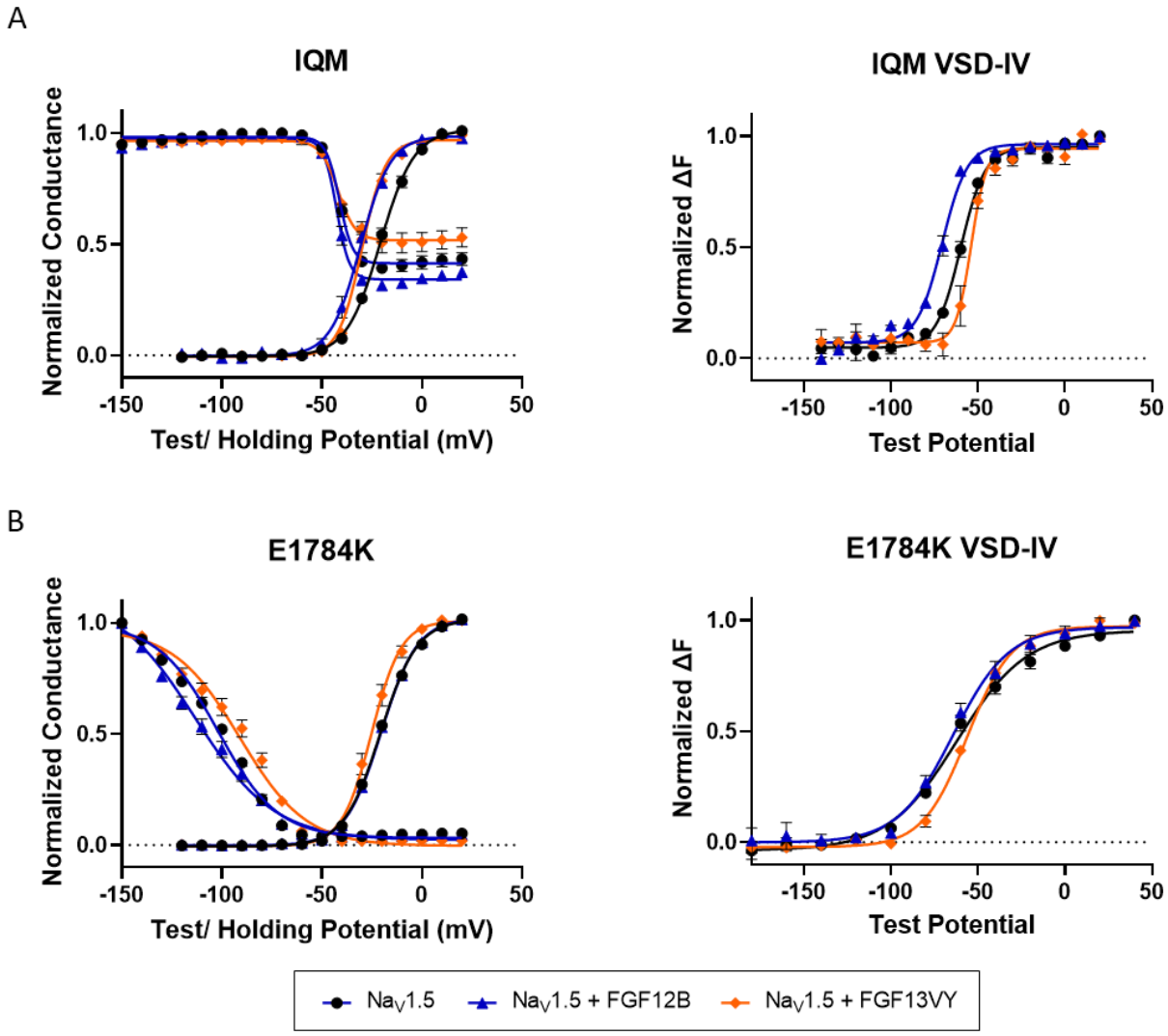

Figure 2.6: The Na_V channel inactivation gate is necessary for iFGF modulation of SSI, but not VSD-IV activation

(A) The IFM/IQM mutation was introduced to impair the Na_V channel fast inactivation gate (IFMT motif) and to investigate its significance on iFGF modulation. The co-expressions of FGF12B and FGF13VY no longer cause the shifts in SSI in IQM channel (left). Both FGF12B and FGF13VY induce the similar shifts in the G-V curves (left). However, the VSD-IV F-V curves (right) show similar alterations by iFGFs as in WT VSD-IV. **(B)** The E1784K mutation interferes with the interaction between Na_V CTD and III-IV linker. This mutation negates the shifts in SSI and G-V by FGF12B and FGF13VY (left) but does not alter the VSD-IV activation curves (right).

2.3.5 iFGF effects in mouse ventricular myocytes

As reported in other studies (Wang et al., 2011a) (Park et al., 2016), we found that FGF13VY is the predominant isoform expressed in mouse ventricles. We generated the mouse model of global FGF13 knockout (FGF13KO) and tested the Na_V channel gating in isolated ventricular myocytes. In comparison to WT and Floxed mice, the deletion of FGF13 did not affect the peak I_{Na} density **(Fig 2.7A, Fig S2.4A)**, nor the voltage-dependence of Na_V channel activation **(Table 2.6) (Fig 2.7B)**. Floxed mice were used as negative control, to ensure the Cre-lox system does not affect I_{Na} **(Fig 2.7B)**. In FGF13KO myocytes, we observed a shift in SSI toward hyperpolarizing potentials **(Table 2.6) (Fig 2.7B)**, consistent with the results from *Xenopus* oocytes. The recovery from inactivation was not altered by the FGF13 knockout (WT: $T_{R,1}$ = 8.1 ± 1.4, FGF13KO: $T_{R,1}$ = 6.3 ± 0.9, p-value = 0.26) **(Table 2.6) (Fig 2.7C)**.

The alteration in the peak current decay can be noticed in FGF13KO. The decay fitted to a double exponential function showed unaffected inactivation time constants but reduced fractional amplitude of slower inactivation component in FGF13KO myocytes **(Table 2.6) (Fig 2.7D, E)**. This change is in the opposite direction from the results obtained in *Xenopus* oocytes. In mouse myocytes, the I_{Na} decays faster when FGF13 was absent, due to the reduction in slower component of inactivation **(Fig 2.7E)**. Similar knockout of FGF12B in mice (FGF12B KO) did not alter any kinetics of the I_{Na} in ventricular cardiomyocytes **(Table 2.6) (Supplementary Fig 2.4B)**. This result is expected, given that FGF12B is not expressed in the mouse ventricle.

We then introduced FGF12B in the FGF13KO mice and found that the SSI was shifted back towards depolarizing potentials, but not as positive as in WT mice **(Table 2.6) (Fig 2.8A, B)**. We also observed the shift in G-V curve by FGF12B plasmid in FGF13KO mice towards depolarizing potentials **(Fig 2.8B)**. A reduction in peak current density was not significant **(Fig S2.4A)**. The presence of FGF12B enhanced the recovery from inactivation (FGF13KO: $T_{R,1}$ = 6.3 ± 0.9, FGF13KO + FGF12BT: $T_{R,1}$ = 4.0 ± 0.6, p-value = 0.04) **(Table 2.6) (Fig 2.8C)** but did not alter the inactivation kinetics. The fast and slower inactivation time

constants, as well as the fractional amplitude of slower inactivation were not affected by FGF12B expression in FGF13KO myocytes **(Table 2.6) (Fig 2.8D, E)**.

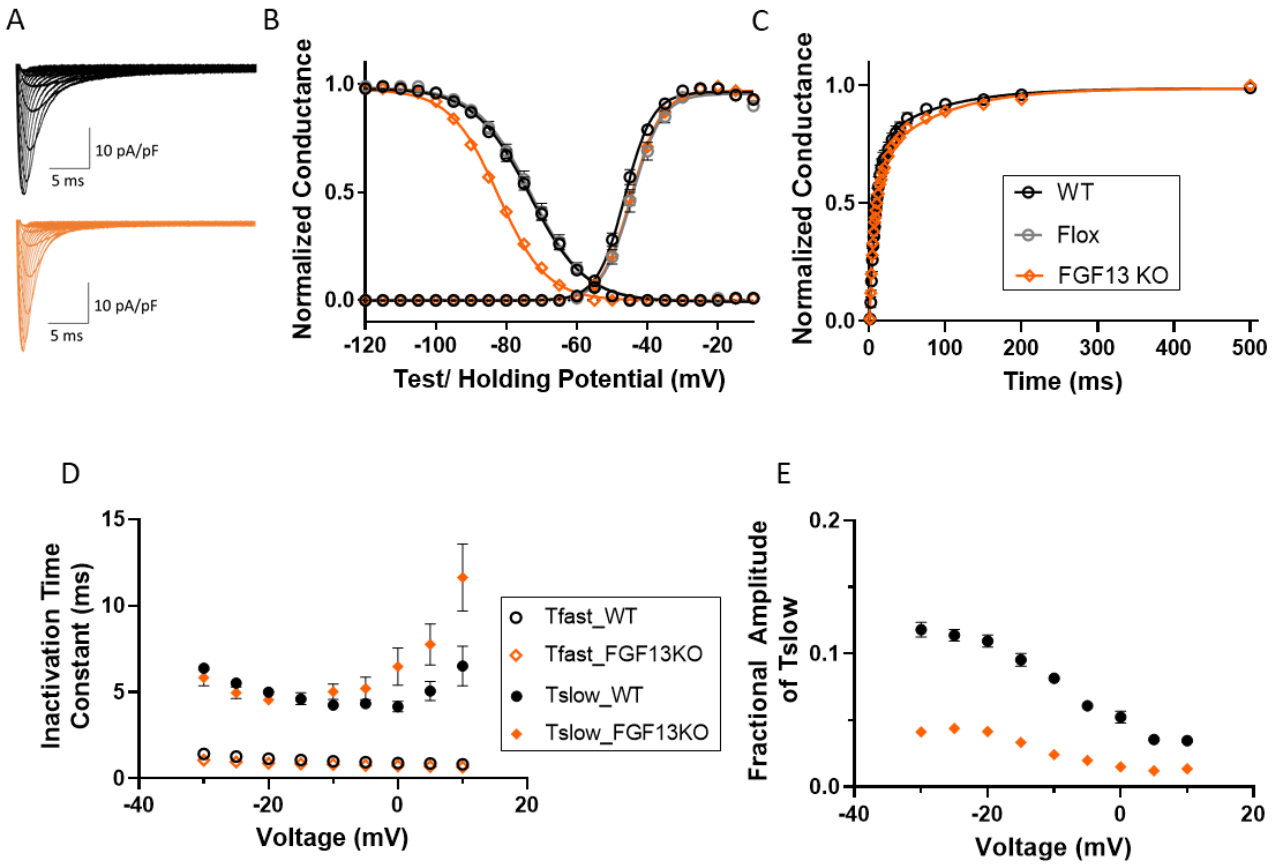

Figure 2.7: The effect of FGF13 in FGF13-knockout, relative to wild-type mice
(A) Exemplary I_{Na} traces from mouse ventricular myocytes of wild-type (WT) (black), and FGF13-knockout (FGF13KO) (orange) mice. **(B)** The voltage dependence of activation curve (G-V) was not affected by FGF13 knockout. However, the knockout of FGF13 caused a hyperpolarizing shift in steady-state inactivation (SSI) curve relative to WT and Flox (grey) mice. **(C)** The recovery from inactivation curves are not different between WT and FGF13KO mice. **(D)** The peak current decay traces were fitted to a double exponential function and the fast (open symbol) and slower (filled symbol) inactivation time constants were plotted. There was no differences between WT and FGF13KO mice in terms of inactivation time constant at hyperpolarizing potentials, but at depolarizing potentials, the knockout of FGF13 slowed down the slower inactivation. **(E)** The fractional amplitude of slower inactivation time constant was reduced upon FGF13 knockout over all membrane potentials.

Altogether, we observe similar effects of FGF12B and FGF13 in mice models on G-V and SSI curves, as in *Xenopus* oocytes. Deviations in inactivation kinetics between two expression systems imply complex gating that is influenced by other factors present in mouse myocytes such as β-subunits and post-translational modifications that may directly affect VSD-IV activation.

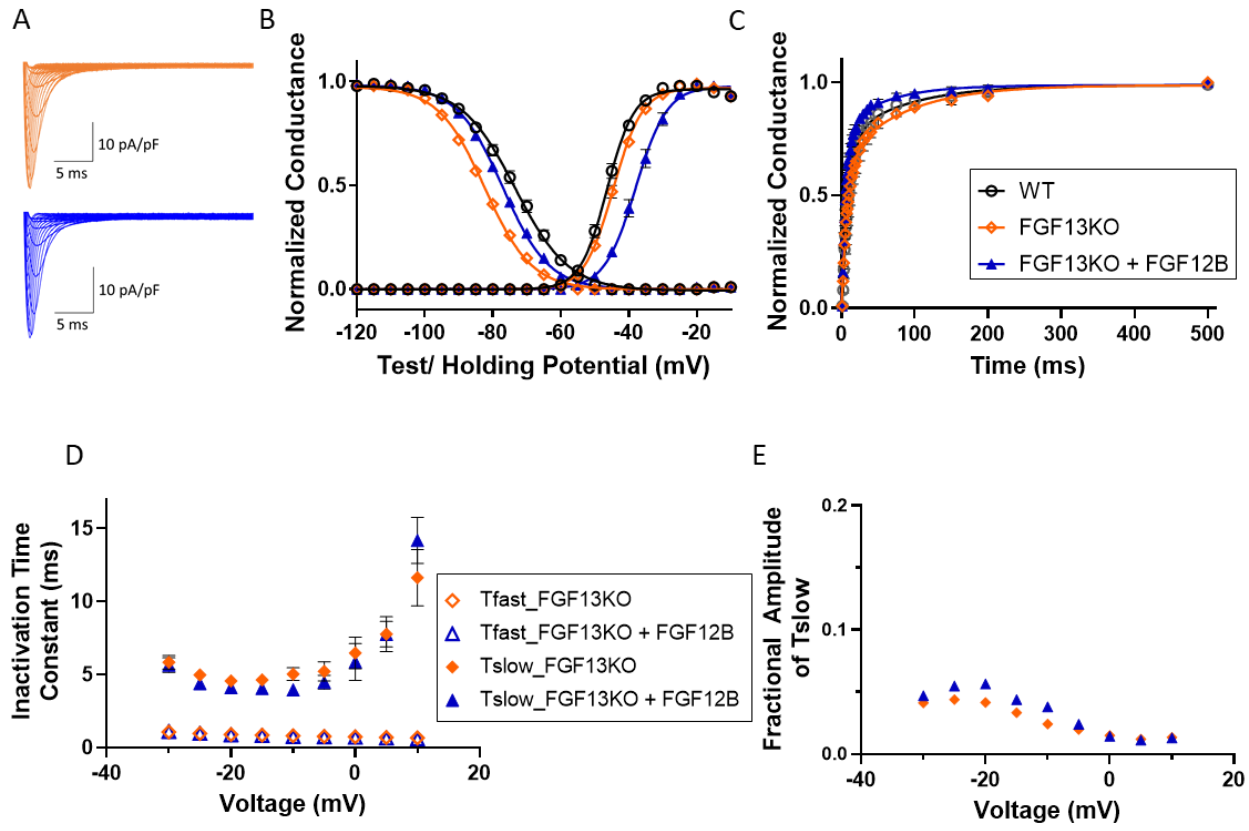

Figure 2.8: The effect of FGF12B in FGF13-knockout mice
(A) Exemplary I_{Na} traces from mouse ventricular myocytes of FGF13-knockout (FGF13KO) (orange), and FGF12B expressed in FGF13KO (FGF13KO + FGF12B) (blue) mice. **(B)** The GV and SSI curves were shifted towards depolarizing potentials by FGF12B expressed in FGF13KO mice (blue vs orange). The shift in SSI by FGF12B expression is not as depolarized as in WT (black) mice. **(C)** The recovery from inactivation was enhanced by FGF12B expression, relative to FGF13KO mice. **(D)** The fast (open symbol) and slower (filled symbol) inactivation time constants were not altered by FGF12B expression in FGF13KO mice. **(E)** The fractional amplitude of slower inactivation time constant was not affected by FGF12B expression, in comparison to FGF13KO mice.

Table 2.5: Fit parameters of IQM and E1784Q NaV1.5 alone and with FGF12B and FGF13VY co-expression

Parameter		**IQM $Na_V1.5$**	**IQM $Na_V1.5$ + FGF12B**	**IQM $Na_V1.5$ + FGF13VY**
GV				
	$V_{1/2}$ (n)	-20.7 ± 1.0 (5)	-30. 6 ± 0.7 (3)	-31.8 ± 0.4 (4)
	p-value		< 0.001 (***)	< 0.001 (***)
	k	8.5 ± 0.3	7.7 ± 0.9	5.2 ± 0.6
	p-value		0.5	0.003 (**)
SSI				
	$V_{1/2}$ (n)	-41.6 ± 0.7 (5)	-43.0 ± 0.9 (3)	-43.6 ± 0.4 (4)
	p-value		0.3	0.1
	k	3.6 ± 0.2	3.4 ± 0.1	4.0 ± 0.4
	p-value		0.9	0.5
VSD-IV FV				
	$V_{1/2}$ (n)	-59.7 ± 0.9 (3)	-70.5 ± 1.3 (3)	-54.4 ± 1.5 (3)
	p-value		0.002 (**)	0.05 (*)
	k	7.3 ± 0.9	7.0 ± 0.5	4.2 ± 1.5
	p-value		0.97	0.1
		E1784K $Na_V1.5$	**E1784K $Na_V1.5$ + FGF12B**	**E1784 K $Na_V1.5$ + FGF13VY**
GV				
	$V_{1/2}$ (n)	-20.7 ± 0.8 (5)	-20.2 ± 0.9 (5)	-25.0 ± 1.7
	p-value		0.95	0.04 (*)
	k	9.1 ± 0.1	9.0 ± 0.3	7.2 ± 0.3
	p-value		0.9	< 0.001 (***)
SSI				
	$V_{1/2}$ (n)	-101.9 ± 0.9 (5)	-113.3 ± 4.1 (5)	-91.8 ± 3.7 (4)
	p-value		0.04 (*)	0.09
	k	14.9 ± 0.3	19.3 ± 0.5	16.5 ± 1.6
	p-value		0.01 (**)	0.3
VSD-IV FV				
	$V_{1/2}$ (n)	-60.9 ± 2.9 (4)	-64.8 ± 2.3 (3)	-56.1 ± 1.0 (3)
	p-value		0.5	0.3
	k	19.5 ± 2.5	17.1 ± 1.8	12.9 ± 1.1
	p-value		0.7	0.1

Table 2.6: Fit parameters of I_{Na} recordings from mouse myocytes

Parameter		WT	Flox	FGF13 KO	FGF12B KO	FGF13KO + FGF12B
G-V	**$V_{1/2}$ (n)**	-46.3 ± 0.6 (24)	-44.1 ± 1.0 (15)	-44.4 ± 0.6 (26)	-44.6 ± 0.8 (19)	-37.48 ± 0.9 (19)
	p-value		0.11	0.12	0.24	< 0.001 (***)
	k	3.6 ± 0.1	2.9 ± 0.2	4.0 ± 0.1	3.7 ± 0.2	4.3 ± 0.1
	p-value		0.46	0.12	0.79	0.006 (**)
SSI	**$V_{1/2}$ (n)**	-73.4 ± 1.0 (24)	-72.8 ± 1.3 (15)	-82.5 ± 0.8 (26)	-70.1 ± 1.0 (19)	-77.2 ± 0.5 (17)
	p-value		0.97	< 0.001 (***)	0.06	0.02 (*)
	k	7.2 ± 0.1	7.1 ± 0.1	6.7 ± 0.2	7.2 ± 0.1	6.9 ± 0.1
	p-value		0.84	0.02 (*)	> 0.99	< 0.001 (***)
Recovery	**$T_{R,1}$ (n)**	8.1 ± 1.4 (7)		6.3 ± 0.9 (9)		4.0 ± 0.6 (9)
	$T_{R,2}$	87.8 ± 18.4		58.9 ± 8.4		28.2 ± 2.8
Peak decay						
At -20 mV	**T_{fast} (n)**	1.4 ± 0.1 (13)		1.0 ± 0.1 (12)		1.1 ± 0.1 (4)
	T_{slow}	6.1 ± 0.3		5.5 ± 0.5		5.7 ± 0.5
	A_{slow}	0.12 ± 0.02		0.041 ± 0.004		0.047 ± 0.01
At -25 mV	**T_{fast}**	1.2 ± 0.05		0.9 ± 0.1		1.0 ± 0.08
	T_{slow}	5.3 ± 0.3		4.7 ± 0.4		4.4 ± 0.2
	A_{slow}	0.11 ± 0.02		0.043 ± 0.003		0.055 ± 0.01
At -20 mV	**T_{fast}**	1.1 ± 0.05		0.8 ± 0.1		0.9 ± 0.06
	T_{slow}	4.8 ± 0.2		4.4 ± 0.3		4.1 ± 0.2
	A_{slow}	0.11 ± 0.02		0.039 ± 0.003		0.056 ± 0.01
At -15 mV	**T_{fast}**	1.0 ± 0.04		0.75 ± 0.07		0.8 ± 0.07
	T_{slow}	4.4 ± 0.2		4.3 ± 0.4		4.1 ± 0.4
	A_{slow}	0.095 ± 0.02		0.031 ± 0.003		0.044 ± 0.002
At -10 mV	**T_{fast}**	0.9 ± 0.04		0.71 ± 0.07		0.8 ± 0.05
	T_{slow}	4.1 ± 0.2		4.5 ± 0.5		4.0 ± 0.3
	A_{slow}	0.081 ± 0.01		0.022 ± 0.003		0.038 ± 0.002
At -5 mV	**T_{fast}**	0.9 ± 0.04		0.67 ± 0.07		0.7 ± 0.05
	T_{slow}	4.2 ± 0.3		4.3 ± 0.8		4.5 ± 0.5
	A_{slow}	0.061 ± 0.01		0.018 ± 0.002		0.024 ± 0.003
At 0 mV	**T_{fast}**	0.8 ± 0.04		0.64 ± 0.07		0.7 ± 0.05
	T_{slow}	4.1 ± 0.4		5.0 ± 1.3		5.8 ± 1.3
	A_{slow}	0.052 ± 0.02		0.013 ± 0.002		0.014 ± 0.002
At 5 mV	**T_{fast}**	0.8 ± 0.05		0.61 ± 0.07		0.6 ± 0.04
	T_{slow}	5.1 ± 0.7		5.8 ± 1.4		7.7 ± 0.9
	A_{slow}	0.035 ± 0.01		0.010 ± 0.002		0.011 ± 0.005
At 10 mV	**T_{fast}**	0.7 ± 0.05		0.58 ± 0.07		0.6 ± 0.03
	T_{slow}	6.6 ± 1.4		8.3 ± 2.3		14.2 ± 1.6
	A_{slow}	0.034 ± 0.01		0.012 ± 0.002		0.013 ± 0.007

2.4 Discussion

Na_V channels in cardiac cells are formed by macromolecular complexes, modulated by myriad auxiliary subunits. Study of the underlying mechanism of particular subunits within a native myocyte environment could be challenging. In this work, we employed the heterologous expression system of *Xenopus* oocytes to delineate the mechanistic detail of iFGF modulation of cardiac $Na_V1.5$ function and compared to native cell regulation.

2.4.1 Differential modulations of $Na_V1.5$ by FGF12B and FGF13VY

We studied the effects of FGF12B and FGF13VY on human $Na_V1.5$. We chose two 2 highly expressed iFGFs in human and mouse hearts as the representatives of different iFGFs. In *Xenopus* oocytes, both iFGFs induced the same depolarizing shift in SSI, but a larger magnitude of alteration in $V_{1/2}$ by FGF13VY. Both FGF12B and FGF13VY caused the faster decay of I_{Na}, which can be characterized as the reduction in the slower component of inactivation. A comparison also showed differences in the magnitude of this reduction, a larger reduction by FGF13VY, more prominently at depolarized potentials.

Although we observed a depolarizing shift in G-V by FGF12B, further investigation showed it was likely due to the tightly coupled activation and inactivation kinetics (Keynes, 1992). In mutant $Na_V1.5$ that we remove the inactivation gate (IQM mutation), FGF12B no longer caused the shift in SSI, nor the G-V. The faster inactivation, induced by iFGF, potentially leading to the reduction in the apparent channel conductance and hence the shift in G-V. The larger amount of channel availability in the presence of FGF13VY could negate a shift in the G-V curve by iFGF.

2.4.2 Distinct iFGF regulation of VSD-IV activation

The VCF results revealed the effects of FGF12B and FGF13VY on the regulation of VSD-IV activation. Their distinct modulation on VSD-IV F-V curve was observed, and can be characterized by differences in

Boltzmann fit parameters, $V_{1/2}$ and k. Both iFGFs induced the hyperpolarizing shift in $V_{1/2}$ and the steeper slope or reduced k, but with differing degree of alteration. The prominent FGF12B effect is in $V_{1/2}$, shifting it to more hyperpolarized potentials, whereas FGF13VY markedly decreased k to a smaller value. The hyperpolarizing shift in $V_{1/2}$ indicates the facilitated activation of VSD-IV at less depolarized potentials, while the steeper slope signifies the accelerated completion of VSD-IV activation due to more charges being transferred.

Previous VCF studies demonstrated that the activation of VSD-IV correlates to the onset of fast inactivation (Chanda and Bezanilla, 2002) (Capes et al., 2013). Site-3 toxins, that bind to the extracellular loop near IV S4 and inhibit the outward translation of VSD-IV, prevent the Na_V channel transition into fast inactivation (Hanck and Sheets, 2007) (Campos et al., 2004). This implies the full activation of VSD-IV is necessary for the entry into the fast inactivated state (Campos and Beirão, 2006) (Campos et al., 2008) (Jiang et al., 2021a) (Jiang et al., 2021b). Modulation by both FGF12B and FGF13VY is consistent with the decrease in the slower component of channels inactivation from open state. In other words, iFGF promotes fast inactivation, by facilitating the VSD-IV activation and accelerating its completion.

This modulation of VSD-IV may be the direct effect of iFGF binding to the Na_V C-terminal domain (CTD) as hypothesized previously from the chimeric structures of Na_VPaS-hNa_V1.7 in complex with the α-scorpion toxin (Clairfeuille et al., 2019). The resting conformation of VSD-IV was shown to interact with the Na_V CTD, which in turn sequesters the III-IV linker (Clairfeuille et al., 2019). Although the nature of this interaction is called into question by the non-functionality of Na_VPaS channel and the absence of resolved CTD in other hNa_V channels, the mutations that likely disrupt this interaction were tested in Na_V1.5 to support the claim. The binding of iFGF could affect the conformation of the CTD so that it breaks contact with VSD-IV and as a result VSD-IV can activate at hyperpolarizing potentials.

The sole modulation of VSD-I activation by FGF13VY suggests the possible role of long N-terminus in altering the coupling between VSDs of different repeats. Multiple electrophysiological studies supported the

tightly coupled interactions between VSDs (Vandenberg and Bezanilla, 1991) (Keynes and Elinder, 1998) (Chanda et al., 2004) (Campos et al., 2008), especially between repeats I and IV where the domain-swapped architecture places the VSD-I close to S5-S6 of repeat IV. However, the binding of local anesthetic (LA) drugs to the channel pore can modify the coupling between VSDs (Muroi and Chanda, 2009). Possibly, the long FGF13VY N-terminus might interact with the channel pore and remodel the coupling interactions between voltage sensors (White et al., 2019) (Yan et al., 2014). FGF12B, which bears much shorter N-terminus hence lacks its effect on VSD-I activation.

2.4.3 iFGF chimera experiments reveal the significance of VSD-IV activation on $Na_V1.5$ inactivation

We used chimera experiments to identify the key iFGF domain responsible for its unique VSD-IV regulation. Surprisingly, results showed that not only N-terminus, but all three domains combined (N-terminus, core, and C-terminus) contribute to unique regulatory effect of each iFGF. According to the structures of $Na_V1.5$ CTD in complex with FGF13 and calmodulin (Goetz et al., 2009) (Wang et a., 2012) (Musa et al., 2015) (Hennessey et al., 2013), the iFGF binding sites reside within the core domain. Interestingly, the FGF12 structures show that its C-terminal residues can interact with the core region, and possibly the N-terminus (Goetz et al., 2009). A disruption of Na_V channel and iFGF interaction interfaces at different sites leads to differential effects on I_{Na} (Singh et al., 2021). These evidence supports the possibility that unique sequence of iFGF leads to differential binding conformation on the Na_V CTD and consequently its distinct modulation of VSD-IV activation.

We then used results from iFGF chimera experiments to analyze the significance of VSD-IV activation on Na_V channel gatings, by performing linear regression analysis. We discovered a good correlation and a high predictability by VSD-IV parameters on I_{Na} decay kinetics, in particular the slower inactivation time constants and the fraction of channels undergoing this mode of inactivation. Further mutagenesis study revealed the iFGF-mediated shifts in SSI requires the inactivation gate, and the interaction between Na_V CTD and III-IV linker. iFGF potentially affects the interaction of Na_V CTD and III-IV linker, that is essential for the release of

an inactivation gate.

Based upon the two-switch model proposed by Clairfeuille et al., during resting state, the Na_V CTD can interact with (1) VSD-IV S4 and (2) III-IV linker (Clairfeuille et al., 2019). The activation of VSD-IV severs the first interaction and subsequently releases III-IV linker from the CTD. The binding of iFGF might modulate these two interactions in two ways: (1) iFGF reduces the CTD interaction with VSD-IV and promotes its activation (2) iFGF enhances the CTD interaction with III-IV linker and reduces the probability of closed-state inactivation, resulting in an increased steady-state channel availability (Angsutararux et al., 2021a). iFGF also facilitates recovery from inactivation, the process depending on both the movement of IFMT motif and VSD-III and VSD-IV deactivation (Hsu et al., 2017).

2.4.4 Physiological significance

The *Xenopus* oocytes heterologous expression system provides insight into mechanisms of iFGF regulation of Na_V channel gating. We observed in FGF13KO mice the consistent effects of iFGF modulation of $Na_V1.5$ G-V and SSI. Previous studies reported a similar FGF13 effect on the modulation of SSI in mice myocytes (Wang et al., 2011a) (Park et al., 2016) (Wang et al., 2017) (Park et al., 2020). Yet, there were some dissimilarities between studies. Past experiments reported the reduced I_{Na} amplitude and a slower recovery from inactivation upon FGF13 knockout or knockdown (Wang et al., 2011a) (Park et al., 2016) (Wang et al., 2017) (Park et al., 2020). However, we observed no change in either peak current density of the rate of recovery from inactivation, in comparison to WT and Floxed mice. The disagreement might arise from the different technique used for gene knockout or variations in recording protocols. The effects of FGF12B were also translated from *Xenopus* oocytes to mouse myocytes. Even the magnitude difference in the shifts of $V_{1/2}$ between FGF12B and FGF13VY, was reflected in the mouse model.

The kinetics of Na_V channel inactivation, however, were different between 2 expression systems. As demonstrated in previous study (Park et al., 2016), the knockout of FGF13 caused an apparently faster current

decay. An analysis showed the reduced fraction of slower inactivation component in FGF13KO mice, which is the opposite effect of FGF13VY reported in *Xenopus* oocytes. This discrepancy might be due to the presence of other factors in native cardiomyocyte that can also affect the VSD-IV activation and hence inactivation kinetics, such as β-subunit (Zhu et al., 2017) (Zhu et al., 2021), Calmodulin (CaM) and intracellular Ca^{2+} (Gade et al., 2020) (Abrams et al., 2020). Post-translational modifications like phosphorylation can also affect the binding of iFGF on the CTD (Burel et al., 2017) (Iqbal and Lemmens-Gruber, 2019) (Lorenzini et al., 2021). The synergistic effects of multiple regulatory proteins can potentially lead to these deviations perceived between different study systems.

2.5 Conclusion

In this study, we demonstrated the significant regulation of VSD-IV activation by iFGF. The facilitated activation and accelerated completion of VSD-IV movement by iFGF reduce the slower component of inactivation, after channel opening. We also showed the differential magnitude of SSI shifts by FGF12B and FGF13VY are the result of distinct iFGF regulation of VSD-IV activation kinetics, and potentially a modulation of CTD interaction with III-IV linker. FGF13VY induced a larger depolarizing shift in SSI because of its faster completion of VSD-IV activation, contributing to the less fraction of channel entering slower mode of inactivation. As a result, with FGF13VY, channels can recover faster and thus the larger number of channels are available to open. The ability to modulate VSD-IV activation, however, is not unique to iFGF. Other regulatory proteins such as β-subunits, toxins, and antiarrhythmic drugs could all modulate VSD-IV and cause distinct effects in Na_V channel inactivation kinetics. Our work suggests a new mechanistic model of Na_V channel regulation that relies on VSD-IV as a signaling hub to determine inactivation gating.

2.6 Materials and Methods

2.6.1 Molecular biology

Point mutations were made in SCN5A, FGF12B and FGF13VY genes with the QuikChange II site-directed mutagenesis kit (Agilent) with primers from Sigma-Aldrich containing the mutation. The DNA of iFGF chimeras was synthesized by GeneArt Gene Synthesis (Thermo Fisher Scientific). All mutations and chimeras were confirmed with DNA sequencing. The complementary RNA (cRNA) was synthesized with the mMessage mMACHINE T7 Transcription kit (Life Technologies) after linearizing DNA with appropriate restriction enzyme and purifying with the NucleoSpin Gel and PCR Clean-up kit (Macherey-Nagel). The final cRNA was reconstituted with ddH_2O to a concentration of ~1 µg/µl.

2.6.2 Cut-Open oocyte and voltage-clamp fluorometry (VCF)

Oocytes were harvested from *Xenopus laevis* by laparotomy according to an animal protocol approved by the Washington University Animal Studies Committee, and digested with collagenase (Sigma-Aldrich, St. Louis, MO). Oocytes were injected with cRNAs and incubated in ND93 solution (93 NaCl mM, 5 KCl mM, 1.8 $CaCl_2$ mM, 1 $MgCl_2$ mM, 5 HEPES mM, 2.5 Na pyruvate mM, and 1% penicillin–streptomycin, pH 7.4) at 18°C for 3-6 days prior to recording. A total of 50-56 ng cRNA was injected per oocyte. For iFGF co-expression experiments, iFGF was co-injected with $hNa_V1.5$ at a 4:1 molar ratio.

Cut-open recordings were performed at 19°C with a temperature controller (HCC-100A; Dagan Corporation), using a cut-open amplifier (CA-1B; Dagan Corporation) coupled to an A/D converter (Digidata 1440; Molecular Devices). Data were collected through Clampex software (Molecular Devices) and analyzed with Clampfit (Molecular Devices). The internal recording solution was composed of 105 mM NMG-Mes, 10 mM Na-Mes, 20 mM HEPES, and 2 mM EGTA, at a pH level of 7.4 and the external recording solution contained 25 mM NMG-Mes, 90 mM Na-Mes, 20 mM HEPES, and 2 mM $Ca\text{-}Mes_2$, at a pH level of 7.4.
For VCF, the oocytes were labeled for 30 minutes on ice with 10 µmol/L of methanethiosulfonate-

carboxytetramethylrhodamine (MTS-TAMRA; Santa Cruz Biotechnology) in a depolarizing solution composed of 110 mM KCl, 1.5 mM MgCl2, 0.8 mM CaCl2, 0.2 mM EDTA and 10 mM HEPES at a pH of 7.1. Simultaneous recordings of ionic current and fluorescence emissions were collected on a custom rig (Rudokas et al., 2014) (Varga et al., 2015) (Zhu et al., 2017). Fluorescence emission was measured by a photodiode (PIN-040A; United Detector Technology) and a patch clamp amplifier (Axopatch-200A; Molecular Devices), after teal LED light illumination by the SPECTRA X (Lumencor, OR).

2.6.3 Electrophysiology data analysis

Recordings were analyzed with Clampfit (Molecular Devices), and Excel (Microsoft). Steady-state activation protocols were tested from -120 to 60 mV for 100 ms with -120 mV pre- and post-pulses holding for 100 ms. The calculated conductance was normalized to the maximum conductance at 20 mV. For steady-state inactivation curve, cells were preconditioned at voltages ranging from -150 to 20 mV for 200 ms, the channel availability was then tested at -20 mV. The normalized conductance-voltage (G-V), and steady-state inactivation (SSI) curves were fitted to a Boltzmann equation (Eq.1).

$$G(V) = 1/(1+\exp[-(V-V_{1/2})/k]) \qquad \text{(Eq.1)}$$

where $V_{1/2}$ is the half-activation voltage and k is the slope factor

Fast inactivation kinetics were calculated by fitting the peak current decay to a double exponential function (Eq.2).

$$I(t) = \text{offset} - a_1\exp(t/\tau_{fast}) - a_2\exp(t/\tau_{slow}) \qquad \text{(Eq.2)}$$

where a_1 and a_2 are amplitudes for fast and slow components of inactivation and τ_{fast} and τ_{slow} are time constants of inactivation.

Recovery from inactivation was determined by a double pulse protocol with varying recovery duration between two pulses. The first depolarizing pulse was applied at -20 mV for 200 ms to induce the fast inactivation and the second 20 ms pulse at -20 mV pulse was used to test the channel availability after

recovery period. The recovery duration was measured from 1-1000 ms. The normalized recovery curve was fit to a double exponential equation (Eq.3).

$$I(t) = \text{offset} - a_1\exp(t/\tau_{R,1}) - a_2\exp(t/\tau_{R,2}) \qquad \text{(Eq.3)}$$

where a_1, a_2 are the current amplitudes at non-zero recovery and $\tau_{R,1}$, $\tau_{R,2}$ are the recovery time constants. The fluorescence signals were low-pass filtered at 1kHz and corrected for photo-bleaching following baseline subtraction. A fluorescence trace obtained at -120 mV, which is the holding potential, was fitted as a model for the calculation of baseline traces with no change in fluorescence at other potentials. The voltage-dependence of normalized steady-state fluorescence emission (F-V) curve was fitted to a Boltzmann equation (Eq.4).

$$F(V) = 1/(1+\exp[(-V-V_{1/2})/k]) \qquad \text{(Eq.4)}$$

Statistical analyses were performed using Student's t-tests, linear regression and multiple linear regression with Prism9 (Graph Pad, CA).

2.7 References

Abrams, J., Roybal, D., Chakouri, N.,…, and S.O. Marx. 2020. Fibroblast growth factor homologous factors tune arrhythmogenic late NaV1.5 current in calmodulin binding-deficient channels. *JCI Insight*. 5(19):e141736. Doi: 10.1172/jci.insight.141736.

Abriel, H. 2010. Cardiac sodium channel Na(v)1.5 and interacting proteins: physiology and pathophysiology. *J Mol Cell Cardiol*. 48:2-11. Doi: 10.1016/j.yjmcc.2009.08.025.

Abriel, H., and R.S. Kass. 2005. Regulation of the voltage-gated cardiac sodium channel $Na_V1.5$ by interacting proteins. *Trends Cardiovasc Med*. 15(1):35-40. Doi: 10.1016/j.tcm.2005.01.001.

Angsutararux, P., Kang, P.W., Zhu, W., and J.R. Silva. 2021a. Conformations of voltage-sensing domain III differentially define Na_V channel closed- and open-state inactivation. *J Gen Physiol*. 153(9):e202112891. Doi: 10.1085/jgp.202112891.

Angsutararux, P., Zhu, W., Voelker, T.L., and J.R. Silva. 2021b. Molecular pathology of sodium channel beta-subunit variants. *Front Pharmacol*. 12:3220. Doi: 10.3389/fphar.2021.761275.

Barbosa, C., Xiao, Y., Johnson, A.J.,…, and T.R. Cummins. 2017. FHF2 isoforms differentially regulate NaV1.6-mediated resurgent sodium currents in dorsal root ganglion neurons. *Pflugers Arch*. 469(2):195-212.

Doi: 10.1007/s00424-016-1911-9.

Burel, S., Coyan, F.C., Lorenzini, M.,…, and Marionneau, C. 2017. C-terminal phosphorylation of $Na_V1.5$ impairs FGF13-dependent regulation of channel inactivation. *J Biol Chem*. 292(42):17431-48. Doi: 10.1074/jbc.M117.787788.

Calhoun, J.D., and L.L Isom. 2014. The role of non-pore-forming β subunits in physiology and pathophysiology of voltage-gated sodium channels. *Handb Exp Pharmacol*. 221:51-89. Doi: 10.1007/978-3-642-41588-3_4.

Campos, F.V., Coronas, F.I.V., P.S.L. Beirão. 2004. Voltage-dependent displacement of the Scorpion toxin Ts3 from sodium channels and its implication on the control of inactivation. *Br J Pharmacol*. 142(7):1115-22. Doi: 10.1038/sj.bjp.0705793.

Campos, F.V., and P.S.L., Beirão. 2006. Effects of bound ts3 on voltage dependence of sodium channel transitions to and from inactivation and energetics of its unbinding. *Cell Biochem Biophys*. 44(3):424-30. Doi: 10.1385/CBB:44:3:424.

Campos, F.V., Chanda, B., Beirão, P.S.L., and F. Bezanilla. 2008. α-scorpion toxin impairs a conformational change that leads to fast inactivation of muscle sodium channels. *J Gen Physiol*. 132(2):251-263. Doi: 10.1085/jgp.200809995.

Capes, D.L., Goldschen-Ohm, M.P., Arcisio-Miranda, M., Bezanilla, F., and B. Chanda. 2013. Domain IV voltage-sensor movement is both sufficient and rate limiting for fast inactivation in sodium channels. *J Gen Physiol*. 142:101-112. Doi: 10.1085/jgp.201310998.

Chahine, M., George Jr, A.L., Zhou, M., Ji, W., Sun, W., Barchi, R.L., and R. Horn. 1994. Sodium channel mutations in paramyotonia congenita uncouple inactivation from activation. *Neuron*. 12(2):281-294. Doi: 10.1016/0896-6273(94)90271-2.

Chanda, B., and F. Bezanilla. 2002. Tracking voltage-dependent conformational changes in skeletal muscle sodium channel during activation. *J Gen Physiol*. 120:629-645. Doi: 10.1085/jgp.20028679.

Chanda, B., Asamoah, O.K., and F. Bezanilla. 2004. Coupling interactions between voltage sensors of the sodium channel as revealed by site-specific measurements. *J Gen Physiol*. 123(3):217-230. Doi: 10.1085/jgp.200308971.

Clairfeuille, T., Cloake, A., Infield, D.T.,…, and Payandeh, J. 2019. Structural basis of α-scorpion toxin action on NaV channels. *Science*. 363(6433):eaav8573. Doi: 10.1126/science.aav8573.

Gade, A.R., Marx, S.O., and G.S. Pitt. 2020. An interaction between the III-IV linker and CTD in $Na_V1.5$ confers regulation of inactivation by CaM and FHF. *J Gen Physiol*. 152(2):e201912434. Doi: 10.1085/jgp.201912434.

Gandhi, C.S., and R. Olcese. 2008. The voltage-clamp fluorometry technique. Methods Mol Biol. 491:213-231. Doi: 10.1007/978-1-59745-526-8_17.

Gardill, B.R., Rivera-Acevedo, R.E., Tung, C.C., Okon, M., McIntosh, L.P., and F.V. Petegem. 2018. The voltage-gated sodium channel EF-hands form an interaction with the III-IV linker that is disturbed by disease-causing mutations. *Sci Rep*. 8:4483. Doi: 10.1038/s41598-018-22713-y.

Gardill, B.R., Rivera-Acevedo, R.E., Tung, C.C., and F.V. Petegem. 2019. Crystal structures of Ca^{2+}-calmodulin bound to Na_V C-terminal regions suggest role for EF-hand domain in binding and inactivation. *Proc Natl Acad Sci USA*. 116(22):10763-72. Doi: 10.1073/1818618116.

Goetz, R., Dover, K., Laezza, F.,…, and M. Mohammadi. 2009. Crystal structure of a fibroblast growth factor homologous factor (FHF) defines a conserved surface on FHFs for binding and modulation of votlage-gated sodium channels. *J Biol Chem*. 284(26):17883-96. Doi: 10.1074/jbc.M109.001842.

Goldfarb, M. 2005. Fibroblast growth factor homologous factors: evolution, structure, and function. *Cytokine Growth Factor Rev*. 16(2):215-220. Doi: 10.1016/j.cytogfr.2005.02.002.

Goldfarb, M., Schoorlemmer, J., Williams, A.,…, and D'Angelo, E. 2007. Fibroblast growth factor homologous factors control neuronal excitability through modulation of voltage-gated sodium channels. *Neuron*. 55(3):449-463. Doi: 10.1016/j.neuron.2007.07.006.

Hanck, D.A., and M.F. Sheets. 2007. Site-3 toxins and cardiac sodium channels. *Toxicon*. 49(2):181-193. Doi: 10.1016/j.toxicon.2006.09.017.

Hartmann, H.A., Tiedeman, A.A., Chen, S.F., Brown, A.M., and G.E. Kirsch. 1994. Effects of III-IV linker mutations on human heart Na^+ channel inactivation gating. *Circ Res*. 75(1):114-122. Doi: 10.1161/01.RES.75.1.114.

Hennessey, J.A., Marcou, C.A., Wang, C.,…, and G.S. Pitt. 2013. FGF12 is a candidate Brugada syndrome locus. *Hearth Rhythm*. 10(12):1886-94. Doi: 10.1016/j.hrthm.2013.09.064.

Horn, R., Ding, S., and H.J. Gruber. 2000. Immobilizing the moving parts of voltage-gated ion channels. *J Gen Physiol*. 116(3):461-476. Doi: 10.1085/jgp.116.3.461.

Hsu, E.J., Zhu, W., Schubert, A.R., VoelKer, T., Varga, Z., and J.R. Silva. 2017. Regulation of Na+ channel inactivation by the DIII and DIV voltage-sensing domains. *J Gen Physiol*. 149(3):389-403. Doi: 10.1085/jgp.201611678.

Igbal, S.M., and R. Lemmens-Gruber. 2019. Phosphorylation of cardiac voltage-gated sodium channel: potential players with multiple dimensions. *Acta Physiol (Oxf)*. 225(3):e13210.

Jiang, D., Siu, H., Tonggu, L.,…, and W.A. Catterall. 2020. Structure of the cardiac sodium channel. *Cell*. 180(1):122-134.e10. Doi: 10.1016/j.cell.2019.11.041.

Jiang, D., Tonggu, L., Gamal El-Din, T.M.,…, and W.A. Catterall. 2021a. Structural basis for voltage-sensor trapping of the cardiac sodium channel by a deathstalker scorpion toxin. *Nat Commun*. 12(1):128. Doi: 10.1038/s41467-020-20078-3.

Jiang, D., Bahn, R., Gamal El-Din, T.M.,…, and W.A. Catterall. 2021b. Open-state structure and pore gating mechanism of the cardiac sodium channel. *Cell*. 184(20):5151-62. Doi: 10.1016/j.cell.2021.08.021.

Keynes, R.D. 1992. A new look at the mechanism of activation and inactivation of voltage-gated ion channels. *Proc R Soc Land*. 249:107-112.

Keynes, R.D., and F. Elinder. 1998. On the slowly rising phase of the sodium gating current in the squid giant axon. *Proc Biol Sci*. 265(1393):255-262. Doi: 10.1098/rspb.1998.0290.

Kuhn, F.J., and N.G., Greeff. 1999. Movement of voltage sensor S4 in domain 4 is tightly coupled to sodium channel fast inactivation and gating charge immobilization. *J Gen Physiol*. 114(2):167-183. Doi: 10.1085/jgp.114.2.167.

Laezza, F., Lampert, A., Kozel, M.A.,…, and D.M. Ornitz. 2009. FGF14 N-terminal splice variants diffrerntially modulate NaV1.2 and NaV1.6-encoded sodium channels. Mol Cell Neurosci. 42(2):90-101. Doi: 10.1016/j.mcn.2009.05.007.

Li, Q., Zhao, Y., Wu, G.,…, and X. Tu. 2017. De novo FGF12 (Fibroblast growth factor 12) functional variation is potentially associated with idiopathic ventricular tachycardia. J Am Heart Assoc. 6(8):e006130. Doi: 10.1161/JAHA.117.006130.

Liu, C.J., Dib-Haji, S.D., and S.G. Waxman. 2001. Fibroblast growth factor homologous factor 1B binds to the C terminus of the tetrodotoxin-resistant sodium channel rNaV1.9a (NaN). *J Biol Chem*. 276(22):18925-33. Doi: 10.1074/jbc.M101606200.

Liu, C.J., Dib-Haji, S.D., Renganathan, M., Cummins, T.R., and S.G. Waxman. 2003. Modulation of the cardiac sodium channel NaV1.5 by fibroblast growth factor homologous factor 1B. *J Biol Chem*. 278(2):1029-36. Doi: 10.1074/jbc.M207074200.

Lorenzini, M., Burel, S., Lesage, A.,…, and Marionneau, C. 2021. Proteomic and functional mapping of cardiac NaV1.5 channel phosphorylation sites. *J Gen Physiol*. 153(2):e202012646. Doi: 10.1085/jgp.202012646.

Lou, J.Y., Laezza, F., Gerber, B.R.,…, and D.M. Ornitz. 2005. Fibroblast growth factor 14 is an intracellular modulator of voltage-gated sodium channels. *J Physiol*. 569(1):179-193. Doi: 10.1113/jphysiol.2005.097220.

Mangold, K.E., Brumback, B.D., Angsutararux, P.,…, and J.R. Silva. 2017. Mechanisms and models of cardiac sodium channel inactivation. *Channels (Austin)*. 11(6):517-33. Doi: 10.1080/19336950.2017.1369637.

Mannuzzu, L.M., Moronne, M.M., and E.Y. Isacoff. 1996. Direct physical measure of conformational rearrangement underlying potassium channel gating. *Science*. 271:213-216. Doi: 10.1126/science.271.5246.213.

Meadows, L.S., and L.L. Isom. 2005. Sodium channels as macromolecular complexes: implications for inherited arrhythmia syndromes. *Cardiovasc Res*. 67(3):448-58. Doi: 10.1016/j.cardiores.2005.04.003.

Mori, M., Konno, T., Morii, T., Nagayama, K., and K. Imoto. 2003. Regulatory interaction of sodium channel IQ-motif with calmodulin C-terminal lobe. *Biochem Biophys Res Commun*. 307:290-296. Doi: 10.1016/s0006-291x(03)01183-5.

Munoz-Sanjuan, I., Smallwood, P.M., and J. Nathans. 2000. Isoform diversity among fibroblast growth factor homologous factors is generated by alternative promoter usage and differential splicing. *J Biol Chem*. 275(4):2589-97. Doi: 10.1074/jbc.275.4.2589.

Muroi, Y., and B. Chanda. 2009. Local anesthetics disrupt energetic coupling between the voltage-sensing segments of a sodium channel. *J Gen Physiol*. 133(1):1-15. Doi: 10.1085/jgp.200810103.

Musa, H., Kline, C.F., Sturm, A.C.,…, and P.J. Mohler. 2015. SCN5A variant that blocks fibroblast growth factor homologous factor regulation causes human arrhythmia. *Proc Natl Acad Sci USA*. 112:12528-33. Doi:

10.1073/pnas.1516430112.

Noble, D., and P.J. Noble. 2006. Late sodium current in the pathophysiology of cardiovascular disease: consequences of sodium-calcium overload. *Heart*. 92(Suppl 4): iv1-iv5. Doi: 10.1136/hrt.2005.078782.

Nof, E., Vysochek, L., Meisel, E.,…, and S. Oz. 2019. Mutations in $Na_V1.5$ reveal calcium-calmodulin regulation of sodium channel. *Front Physiol*. 10:700. Doi: 10.3389/fphy.2019.00700.

Olsen, S.K., Garbi, M., Zampieri, N.,…, and M. Mohammadi. 2003. Fibroblast growth factor (FGF) homologous factors share structural but not functional homology with FGFs. *J Biol Chem*. 278(36):34226-36. Doi: 10.1074/jbc.M303183200.

Pablo, J.L., and G.S. Pitt. 2017. Fibroblast growth factor homologous factors (FHFs): new roles in neuronal health and disease. *Neuroscientist*. 22(1):19-25. Doi: 10.1177/1073858414562217.

Pan, X., Li, Z., Zhou, Q.,…, and N. Yan. 2018. Structure of the human voltage-gated sodium channel $Na_V1.4$ in complex with β1. *Science*. 362(6412):eaau2486. Doi: 10.1126/science.aau2486.

Park, D.S., Shekhar, A., Marra, C.,…, and G.I. Fishman. 2016. Fhf2 gene deletion causes temperature-sensitive cardiac conduction failure. *Nat Commun*. 7:12966. Doi: 10.1038/ncomms12966.

Park, D.S., Shekhar, A., Santucci III, J.,…, and G.I. Fishman. 2020. Ionic mechanisms of impulse propagation failure in the FHF2-deficient heart. *Circ Res*. 127(12):1536-48. Doi: 10.1161/CIRCRESAHA.120.317349.

Peters, C.H., Watkins, A.R., Poirier, O.L., and P.C. Ruben. 2020. E1784K, the most common Brugada syndrome and long-QT syndrome type 3 mutant, disrupts sodium channel inactivation through two separate mechanisms. *J Gen Physiol*. 152(9):e202012595. Doi: 10.1085/jgp.202012595.

Pitt, G.S., and S.Y. Lee. 2016. Current view on regulation of voltage-gated sodium channels by calcium and auxiliary proteins. *Protein Sci*. 25(9):1573-84. Doi: 10.1002/pro.2960.

Ruan, Y., Liu, N., and Priori, S.G. 2009. Sodium channel mutations and arrhythmias. *Nat Rev Cardiol*. 6(5):337-348. Doi: 10.1038/nrcardio.2009.44.

Rudokas, M.W., Varga, Z., Schubert, A.R., Asaro, A.B., and Silva, J.R. 2014. The Xenopus oocyte cut-open Vaseline gap voltage-clamp technique with fluorometry. *J Vis Exp*. 11(85):51040. doi:10.3791/51040.

Scheuer, T. 2011. Regulation of sodium channel activity by phosphorylation. Semin Cell Dev Biol. 22(2):160-165. Doi: 10.1016/j.semcdb.2010.10.002.

Sheets, M.F., Kyle, J.W., Kalien, R.G., and D.A. Hanck. 1999. The Na channel voltage sensor associated with inactivation is localized to the external charged residues of domain IV, S4. *Biophys J*. 77(2):747-757. Doi: 10.1016/S0006-3495(99)76929-8.

Shen, H., Zhou, Q., Pan, X.,…, and Yan, N. 2017. Structure of a eukaryotic voltage-gated sodium channel at near-atomic resolution. *Science*. 355(6328):eaal4326. Doi: 10.1126/science.aal4326.

Siekierska, A., Isrie, M., Liu, Y.,…, and Buyse, G.M. 2016. Gain-of-function FHF1 mutation causes early-onset epileptic encephalopathy with cerebellar atrophy. *Neurology*. 86(23):2162-2170.

Silva J. 2014. Slow inactivation of Na(+) channels. *Handb Exp Pharmacol*. 221:33-49.

Silva, J.R., and Goldstein, S.A. 2013a. Voltage-sensor movements describe slow inactivation of voltage-gated sodium channels I: wild-type skeletal muscle Na(V)1.4. *J Gen Physiol*. 141(3):309-321.

Silva, J.R., and Goldstein, S.A. 2013b. Voltage-sensor movements describe slow inactivation of voltage-gated sodium channels II: a periodic paralysis mutation in Na(V)1.4 (L689I). *J Gen Physiol*. 141(3):323-334.

Singh, A.K., Dvorak, N.M., Tapia, C.M.,…, and F. Laezza. 2021. Differential modulation of the voltage-gated Na+ channel 1.6 by peptides derived from fibroblast growth factor 14. Front Mol Biosci. 8:860. Doi: 10.3389/fmolb.2021.742903.

Stefani, E., and F. Bezanilla. 1998. Cut-open oocyte voltage-clamp technique. *Methods Enzymol*. 293:300-318. Doi: 10.1016/s0076-6879(98)93020-8.

Tan, H.L., Kupershmidt, S., Zhang, R.,…, and J.R. Balser. 2002. A calcium sensor in the sodium channel modulates cardiac excitability. *Nature*. 415:442-447. Doi: 10.1038/415442a.

Ton, A.T., Nguyen, W., Sweat, K.,…, and N. Abi-Gerges. Arrhythmogenic and antiarrhythmic actions of late sustained sodium current in the adult human heart. *Sci Rep*. 11:12014. Doi: 10.1038/s41598-021-91528-1.

Vandenberg, C.A., and F. Bezanilla. 1991. A sodium channel gating model based on single channel, macroscopic ionic, and gating currents in the squid giant axon. *Biophys J*. 60(6):1511033. Doi: 10.1016/s0006-3495(91)82186-5.

Varga, Z., Zhu, W., Schubert, A.R.,…, and J.R. Silva. 2015. Direct measurement of cardiac Na^+ channel conformations reveals molecular pathologies of inherited mutations. *Circ Arrhythm Electrphysiol*. 8(5):1228-39. Doi: 10.1161/CIRCEP.115.003155.

Wang, C., Hennessey, J.A., Kirkton, R.D.,…, and G.S. Pitt. 2011a. Fibroblast growth factor homologous factor 13 regulates Na^+ channels and conduction velocity in murine hearts. *Circ Res*. 109(7):775-782. Doi: 10.1161/CIRCRESAHA.111.247957.

Wang, C., Wang, C., Hoch, E.G., and G.S. Pitt. 2011b. Identification of novel interaction sites that determine specificity between fibroblast growth factor homologous factors and voltage-gated sodium channels. *J Biol Chem*. 286(27):24253-63. Doi: 10.1074/jbc.M111.245803.

Wang, C., Chung, B.C., Yan, H., Lee, S.Y., and G.S. Pitt. 2012. Crystal structure of the ternary complex of a NaV C-terminal domain, a fibroblast growth factor homologous factor, and calmodulin. *Structure*. 20(7):1167-76. Doi: 10.1016/j.str.2012.05.001.

Wang, X., Tang, H., Wei, E.Q., and C. Wang. 2017. Conditional knockout of Fgf13 in murine hearts increases arrhythmia susceptibility and reveals novel ion channel modulatory roles. *J Mol Cell Cardiol*. 104:63-74. Doi: 10.1016/j.yjmcc.2017.01.009.

West, J.W., Patton, D.E., Scheuer, T., Wang, Y., Goldin, A.L., and W.A. Catterall. 1992. A cluster of hydrophobic amino acid residues required for fast Na(+)-channel inactivation. *Proc Natl Acad Sci USA*. 89(22):10910-4. Doi: 10.1073/pnas.89.22.10910.

White, H.V., Brown, S.T., Bozza, T.C., and I.M. Raman. 2019. Effects of FGF14 and $Na_V\beta4$ deletion on transient and resurgent Na current in cerebellar Purkinje neurons. *J Gen Physiol*. 151(11):1300-18. Doi: 10.1085/jgp.201912390.

Yan, H., Pablo, J.L., Wang, C., and G.S. Pitt. 2014. FGF14 modulates resurgent sodium current in mouse cerebellar Purkinje neurons. *eLife*. 3:e04193. Doi: 10.7554/eLife.04193.

Yang, J., Wang, Z., Sinden, D.S.,…, and C. Wang. 2016. FGF13 modulates the gating properties of the cardiac sodium channel $Na_V1.5$ in an isoform-specific manner. *Channels*. 10(5):410-420. Doi: 10.1080/19336950.2016.1190055.

Zhu, W., Varga, Z., and J.R. Silva. 2016. Molecular motions that shape the cardiac action potential: insights from voltage clamp fluorometry. *Prog Biophys Mol Biol*. 120(1-3):3-17. Doi: 10.1016/j.pbiomolbio.2015.12.003.

Zhu, W., Voelker, T.L., Varga, Z., Schubert, A.R., Nerbonne, J.M, and J.R. Silva. 2017. Mechanisms of noncovalent β subunit regulation of Na_V channel gating. *J Gen Physiol*. 149(8):813-31. Doi: 10.1085/jgp.201711802.

Zhu, W., Mazzani, A., Voelker, T.L.,…, and J.R. Silva. 2019. Predicting patient response to the antiarrhythmic Mexiletine based on genetic variation. Circ Res. 124(4):539-552. Doi: 10.1161/CIRCRESAHA/118.314050.

Zhu, W., Wang, W., Angsutararux, P.,…, J.R. Silva. 2021. Modulation of the effects of class Ib antiarrhythmics on cardiac NaV1.5-encoded channels by accessory NaVβ subunits. JCI Insight. 6(15):e143092. Doi: 10.1172/jci.insight.143092.

2.8 Supplementary Figures

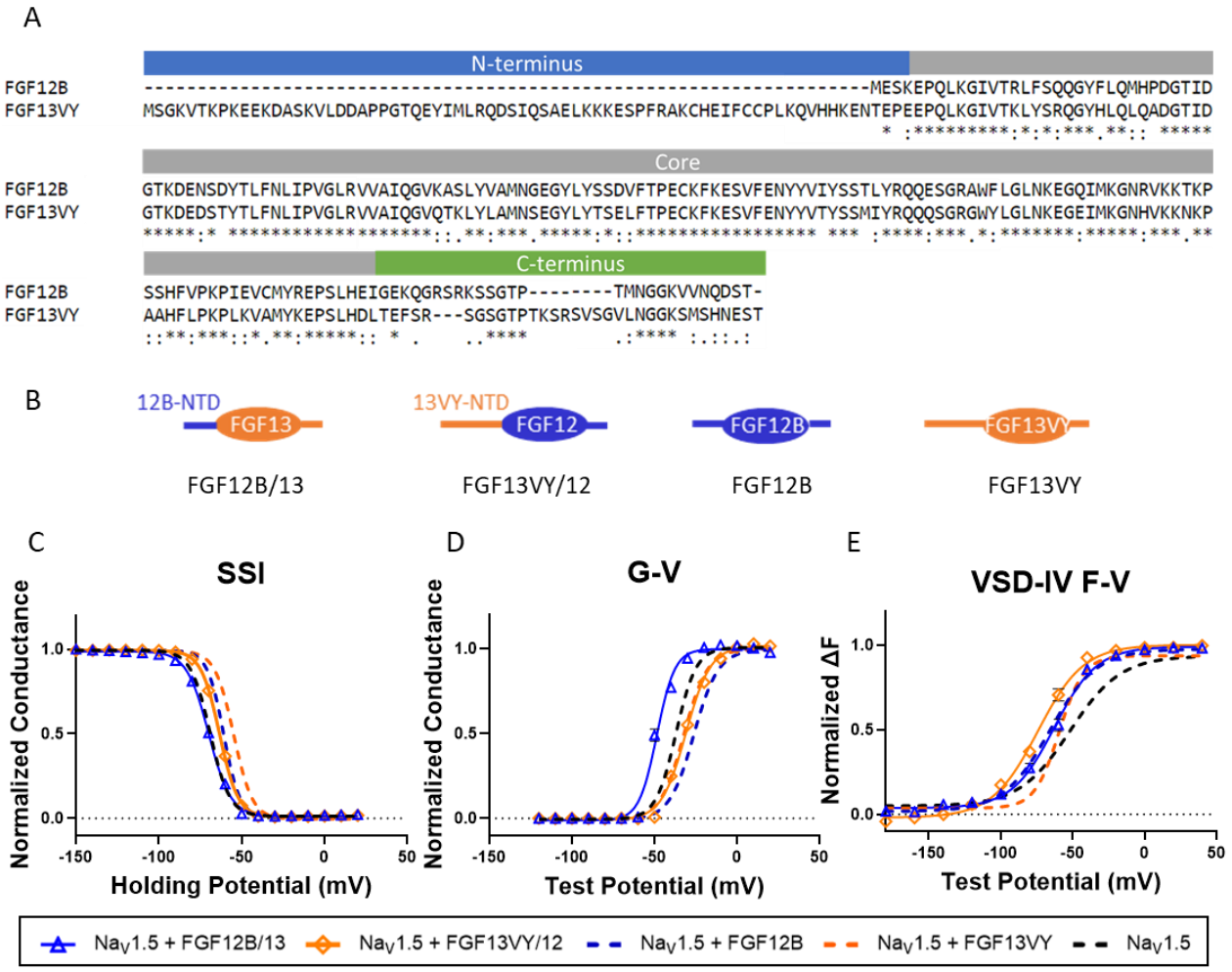

Figure S2.1: Investigation of iFGF N-terminus on the isoform-specific regulation of $Na_V1.5$
(A) An alignment of FGF12B and FGF13VY sequences showed their significant difference in N-terminus. High sequence similarities were found in the iFGF core domain, whereas the C-terminus portrays the difference between the type of iFGF. **(B)** An illustration of iFGF chimeras with swapped N-terminus (FGF12B/13 and FGF13VY/12) and original iFGFs. **(C-E)** The measurements of steady-state inactivation (SSI) **(C)**, voltage-dependence of activation (G-V) **(D)**, and the VSD-IV voltage-dependence of steady-state fluorescence (F-V) curves of $Na_V1.5$ co-expressed with FGF12B/13 (blue triangle, solid line) and FGF13VY/12 (orange diamond, solid line) were compared to $Na_V1.5$ alone (black, dashed line), with FGF12B (blue, dashed line) and with FGF13VY (orange, dashed line) co-expression.

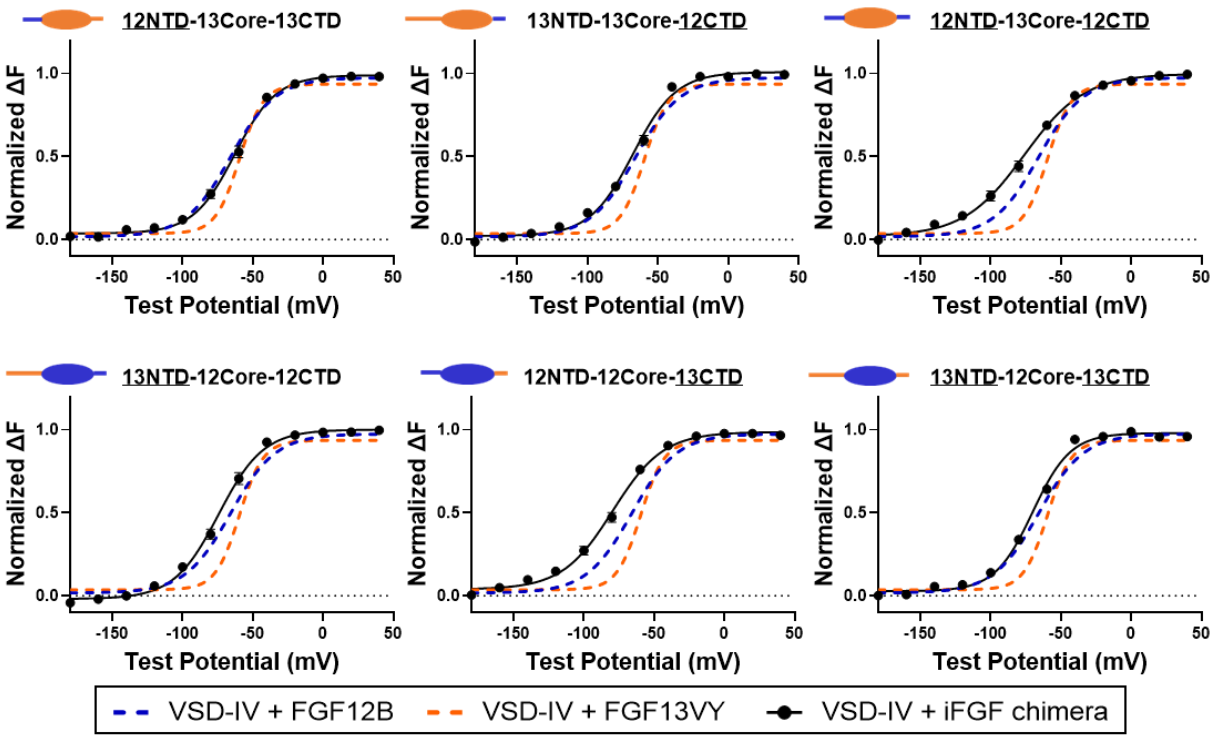

Figure S2.2: The iFGF chimeras experiment reveals the significance of unique iFGF sequence on the modulation of VSD-IV activation

The VSD-IV F-V curves of iFGF chimeras (black, circle) were compared to those of FGF12B (blue, dashed line) and FGF13VY (orange, dashed line), in order to test the significance of different parts of iFGF. Two iFGFs were swapped for N-terminus (left), C-terminus (middle), or both N- and C-termini (right) and tested for their modulation of VSD-IV activation. Results show none of the swapped pairs can sufficiently replicate the results of FGF12B and FGF13VY modulation, indicating the significance of the unique sequence of iFGF stemming from all the iFGF parts.

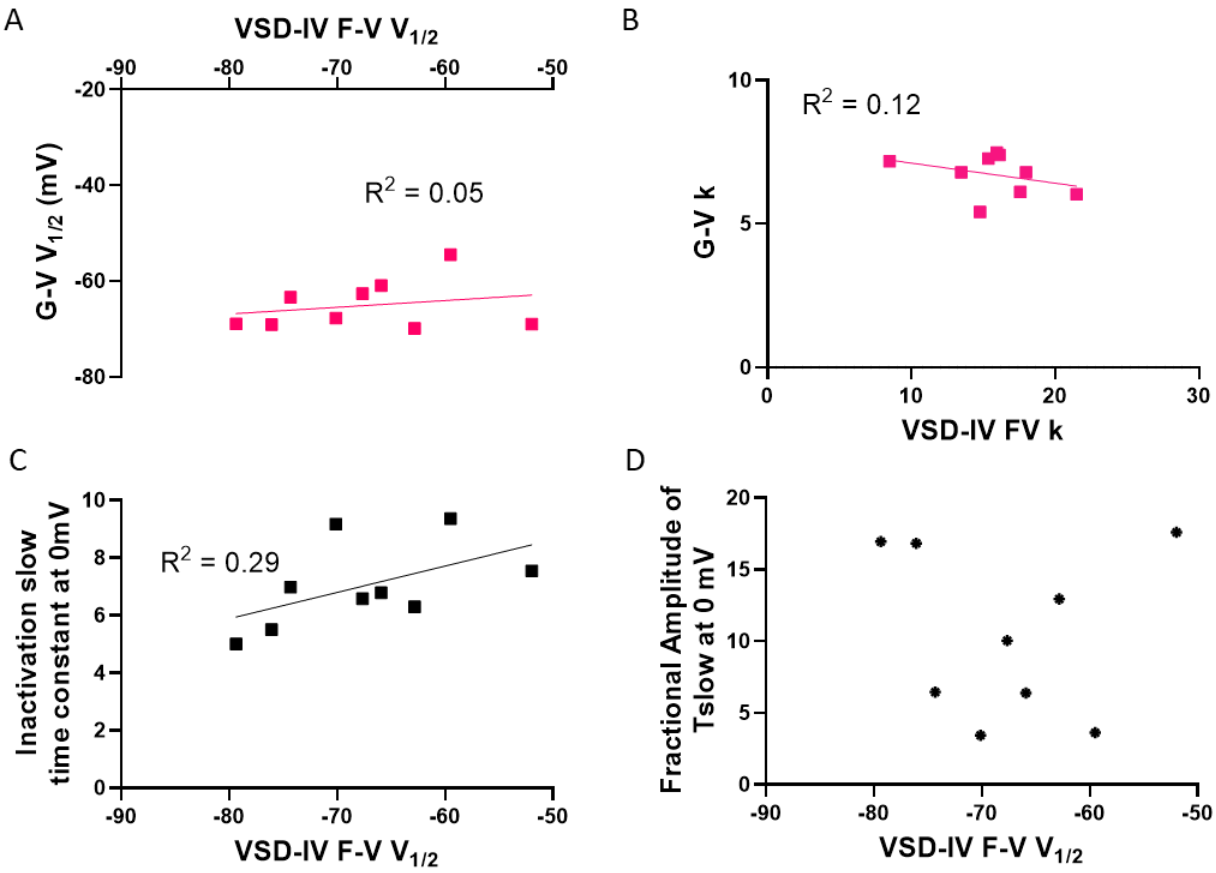

Figure S2.3: Linear regression analyses of iFGFs and iFGF chimeras reveal no relationship between VSD-IV modulation and G-V curves

There is no correlation found between the VSD-IV F-V and the G-V curves, for either $V_{1/2}$ **(A)** or k **(B)**. The $V_{1/2}$ of VSD-IV F-V also does not show correlation to the inactivation kinetics, parameterized as inactivation slow time constant **(C)** and its fractional amplitude **(D)**.

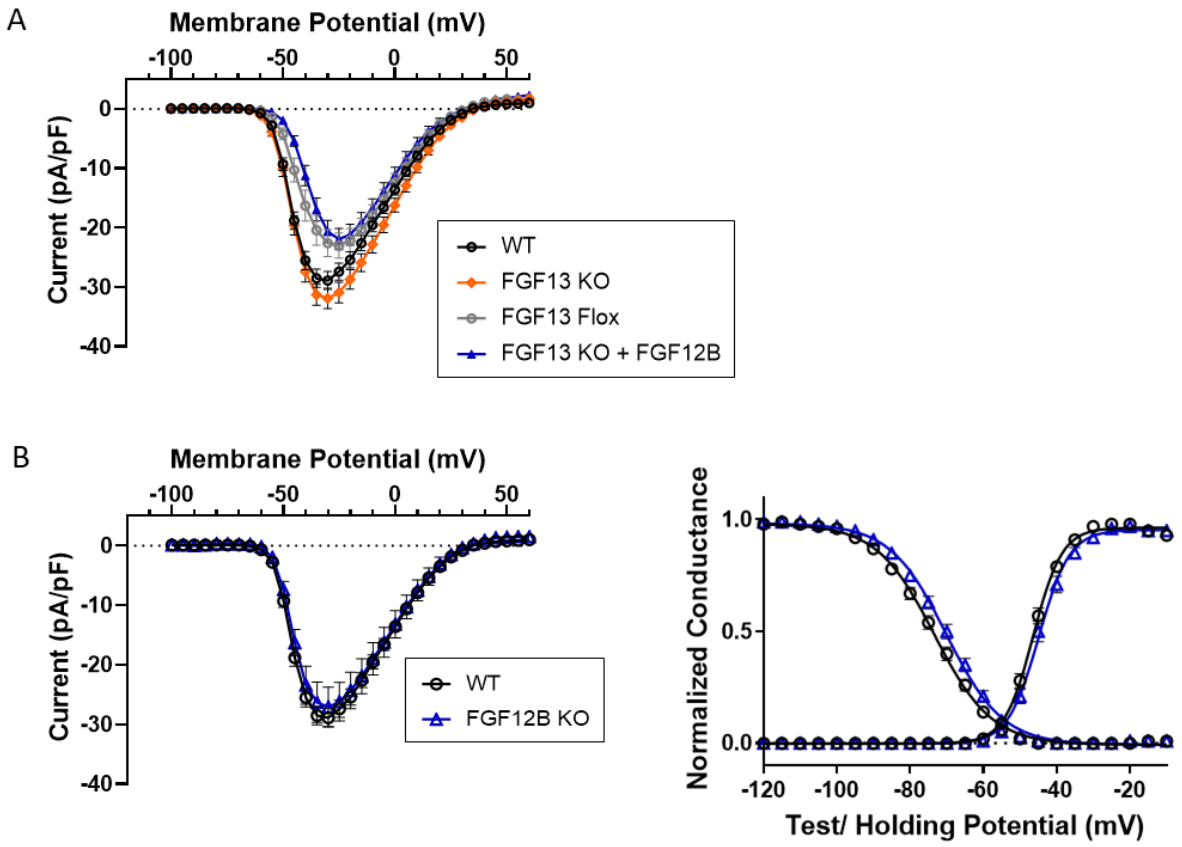

Figure S2.4: The knockout of FGF12B causes no change in I_{Na}, relative to WT mouse ventricular myocytes
(A) The peak current density voltage curves showed no alteration in the peak I_{Na} of FGF13 knockout (orange), and FGF12B expressed in FGF13KO (blue), relative to WT (black) and Flox (grey) mice.
(B) The peak current density voltage curve (left) and voltage dependence of activation and steady-state inactivation curves (right) showed no alteration in FGF12B knockout (blue), relative to WT(black) mice.

Chapter 3: Na_V channel accessory subunit, FGF12A, is the late I_{Na} inhibitor of cardiac $Na_V1.5$

3.1 Abstract

Cardiac voltage-gated sodium ($Na_V1.5$) channels are responsible for the cardiac tissue excitability. Its activation leads to a large inward Na^+ current (I_{Na}), that depolarizes membrane potential during the upstroke of an action potential (AP). Fast inactivation occurs a few milliseconds later and facilitates AP termination. When Na_V channel inactivation is incomplete, residual I_{Na} that persists long after fast inactivation (late I_{Na}) is enhanced, predisposing the heart to arrhythmias. This phenomenon is observed in several acquired diseased conditions including heart failure (HF). Increased late I_{Na} leads to enhanced expression and activation of CaMKII, which can further mediate an increase in late I_{Na}, establishing the positive feedback loop. The specific late I_{Na} inhibitor shows promising therapeutic potential. However, drug therapy targeting late I_{Na} was not yet successful in reversing conditions of HF patients. In this study, we demonstrated the crucial role of FGF12A, which we found upregulated in failing hearts, in the pathophysiology of cardiac diseases. FGF12A is an intracellular fibroblast growth factor (iFGF) and is an important regulator of Na_V channel function. It caused a depolarizing shift in Na_V channel steady-state inactivation (SSI) and a reduction in slower component of Na_V fast inactivation. We illustrated its ability to inhibit late I_{Na} in the inactivation deficient Na_V channels. This switch of iFGF isoforms presents natural protective mechanism. FGF12A expression can modulate the pharmacology and sensitivity of specific late I_{Na} inhibitor like Ranolazine. This work presents the new paradigm of late I_{Na} with adaptive mechanism in pathophysiology of HF.

3.2 Introduction

Cardiac voltage-gated sodium ($Na_V1.5$) channels mediates the excitability of myocytes. The activation of Na_V channels gives rise to inward Na^+ current (I_{Na}) during the upstroke of an action potential (AP) (Yu and Catterall, 2003). Shortly after, Na_V channels inactivate and limit I_{Na}, allowing other outward currents to hyperpolarize membrane potential and terminate an AP. In normal heart, late I_{Na} persisted long-after the fast inactivation is small, relative to peak I_{Na} (Mangold et al., 2017). When the fast inactivation is compromised, elevated level of late I_{Na} could be detrimental and predisposes the heart to arrhythmias (Antzelevitch and Nesterenko, 2015). Enhanced late INa is the common mechanism observed in congenital heart diseases such as long QT type 3 (LQT3) syndrome (Dumaine et al., 1996) and in acquired conditions such as heart failure (HF) (Horvath and Bers, 2014).

When late I_{Na} is increased, the AP duration is prolonged, making the heart susceptible to arrhythmia (Horvath et al., 2013). Additionally, increased intracellular Na^+ can affect intracellular Ca^{2+}, through the sodium calcium exchanger (NCX), and lead to diastolic dysfunction (Sossalla et al., 2011). Increase in Ca^{2+} concentration also enhances the expression and activation of CaMKII, which promotes the positive feedback loop through CaMKII-mediated increase of late I_{Na} (Wagner et al., 2006) (Maltsev et al., 2008) (Aiba et al., 2010) (Ma et al., 2012). An increase in late I_{Na} were found among cardiomyocytes from end-stage HF patients and in HF animal models (Maltsev et al., 2007) (Valdivia et al., 2005) (Maltsev et al., 1998). The treatment of HF with specific late I_{Na} inhibitor such as Ranolazine showed promising therapeutic benefits (Scirica et al., 2007) (Antzelevitch et al., 2011). However, in the clinical trials, Ranolazine failed to reverse the myocardial infarction or severe recurrent ischemia in patients (Morrow et al., 2007). What causes the unsuccessful outcome of this treatment is not well understood.

The primary Na_V α-subunit comprises 4 repeats (I-IV). Each repeat contains 6 membrane segments (S1-S6), with S1-S4 constituting voltage sensing domain (VSD) and S5-S6 forming the Na^+-selective pore. Na_V

channel function is often regulated by auxiliary subunits such as intracellular fibroblast growth factors (iFGFs) or fibroblast growth factor homologous factors (FHFs) (Goldfarb et al., 2007) (Goetz et al., 2009) (Pitt and Lee, 2016) (Yang et al., 2016) (Barbosa et al., 2017) (Effraim et al., 2019). iFGFs are a subfamily of FGFs, sharing high similarities in their sequences (Goldfarb, 2005) (Ornitz and Itoh, 2015). FGF11-FGF14 lack the secretion signal sequences (Munoz-Sanjuan et al., 2000) (Olsen et al., 2003), and are retained intracellularly (Olsen et al., 2003). Each iFGF exists in various isoforms, originating from an alternative splicing in its N-terminus (Munoz-Sanjuan et al., 2000). The expression pattern of iFGFs varies across different tissues (Goldfarb, 2005) (Munoz-Sanjuan et al., 2000) (Wang et al., 2000) (Wang et al., 2011a), and within subcellular compartments (Rush et al., 2006) (Xiao et al., 2013). The interaction between Na_V channel and iFGFs is also isoform specific (Wang et al., 2011b) (Lou et al., 2005) (Liu et al., 2003). The iFGF-mediated modulation of Na_V channel kinetics is distinct between different isoforms (Yang et al., 2016) (Barbosa et al., 2017) (Effraim et al., 2019) (Rush et al., 2006) (Wittmack et al., 2004) (Laezza et al., 2009). We recently illustrated the unique regulatory mechanism of iFGF through $Na_V1.5$ VSD modulation (Angsutararux et al., 2022, in preparation).

In neurons, iFGFs A-isoform regulates the repetitive firing frequency by inducing the long-term inactivation of neuronal Na_V channels (such as $Na_V1.2$, $Na_V1.6$) (Dover et al., 2010) (Yan et al., 2014) (Venkatesan et al., 2014). An inactivation particle was identified on the N-terminus of iFGF A-isoform (Dover et al., 2010) (Yan et al., 2014) (Venkatesan et al., 2014) (Navarro et al., 2020). This inactivation particle is conserved across A-isoform of all iFGFs. In human hearts, FGF12B is the predominant iFGF (Hennessey et al., 2014). *FGF12* gene can encode two isoforms, FGF12A and FGF12B. In this study, we observed an increase in the expression of FGF12A isoform in HF patients. The role and mechanism of FGF12A on cardiac $Na_V1.5$ is not yet established. Here, we demonstrated the significance of FGF12A on the regulation of $Na_V1.5$ function, particularly on its modulation of late I_{Na} in pathogenic conditions. We further investigated its implications on the HF treatment.

3.3 Results

3.3.1 FGF12A expression is upregulated in the human failing heart

In normal human hearts, FGF12B is most highly expressed among iFGF isoforms in both atria and ventricles **(Fig 3.1A)**. There showed some expressions of FGF12A, and less of FGF13s. In the failing ventricles, an increase in the expression of FGF12A and a reduction in FGF12B expression was detected **(Fig 3.1B)**. There was no difference in the expression of FGF13 isoforms in the failing, compared to normal hearts.

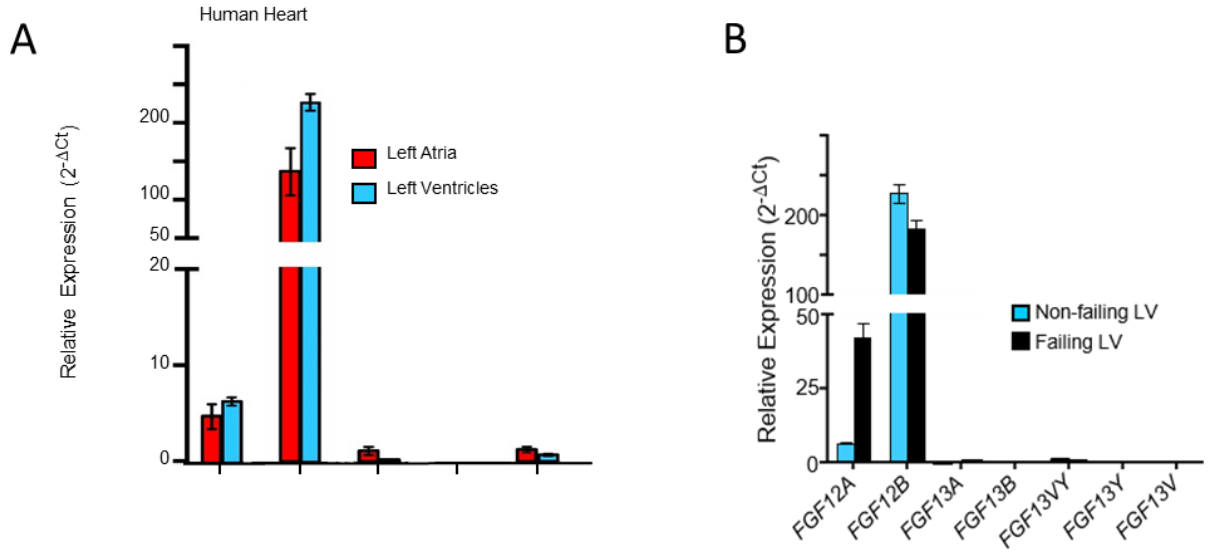

Figure 3.1: The expression of FGF12A is increased in heart failing ventricle
In the normal human heart, the predominant iFGF in both atria and ventricles is FGF12B (left), while FGF12A is also expressed at lower amount. The expression of FGF12A was found to increase in failing ventricles compared to the normal heart, whereas the FGF12B expression is reduced (right).

3.3.2 FGF12A alters $Na_V1.5$ inactivation kinetics

FGF12A was injected with human $Na_V1.5$ at a 4:1 molar ratio to ensure complete interaction for all Na_V channels studied. I_{Na} was measured for $Na_V1.5$ alone or with FGF12A co-expression **(Fig 3.2A)**. The steady-state inactivation (SSI) curve was shifted by FGF12A toward depolarizing potentials, while the voltage

dependence of activation (G-V) curve was not affected **(Table 3.1) (Fig 3.2B)**. The recovery from inactivation also showed no alteration by FGF12A **(Table 3.1) (Fig 3.2C)**. A comparison of I_{Na} traces between $Na_V1.5$ alone and with FGF12A co-expression demonstrated the distinct inactivation kinetics, over the first 10 ms of activation **(Fig 3.2D, insets)**. The normalized peak current decay can be best fitted to a bi-exponential function across membrane potentials. Two inactivation time constants are in the range of a 1s and 10s ms. They are defined as fast and intermediate inactivation, which is faster than the conventional slow inactivation occurring in the range of 100s ms to seconds. We found that FGF12A did not significantly alter the inactivation time constants **(Table 3.1) (Fig 3.2D)**. However, the fractional amplitude of intermediate inactivation relative to the fast inactivation were significantly decreased by FGF12A co-expression across all depolarizing potentials **(Table 3.1) (Fig 3.2E)**. We showed here that FGF12A modulates the Na_V channel inactivation completion at steady state, as well as the fraction of channels undergoing fast vs intermediate inactivation during its fast kinetics.

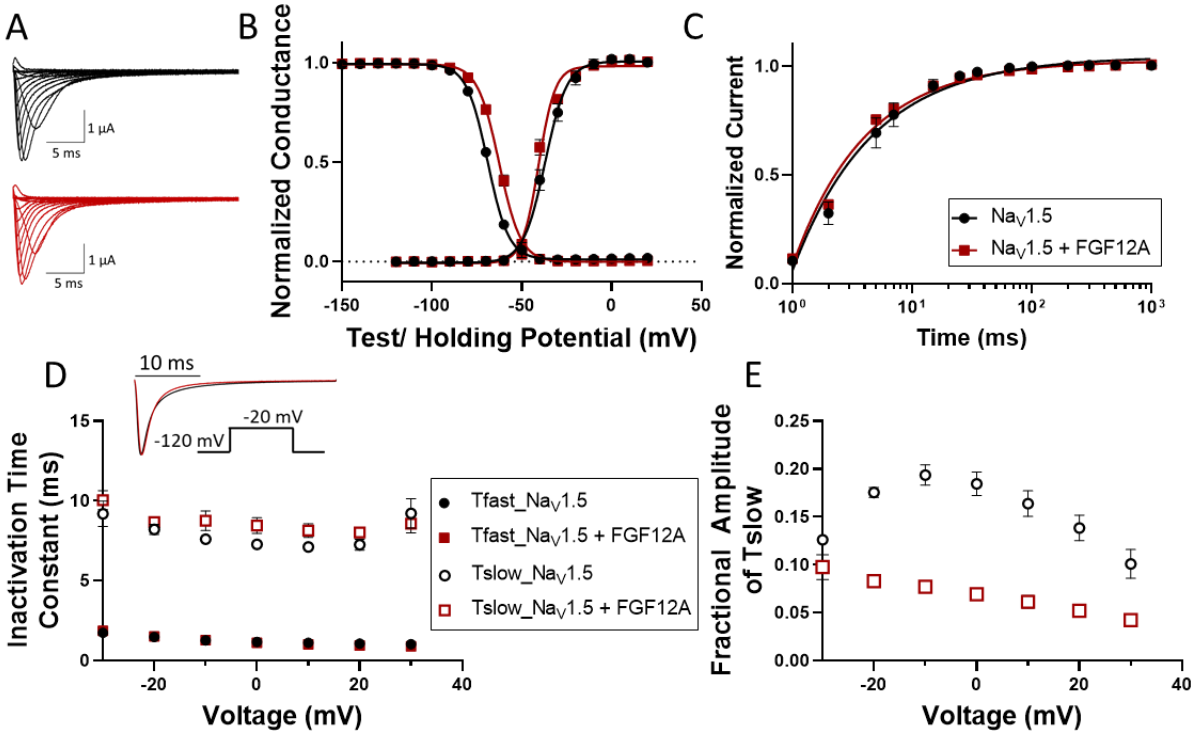

Figure 3.2: The electrophysiological study of FGF12A modulation of human cardiac $Na_V1.5$
(A) The I_{Na} recordings of $hNa_V1.5$ (black) and $hNa_V1.5$ co-expressed with FGF12A (red) in *Xenopus* oocytes were shown. **(B)** The co-expression of FGF12A shifts the steady-state inactivation (SSI) curve towards positive potentials, without affecting the voltage dependence of activation (G-V).

Table 3.1: Fit parameters of $Na_V1.5$ compared to $Na_V1.5$ with FGF12A co-expressions reported as mean ± S.E.M

Parameter		**$Na_V1.5$**	**$Na_V1.5$ + FGF12A**
GV			
	$V_{1/2}$ (n)	-37.0 ± 0.6 (5)	-40.4 ± 0.9 (5)
	p-value		0.6
	k	6.1 ± 0.3	4.5 ± 0.7
	p-value		0.1
SSI			
	$V_{1/2}$ (n)	-69.0 ± 0.5 (9)	-62.6 ± 0.5 (6)
	p-value		<0.001 (***)
	k	5.8 ± 0.3	6.0 ± 0.3
	p-value		0.97
Recovery	**T_f (n)**	2.5 ± 0.2 (8)	2.2 ± 0.1 (6)
	p-value		0.4
	T_s (n)	15.8 ± 1.4	22.4 ± 3.9
Peak decay			
At -30 mV	**T_{fast} (n)**	1.7 ± 0.2 (5)	1.8 ± 0.1 (5)
	T_{slow}	9.2 ± 0.8	10.1 ± 0.6
	A_{slow}	0.13 ± 0.004	0.098 ± 0.01
At -20 mV	**T_{fast}**	1.4 ± 0.2	1.5 ± 0.1
	T_{slow}	8.1 ± 0.4	8.7 ± 0.3
	A_{slow}	0.17 ± 0.006	0.07 ± 0.01 (***)
At -10 mV	**T_{fast}**	1.2 ± 0.1	1.3 ± 0.06
	T_{slow}	7.5 ± 0.3	8.8 ± 0.6
	A_{slow}	0.19 ± 0.01	0.08 ± 0.01 (***)
At 0 mV	**T_{fast}**	1.1 ± 0.1	1.1 ± 0.06
	T_{slow}	7.1 ± 0.3	8.5 ± 0.5 (*)
	A_{slow}	0.18 ± 0.01	0.07 ± 0.006 (***)
At 10 mV	**T_{fast}**	1.1 ± 0.1	1.0 ± 0.05
	T_{slow}	6.9 ± 0.3	8.1 ± 0.4 (*)
	A_{slow}	0.15 ± 0.01	0.06 ± 0.006 (***)
At 20 mV	**T_{fast}**	1.0 ± 0.08	0.95 ± 0.05
	T_{slow}	7.1 ± 0.3	8.0 ± 0.3
	A_{slow}	0.13 ± 0.01	0.05 ± 0.005 (***)
At 30 mV	**T_{fast}**	0.98 ± 0.06	0.8 9 ± 0.04
	T_{slow}	9.3 ± 1.1	8.6 ± 0.6
	A_{slow}	0.09 ± 0.01	0.04 ± 0.006 (**)

Figure 3.2 (Continue): **(C)** The time course of recovery from inactivation is similar between $Na_V1.5$ alone and with FGF12A (T_R $Na_V1.5$: 1.8 ± 0.1 ms, T_R $Na_V1.5$+FGF12A: 1.9 ± 0.1 ms, p-value = 0.4). **(D)** An overlay of normalized I_{Na} at -20 mV shows the accelerated decay for the first 10 ms (inset). The normalized peak current decay was best fitted to a double exponential function across multiple potentials. The fast and slower inactivation time constants are similar between $Na_V1.5$ and $Na_V1.5$ with FGF12A. **(E)** The fractional amplitude of slower inactivation time constants was significantly reduced by FGF12A across depolarizing potentials.

3.3.3 The modulation of FGF12A on VSD-IV activation

We investigated the mechanisms of FGF12A modulation through the voltage-clamp fluorometry (VCF) technique (Rudokas et al., 2014). The fluorescence dye (MTS-TAMRA) was tagged to an individual voltage sensor domain (VSD), allowing its conformational change to be detected. Simultaneous recordings of electrical current I_{Na} and the fluorescence signal gives insights into the kinetics of VSD activation at (Cha & Bezanilla, 1997) (Zhu et al., 2016).

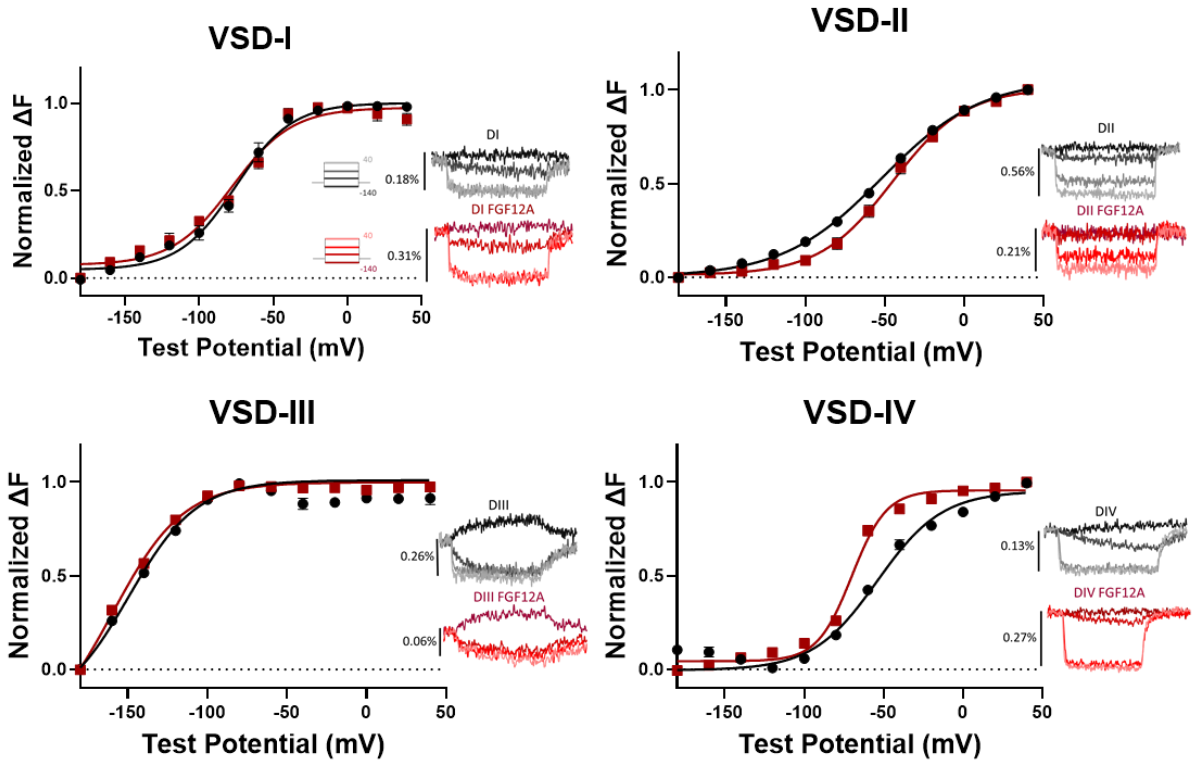

Figure 3.3: FGF12A alter the activation of VSD-IV
The voltage clamp fluorometry (VCF) technique was applied to study the FGF12A effect on individual VSD. The exemplary traces of fluorescence signal at various depolarizing potentials were shown. The change in steady-state emission was normalized and plotted against testing potentials. The voltage dependence of fluorescence emission (F-V) curves showed no difference between $Na_V1.5$ (black) and $Na_V1.5$ with FGF12A co-expression (red) in the activation of VSD-I to VSD-III. However, FGF12A accelerates the completion of VSD-IV activation, shifting the $V_{1/2}$ of the curve toward hyperpolarizing potential as well as decreasing the slope factor k ($Na_V1.5$: $V_{1/2}$ = -54.7 ± 1.4 mV, k = 18.2 ± 1.0, $Na_V1.5$+FGF12A: $V_{1/2}$ = -70.0 ± 1.2 mV, k = 10.6 ± 0.9; p-value $V_{1/2}$ < 0.001, p-value k < 0.001).

The voltage dependence of steady-state fluorescence signal (F-V) curves were examined for each repeat with and without FGF12A co-expression **(Fig 3.3)**. There was no alteration in the F-V curves of VSD-I, II and III **(Table 3.2)** by FGF12A. However, pronounced shift in half maximal voltage ($V_{1/2}$) towards hyperpolarizing potentials was observed for VSD-IV F-V when co-expressed with FGF12A ($Na_V1.5$ $V_{1/2}$: -54.7 ± 1.4 mV, $Na_V1.5$ + FGF12A $V_{1/2}$: -66.2 ± 2.3 mV) **(Table 3.2) (Fig 3.3)**. The slope factor (k) of VSD-IV F-V was also altered ($Na_V1.5$ k: 28.2 ± 1.0, $Na_V1.5$ + FGF12A k: 10.6 ± 0.9) **(Table 3.2)**, indicating an earlier and faster movement of this VSD.

Table 3.2: Fit parameters of voltage dependence of fluorescence (F-V) curves for all voltage sensor domains of NaV1.5 alone, and with FGF12A co-expression

Parameter		**$Na_V1.5$**	**$Na_V1.5$ + FGF12A**
VSD-I FV			
	$V_{1/2}$ (n)	-75.7 ± 3.5 (4)	-78.0 ± 2.6 (4)
	p-value		0.62
	k	18.8 ± 0.9	20.7 ± 2.0
	p-value		0.42
VSD-II FV			
	$V_{1/2}$ (n)	-51.6 ± 1.8 (5)	-48.3 ± 1.7 (3)
	p-value		0.27
	k	33.0 ± 4.9	22.7 ± 1.2
	p-value		0.11
VSD-III FV			
	$V_{1/2}$ (n)	-150.7 ± 1.5 (9)	-157.4 ± 3.1 (6)
	p-value		0.051
	k	21.4 ± 0.8	22.7 ± 1.0
	p-value		0.33
VSD-IV FV			
	$V_{1/2}$ (n)	-54.7 ± 1.4 (6)	-66.2 ± 2.3 (8)
	p-value		<0.001 (***)
	k	28.2 ± 1.0	10.6 ± 0.9
	p-value		<0.001 (***)

3.3.4 FGF12A acts as inactivation particle when Na_V channel inactivation gate is impaired

Na_V channel fast inactivation involves the inactivation gate (IFMT motif) on III-IV linker binding to its receptor, and allosterically blocking the Na^+ conduction (Pan et al., 2018) (Jiang et al., 2020) (Angsutararux et

al., 2021a). To test whether this inactivation gate, is required for FGF12A-mediated modulation of Na_V inactivation, we made an IFM/IQM mutation.

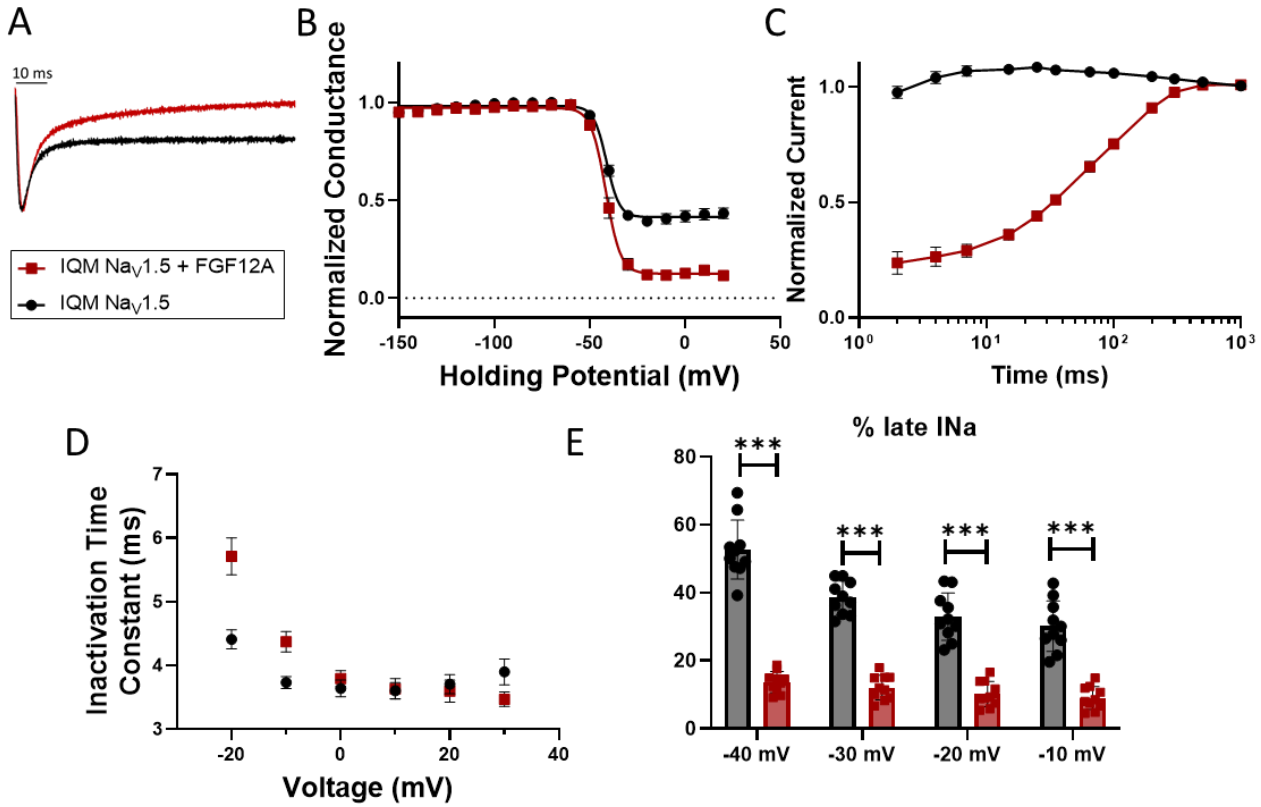

Figure 3.4: FGF12A promotes open-state inactivation in an inactivation-impaired Na$_V$1.5
(A) The mutation of IFMT motif to IQM in Na$_V$1.5 impairs the fast inactivation, leading to the sustained late I_{Na} (black). An expression of FGF12A induces secondary inactivation in IQM Na$_V$1.5, resulting in reduced level of late I_{Na}. **(B)** The SSI curves of IQM Na$_V$1.5 exhibits an incomplete inactivation at depolarizing potentials, while the FGF12A co-expression increases the steady-state inactivation. There is no difference in the $V_{1/2}$ of SSI curves (IQM Na$_V$1.5: -41.6 ± 0.7 mV, IQM Na$_V$1.5+FGF12A: -41.7 ± 0.9 mV, p-value = 0.99). **(C)** The time course of recovery from inactivation for IQM Na$_V$1.5 with FGF12A showed the delayed period with no recovery during the first 10 ms. This hints to the possible different deactivation kinetics of FGF12A from the IFMT motif. **(D)** The peak current decay of IQM Na$_V$1.5 was best fitted to a single exponential equation. The inactivation time constants are similar between the Na$_V$ channels with and without FGF12A. **(E)** The late I_{Na} was measured as the average current during the last 10 ms of the 100-ms depolarizing pulse, normalized to the peak current. There is significant reduction in % late I_{Na} by FGF12A across membrane potentials (filled black circle vs filled red square) (*, **, *** indicate p-values less than 0.05, 0.01, and 0.001 accordingly).

The resulting inactivation impaired IQM Na$_V$1.5 showed noticeable level of late I_{Na}, which is significantly reduced upon FGF12A co-expression **(Fig 3.4A)**. The quantification of late I_{Na} over the last 10 ms of 100-ms depolarization pulse demonstrated FGF12A ability to reduce late I_{Na} across all depolarizing potentials **(Table 3.3) (Fig 3.4E)**. With FGF12A, the inactivation proceeded long after the first few ms toward the entire

duration. The SSI curve also showed a significant reduction in the Na_V channel conductance at depolarizing potentials in the presence of FGF12A, which translates to a higher amount of Na_V channels with complete inactivation **(Fig 3.4B)**. Interestingly, there is no longer the shift in SSI $V_{1/2}$ by FGF12A in IQM $Na_V1.5$ **(Fig 3.4B)**. Removal of the inactivation gate nullified the FGF12A modulation of Na_V SSI, implying its significance in FGF12A regulatory mechanisms.

The recovery from inactivation curve revealed the unique mechanism of FGF12A inactivation particle **(Fig 3.4C)**, featuring the lagging phase where no channel recovers from inactivation. The inactivation kinetic of IQM $Na_V1.5$, as quantified by the peak current decay, was now best fitted to a single exponential function. We observed similar inactivation time constants for IQM $Na_V1.5$ with and without FGF12A, even though the final level of steady-state inactivation was different **(Fig 3.4D)**. The inactivation time constants of FGF12A, however, were distinct from WT $Na_V1.5$ fast and intermediate inactivation. This altogether implies the unique inactivation mechanism of FGF12A inactivation particle.

Past studies identified the N-terminus of iFGF A-isoform (amino acid 2-21) as the inactivation particle for long-term inactivation of neuronal Na_V channels (Dover et al., 2010) (Venkatesan et al., 2014), we tested the specificity of this region in FGF12A and cardiac $Na_V1.5$. The deletion of the inactivation particle sequence made FGF12A ineffective in reducing late I_{Na} of IQM $Na_V1.5$ **(Fig S3.1)**. The A-isoform of FGF13 which contains the same inactivation particle sequence **(Fig S3.2A)** can also reduce late I_{Na} **(Fig S3.2B, C)** and increase steady-state inactivation completion **(Fig S3.2D)**. The recovery from inactivation with FGF13A displayed the lagging phase as observed with FGF12A **(Fig S3.2E)**. Together, these showed the N-terminus of iFGF A-isoform bears the inactivation particle that can rescue cardiac $Na_V1.5$ inactivation when the inactivation gate was impaired.

Table 3.3: Averaged % late I_{Na} for IFM/IQM $Na_V1.5$, alone or with FGF12A measured before and after Ranolazine treatment

Parameter		**Before Ranolazine**	**After Ranolazine**
IQM $Na_V1.5$			
-40 mV	**% late I_{Na} (n)**	52.7 ± 2.7 (10)	39.0 ± 2.4 (7)
	p-value		0.003 (**)
	% block		25.2 ± 4.0
-30 mV	**% late I_{Na} (n)**	38.4 ± 1.6 (10)	27.0 ± 1.8 (7)
	p-value		< 0.001 (***)
	% block		27.0 ± 3.9
-20 mV	**% late I_{Na} (n)**	32.9 ± 2.2 (10)	21.3 ± 1.7 (7)
	p-value		0.001 (**)
	% block		29.5 ± 3.8
-10 mV	**% late I_{Na} (n)**	30.1 ± 2.3 (10)	16.4 ± 0.9 (7)
	p-value		< 0.001 (***)
	% block		36.1 ± 3.6
IQM $Na_V1.5$+ FGF12A			
-40 mV	**% late I_{Na} (n)**	13.7 ± 1.0 (10)	11.7 ± 1.1 (7)
	p-value		0.2
	% block		23.2 ± 8.1
-30 mV	**% late I_{Na} (n)**	12.1 ± 1.2 (10)	9.2 ± 0.5 (7)
	p-value		0.06
	% block		34.5 ± 5.9
-20 mV	**% late I_{Na} (n)**	10.2 ± 1.2 (10)	7.2 ± 0.5 (7)
	p-value		0.06
	% block		39.4 ± 6.7
-10 mV	**% late I_{Na} (n)**	9.0 ± 1.1 (10)	5.8 ± 0.7 (7)
	p-value		0.04 (*)
	% block		49.7 ± 7.1

3.3.5 FGF12A reduces late I_{Na} in LQT3-linked $Na_V1.5$ variants on III-IV linker

An inherited cardiac disease long-QT type 3 (LQT3) syndrome is caused by mutations in $Na_V1.5$ that enhances late I_{Na}, leading to the prolonged QT interval. A treatment with late I_{Na} blocker serves as an effective therapy (Nagatomo et al., 2000). Here, we tested whether FGF12A can reduce late I_{Na} in LQT3-linked $Na_V1.5$ variants. These variants are usually found along locations, involved in the regulation of Na_V channel inactivation, such as III-IV linker (Kapplinger et al., 2015). We studied three variants, F1473S, ΔK1500, and ΔKPQ (Zhu et al., 2019) **(Fig 3.5A).** The current recording at -20 mV showed noticeable level of late I_{Na} for these 3 variants **(Fig 3.5D)**. The SSI curves also showed non-zero conductance at high depolarizing potential, an implication of incomplete inactivation **(Fig 3.5E)**. The expression of FGF12A with these LQT3-linked variants led to the significant reduction in late I_{Na}, with great efficiency over 50% **(Table 3.4) (Fig 3.5B)**. The steady-state availability also decreased with FGF12A co-expression, in addition to its depolarizing shift in $V_{1/2}$ **(Table 3.5) (Fig 3.5C, D)**. Indeed, two variants, ΔK1500 and ΔKPQ, showed almost complete inactivation in the presence of FGF12A. We demonstrated here the potential of FGF12A as a late I_{Na} inhibitor for LQT3 treatment.

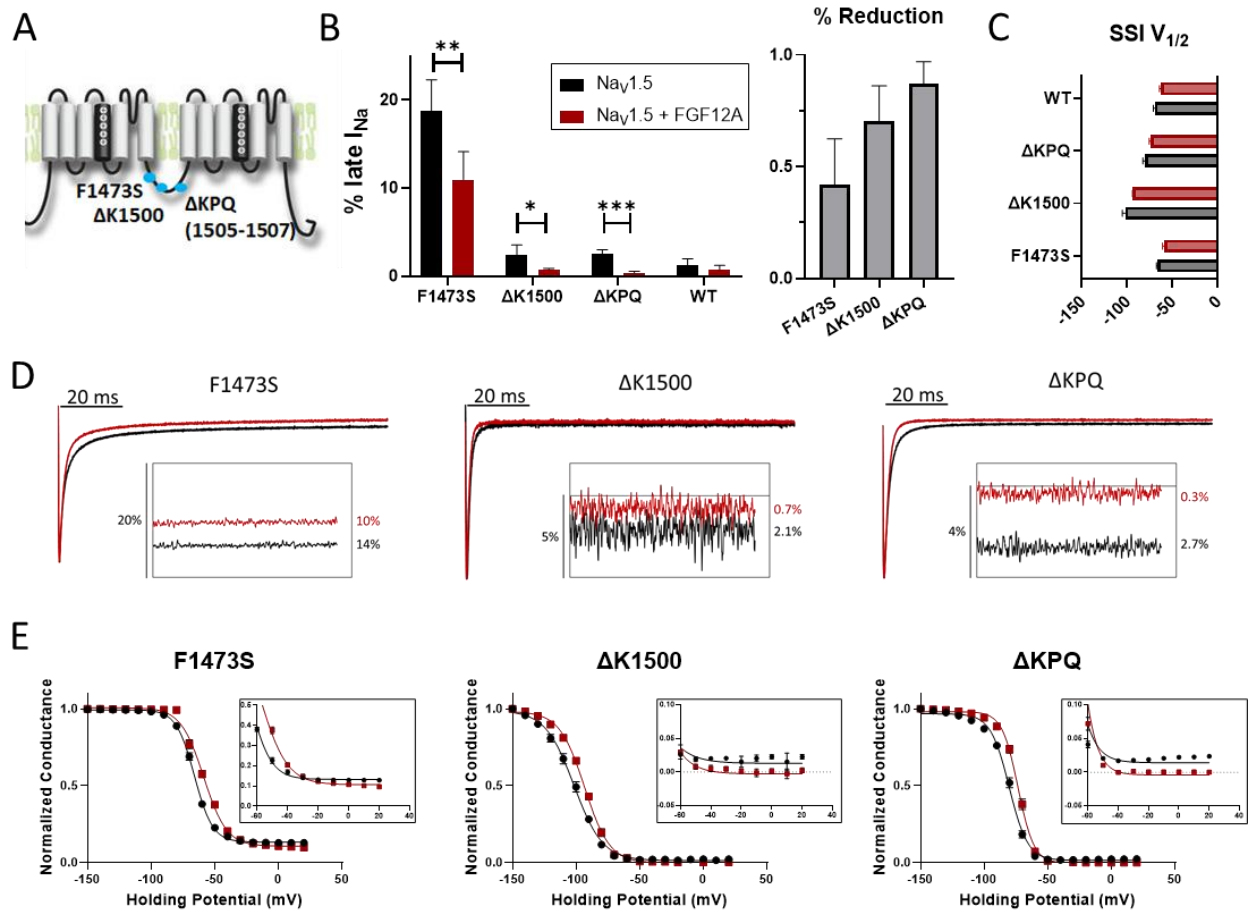

Figure 3.5: FGF12A acts as a late I_{Na} inhibitor in LQT3-linked $Na_V1.5$ variants
(A) An illustrated figure shows mutations in III-IV linker, that are found in patients with long QT type 3 (LQT3) syndrome. **(B)** All LQT3-linked Na_V variants exhibited the late I_{Na} that was significantly reduced by FGF12A. **(C)** The comparison of SSI $V_{1/2}$ between LQT3-linked $Na_V1.5$ variants alone (grey) and with FGF12A (red). **(D)** Exemplary traces of LQT3-linked I_{Na}, compared between in the absence and presence of FGF12A (black vs red). Insets showed the level of late I_{Na} during the last 10 ms. **(E)** The incomplete steady-state inactivation was decreased by the co-expression of FGF12A (inset), reducing the channel conductance at depolarizing potentials almost to zero. The SSI curves were also shifted by FGF12A towards positive potentials.

Table 3.4: % late INa of LQT3-linked NaV1.5 variants, alone or with FGF12A co-expression

Variants		**$Na_V1.5$**	**$Na_V1.5$ + FGF12A**
F1473S	**% late I_{Na} (n)**	18.7 ± 1.6 (5)	10.9 ± 1.1 (8)
	p-value		0.002 (**)
ΔK1500	**% late I_{Na} (n)**	2.4 ± 0.6 (4)	0.7 ± 0.1 (4)
	p-value		0.025 (*)
ΔKPQ	**% late I_{Na} (n)**	2.5 ± 0.2 (5)	0.3 ± 0.1 (5)
	p-value		< 0.001 (***)
D1790G	**% late I_{Na} (n)**	0.9 ± 0.1 (5)	0.4 ± 0.1 (7)
	p-value		0.01 (*)
Y1795C	**% late I_{Na} (n)**	4.5 ± 1.3 (4)	0.7 ± 0.5 (4)
	p-value		0.03 (*)
E1901Q	**% late I_{Na} (n)**	1.0 ± 0.6 (10)	0.4 ± 0.1 (6)
	p-value		< 0.001 (***)
S1904L	**% late I_{Na} (n)**	2.6 ± 0.6 (5)	1.0 ± 0.2 (5)
	p-value		0.03 (*)
Q1909R	**% late I_{Na} (n)**	0.8 ± 0.1 (4)	0.7 ± 0.2 (4)
	p-value		0.73
IQ/AA	**% late I_{Na} (n)**	0.7 ± 0.1 (4)	0.7 ± 0.2 (4)
	p-value		0.89
WT	**% late I_{Na} (n)**	1.2 ± 0.4 (5)	0.7 ± 0.2 (5)
	p-value		0.27

Table 3.5: Fit parameters of SSI curves for all LQT3-linked $Na_V1.5$ variants alone, and with FGF12A co-expression

Variants		**$Na_V1.5$**	**$Na_V1.5$ + FGF12A**
F1473S	**SSI $V_{1/2}$ (n)**	-66.0 ± 1.2 (4)	-58.7 ± 1.7 (4)
	p-value		< 0.001 (***)
	SSI k	7.2 ± 0.5	8.7 ± 0.2
ΔK1500	**SSI $V_{1/2}$ (n)**	-80.2 ± 1.9 (4)	-93.2 ± 0.5 (3)
	p-value		0.006 (**)
	SSI k	11.3 ± 0.6	9.9 ± 0.6
ΔKPQ	**SSI $V_{1/2}$ (n)**	-69.0 ± 1.6 (4)	-73.3 ± 1.8 (4)
	p-value		0.002 (**)
	SSI k	7.3 ± 0.2	6.2 ± 0.2
D1790G	**SSI $V_{1/2}$ (n)**	-83.9 ± 1.4 (4)	-71.4 ± 1.2 (6)
	p-value		< 0.001 (***)
	SSI k	5.6 ± 0.1	4.6 ± 0.1
Y1795C	**SSI $V_{1/2}$ (n)**	-77.9 ± 4.9 (4)	-57.3 ± 1.3 (4)
	p-value		< 0.001 (***)
	SSI k	5.6 ± 0.2	5.5 ± 0.5
E1901Q	**SSI $V_{1/2}$ (n)**	-66.6 ± 3.0 (8)	-49.8 ± 1.0 (4)
	p-value		< 0.001 (***)
	SSI k	5.3 ± 0.1	4.0 ± 0.2
S1904L	**SSI $V_{1/2}$ (n)**	-69.1 ± 0.3 (5)	-54.5 ± 2.0 (5)
	p-value		< 0.001 (***)
	SSI k	5.2 ± 0.3	5.3 ± 0.3
Q1909R	**SSI $V_{1/2}$ (n)**	-75.0 ± 1.0 (4)	-62.3 ± 0.9 (5)
	p-value		< 0.001 (***)
	SSI k	6.7 ± 0.2	5.6 ± 0.4
IQ/AA	**SSI $V_{1/2}$ (n)**	-78.5 ± 2.2 (7)	-59.8 ± 1.8 (5)
	p-value		< 0.001 (***)
	SSI k	6.5 ± 0.2	7.3 ± 0.2

3.3.6 FGF12A induces a large shift in SSI $V_{1/2}$ when $Na_V1.5$ variants disrupt CaM binding on the CTD

Next, we tested the LQT3-linked variants registered to the C-terminal domain (CTD) of $Na_V1.5$, which contains the binding sites of iFGF and Calmodulin (CaM) (Wang et al., 2012). We picked 5 LQT3-linked variants, D1790G (Liu et al., 2003) (Abriel et al., 2000), Y1795C (Vecchietti et al., 2007) (Rivolta et al., 2001), E1901Q (Kapplinger et al., 2009), S1904L (Bankston et al., 2007), and Q1909R (Tester et al., 2005) **(Fig 3.6A)**. Three variants, E1901Q, S1904L, and Q1909R are located within the CaM-binding motif (IQ motif) (Yan et al., 2017), whereas D1790G and Y1795C are in the globular or the EF-hand domain. These two amino acids D1790 and Y1795 are shown in the interaction interface between two $Na_V1.5$ CTDs (Gabelli et al., 2014). The EF-hand domain was also proposed to interact with III-IV linker during inactivation (Gardill et al., 2018). Except D1790G (Liu et al., 2003), the rest of these LQT3-linked variants were reported to display enhanced late I_{Na} as arrhythmogenic mechanism.

In our *Xenopus* oocytes heterologous system, however, only Y1795C and S1904L showed substantially larger late I_{Na}, than WT $Na_V1.5$ **(Table 3.4) (Fig 3.6B)**. Even the IQ/AA $Na_V1.5$, that abolishes the binding site of CaM, showed non-significant late I_{Na}. Still, FGF12A was effective in reducing late I_{Na} for Y1795C and S1904L **(Table 3.4) (Fig 3.6D)**, showing approximately the same % reduction efficiency as in LQT3-linked variants in III-IV linker **(Fig 3.6B)**. Interestingly, the expression of FGF12A with Y1795C NaV1.5 delayed its fast inactivation, as observed by distinctively slowed peak current decay **(Fig 3.6D)**. The SSI curves of all LQT3-linked variants in the CTD were shifted towards depolarizing potentials by FGF12A **(Table 3.5)**, with the inactivation mostly complete at steady state **(Fig 3.6C, E)**. The shifts in SSI $V_{1/2}$ by FGF12A, nevertheless, were larger among $Na_V1.5$ variants on the CTD, relative to WT and LQT3-linked variants on III-IV linker **(Fig S3)**. The magnitude of the change was largest in IQ/AA $Na_V1.5$. The difference here suggests the significance of CaM binding towards FGF12A regulation of $Na_V1.5$.

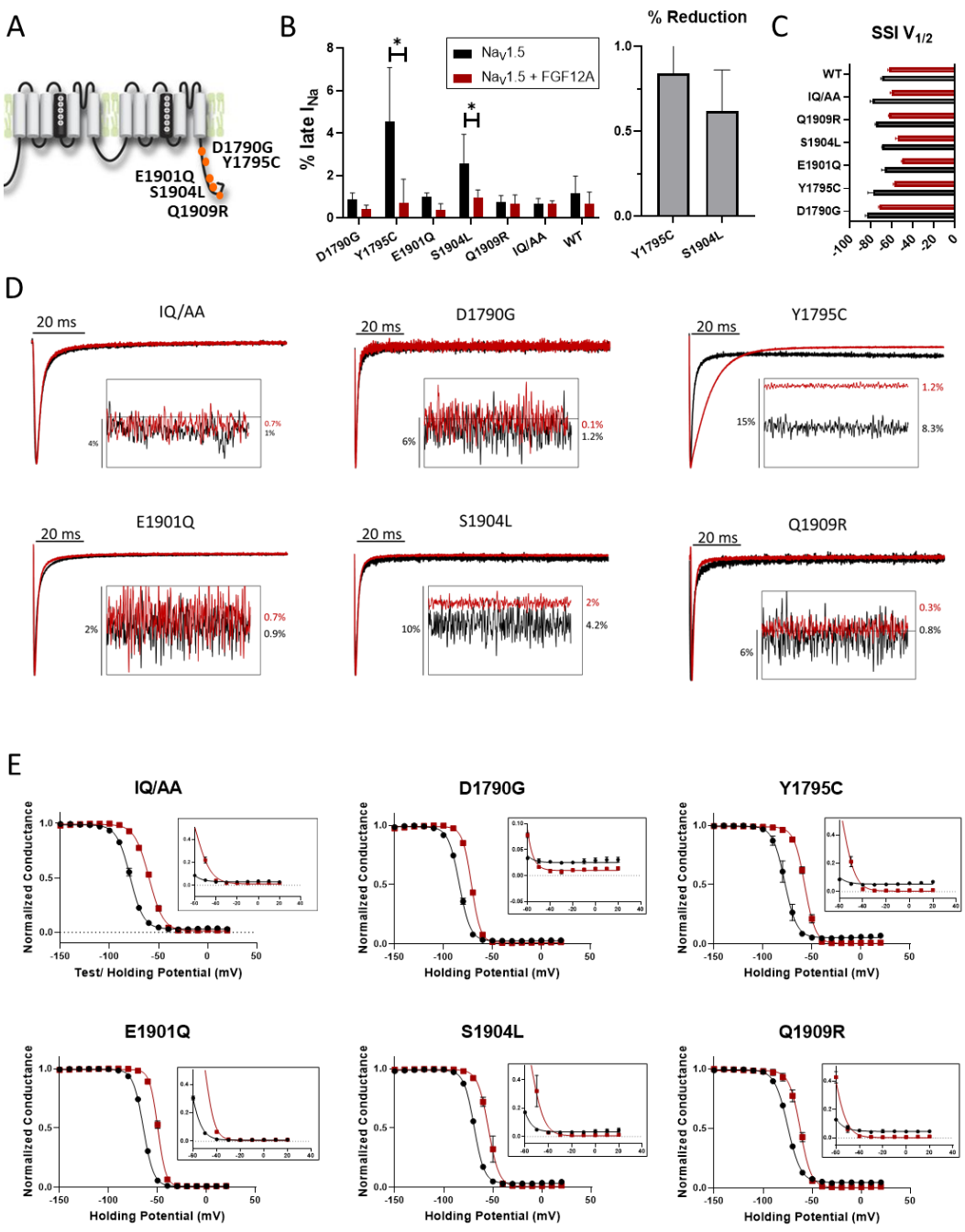

Figure 3.6: Effects of FGF12A on LQT3-linked $Na_V1.5$ variants located at the C-terminal domain
(A) An illustrated figure shows mutations in the C-terminal domain (CTD) that are found in patients with long QT type 3 (LQT3) syndrome **(B)** FGF12A reduced late I_{Na} in 2 $Na_V1.5$ variants, Y1795C and S1904L. The rest of the LQT3-linked $Na_V1.5$ variants did not show significant increase in late I_{Na}, relative to WT $Na_V1.5$. **(C)** The comparison of SSI $V_{1/2}$ between LQT3-linked $Na_V1.5$ variants alone (grey) and with FGF12A (red). **(D)** The exemplary I_{Na} traces of LQT3-linked $Na_V1.5$ variants (black) alone and with FGF12A co-expression (red). Insets show the late I_{Na} during the last 10 ms of the depolarizing pulse. **(E)** SSI curves demonstrated the FGF12A-modulated shifts towards depolarizing potentials for all LQT3-linked variants on $Na_V1.5$ CTD, as well as the more complete inactivation (insets).

3.3.7 FGF12A modulates late I_{Na} blocker, Ranolazine

We demonstrated the ability of FGF12A to reduce late I_{Na} in the inactivation-impaired Na_V channels. We then wanted to test how FGF12A affects the efficacy of the specific late I_{Na} blocker like Ranolazine. Studies showed that accessory proteins such as B-subunit can modulate the sensitivity of the NaV channels to antiarrhythmic drug (Zhu et al., 2021). We found that in IFM/IQM $Na_V1.5$, Ranolazine caused the significant reduction in % late I_{Na} **(Table 3.3) (Fig 3.7A, B)**. However, when FGF12A was co-expressed, % late I_{Na} before and after Ranolazine treatment were no longer significantly different **(Table 3.3) (Fig 3.7A, B)**. FGF12A was more potent in blocking late I_{Na} than Ranolazine in in IQM $Na_V1.5$, yielding smaller % late I_{Na}. Still, the efficacy of Ranolazine in inhibiting late I_{Na} was not affected by the presence of FGF12A **(Fig 3.7C)**. Rather, FGF12A greatly reduced late I_{Na} in such a way that further reduction by Ranolazine appeared insignificant. The modulatory effect of FGF12A, instead, altered Ranolazine block of I_{Na} peak current **(Fig 3.7A, D)**. Significantly larger reduction in peak I_{Na} by Ranolazine was observed with FGF12A co-expression, as comparison to IQM $Na_V1.5$ **(Fig 3.7D)**. In the presence of FGF12A, Ranolazine was more effective in inhibiting peak, rather than late I_{Na} in IQM $Na_V1.5$, especially at less depolarized potentials. This modification of peak I_{Na} inhibition by FGF12A, however, was not observed in WT $Na_V1.5$ **(Fig S3.4A)**. Ranolazine yielded similar tonic block (TB) and use-dependent block (UDB) in WT $Na_V1.5$, regardless of the expression of FGF12A **(Fig S3.4B)**.

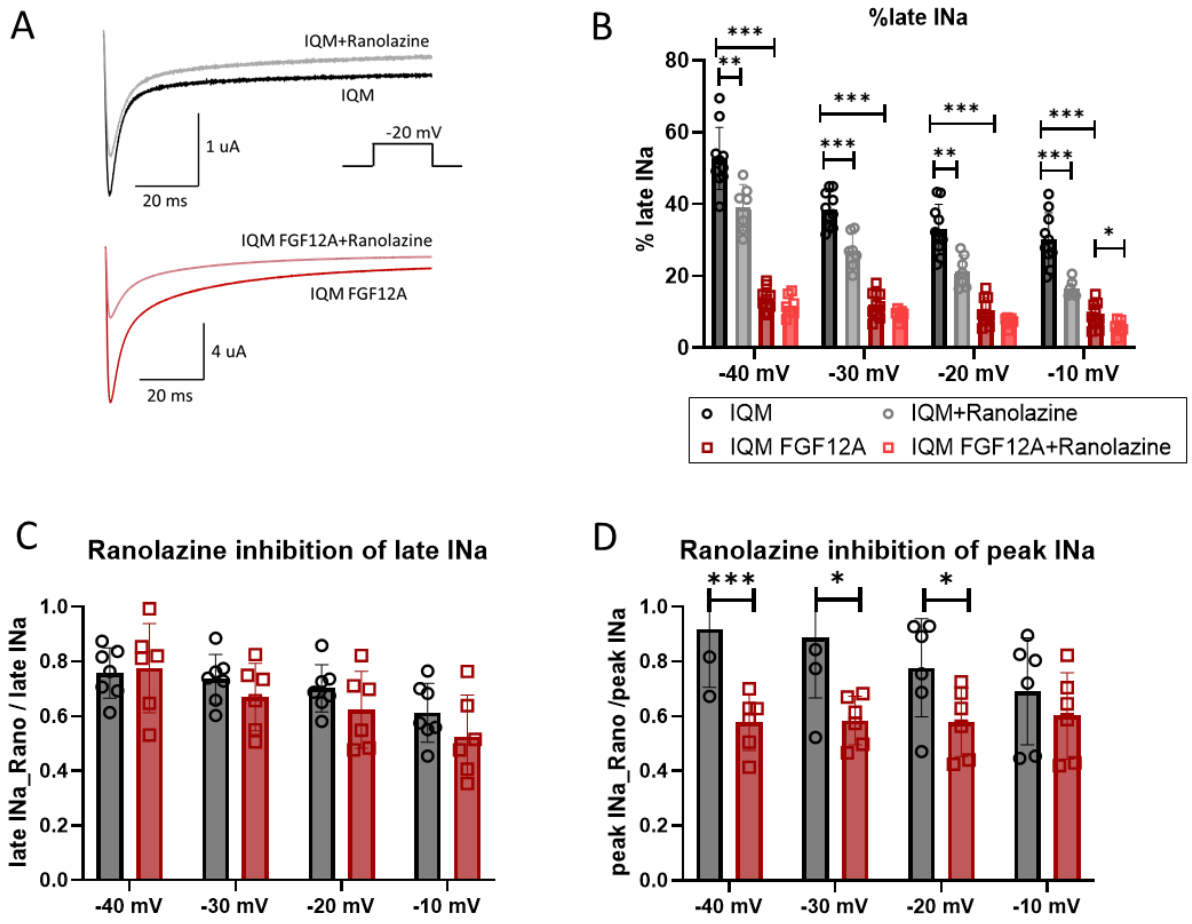

Figure 3.7: FGF12A expression modulates the pharmacology of specific late I_{Na} inhibitor Ranolazine
(A) Exemplary traces of IQM (top) and IQM with FGF12A (bottom) before and after Ranolazine. The drug induces the reduction in both peak and late I_{Na}. **(B)** The % late I_{Na}, relative to peak I_{Na}, of IQM $Na_V1.5$ was significantly reduced by Ranolazine and FGF12A at all potentials. However, Ranolazine failed to cause significant reduction in % late I_{Na} when IQM $Na_V1.5$ was co-expressed with FGF12A. **(C)** The % inhibition of late I_{Na} by Ranolazine was similar in IQM $Na_V1.5$ with and without FGF12A. **(D)** FGF12A increased Ranolazine inhibition of peak I_{Na}.

3.4 Discussion

When the heart fails to pump blood efficiently, multiple adaptations are triggered as compensatory mechanisms (Kemp and Conte, 2012) (Jackson et al., 2000). Some mechanisms such as cardiac remodeling may lead to eventual deterioration of cardiac function, while some are believed to have protective effects

(Mann, and Bristow, 2005). These alterations can also happen at the cellular level in cardiac myocytes (Dash et al., 2001).

In cardiomyocytes isolated from left ventricle of heart failure (HF) patients, we observed an increase in the expression of FGF12A and a reduction of FGF12B. This alteration hints to the possible novel adaptative mechanisms upon HF. In this study, we demonstrated the therapeutic potential of FGF12A in pathophysiology of heart diseases, and how its expression might affect the treatment by specific late I_{Na} inhibitor like Ranolazine.

3.4.1 FGF12A modulates Na_V channel inactivation through VSD-IV regulation

A co-expression of FGF12A increased $Na_V1.5$ steady-state availability without affecting the voltage-dependence of its activation. FGF12A did not alter the recovery from inactivation but modulated the fast inactivation kinetics, by biasing the channels undergoing open-state inactivation towards fast inactivation across all depolarizing potentials. In our recent work, we compared the mechanisms of regulations between two iFGF isoforms, FGF12B and FGF13VY, that are dominant in human and mouse hearts accordingly and found similar regulatory effects on Na_V channel inactivation (Angsutararux et al., submitted). The depolarizing shifts in SSI were also reported in other studies of different Na_V and iFGF isoforms (Liu et al., 2003) (Yang et al., 2016) (Wang et al., 2011a) (Wang et al., 2012) (Effraim et al., 2019). We identified the same FGF12A regulation of VSD-IV activation, as in our previous work on FGF12B and FGF13VY (Angsutararux et al., submitted). The regulation of VSD-IV and VSD-III kinetics was previously shown to affect $Na_V1.5$ inactivation (Hsu et al., 2017).

The effect of FGF12A on SSI also relied on an inactivation gate (IFMT motif), as shown in IFM/IQM $Na_V1.5$. When an inactivation gate is impaired, the FGF12A-mediated shift in SSI was no longer detected. In general, iFGFs show similar regulation mechanism on $Na_V1.5$, by modulating the activation of VSD-IV to mediate inactivation kinetics and through the interaction with III-IV linker, to affect steady-state inactivation.

3.4.2 FGF12A is a late I_{Na} inhibitor

The expression of FGF12A in IQM $Na_V1.5$ significantly reduced late I_{Na}. This phenomenon has not been observed prior with FGF12B nor FGF13VY. We thus speculate the potential of FGF12A as a late I_{Na} inhibitor in inactivation impaired Na_V channels. Indeed, the N-terminus of FGF12A (amino acid 2-21) likely contains an inactivation particle as suggested by other studies (Dover et al., 2010) (Venkatesan et al., 2014). The distinct kinetics of recovery from inactivation and inactivation time constant of FGF12A expressed with IQM $Na_V1.5$ suggests the unique mechanism of FGF12A inactivation particle that is different from IFMT motif.

We showed that FGF12A can reduce the percentage of late I_{Na} in LQT3-linked Na_V variants. The LQT3 syndrome is caused by mutations in $Na_V1.5$ that disrupt Na_V channel inactivation leading to sustained late I_{Na} (Wang et al., 1996). The resulting prolonged QT duration predisposes patients to fatal arrhythmias. FGF12A was an effective late I_{Na} inhibitor for most LQT3-linked variants on III-IV linker and the CTD we studied. There were, however, differences in the level of late I_{Na} observed between *Xenopus* oocytes expression system and HEK cells from past studies, for two variants E1901Q and Q1909R. The lack of late I_{Na} in *Xenopus* oocytes might be due to the high CaM expression (Yan et al., 2017) or the elevated Ca2+ concentration (Abdelsayed et al., 2017) that rescue defective CaM binding.

The cryo-EM structure of cockroach Na_VPaS channel included the CTD interaction with III-IV linker via equivalent residue pair E1784-K1493 in $Na_V1.5$ (Shen et al., 2017). The interaction sites were also tested in another study using isothermal titration calorimetry (ITC) and NMR spectroscopy (Gardill et al., 2018). They were mapped to III-IV linker K1504/K1505 and the EF-hand domain in the CTD. Here, we observed the higher FGF12A blocking efficiency in LQT3-linked variants closer to these identified sites (ΔK1500, ΔKPQ, Y1795C vs F1473S, S1904L), hinting at the significance of III-IV linker and the CTD interaction on FGF12A inactivation particle function.

We also found accelerated inactivation kinetics upon FGF12A co-expression for most LQT3-linked variants,

except Y1795C. A significantly slower inactivation kinetic, over early depolarization (20 ms), occurred in Y1795C $Na_V1.5$ when FGF12A was expressed. Yet, sustained late I_{Na} during prolonged depolarization (100 ms) was significantly reduced. This Y1795 is an interesting residue. Multiple mutations can register to various phenotypically distinct conditions. Three variants, Y1795C, Y1795H and Y1795insD result in LQT3, Brugada and mixed phenotype syndromes accordingly (Vecchietti et al., 2007) (Rivolta et al., 2001). A study demonstrated that Y1795C disrupted the heterodimer interaction between the CTD of one $Na_V1.5$ and CaM bound to the CTD of the other $Na_V1.5$ (Gabelli et al., 2014) (Yan et al., 2017). The mutation might affect iFGF binding conformation and a coupling between Na_V channel dimers.

Additionally, FGF12A caused the depolarizing shifts in SSI for all LQT3-linked variants. There were, however, differences in the magnitude of $V_{1/2}$ alteration. For LQT3-linked variants in III-IV linker, FGF12A induced the similar change in SSI $V_{1/2}$ as in WT $Na_V1.5$. When variants occurred in the CTD, that affect CaM binding affinities, FGF12A caused the larger depolarizing shifts in SSI $V_{1/2}$, almost twice as much as in WT $Na_V1.5$. This difference suggests an important, but non-essential role of CaM in FGF12A regulation of $Na_V1.5$. Recent study demonstrated that iFGF N-terminal domain also contains CaM binding site, further down an inactivation particle region (Mahling et al., 2021). It is possible that CaM, with reduced affinities in LQT3-linked variants, preferentially binds to the FGF12A N-terminus and affect the Na_V channel availability. CaM binding on its N-terminus might alter FGF12A conformation on the $Na_V1.5$ CTD, and its regulation of SSI. A model was proposed based on a chimeric structure of $Na_V1.7$-Na_VPaS with α-scorpion toxin that at resting state, the Na_V CTD interacts with VSD-IV, resulting in sequestered III-IV linker. Upon VSD-IV activation, III-IV linker is released to move the IFMT motif to its binding site (Clairfeuille et al., 2019). The binding of CaM and iFGF on the CTD could cooperatively modulate such interactions (Gade et al., 2020) (Abrams et al., 2020) (Kang et al., 2021).

3.4.3 FGF12A modifies the pharmacology of late I_{Na} inhibitor, Ranolazine

Ranolazine is the specific late I_{Na} inhibitor (Rayner-Hartley & Sedlak, 2016) that shows potential clinical

benefits in patients with LQT3 (Scirica et al., 2007) (Moss et al., 2008) (Chorin et al., 2016). It is recommended in the guideline by the American College of Cardiology Foundation and the American Heart Association for patients with stable ischemic heart disease that are unable to use acceptable dose of β-blockers. In clinical trials of patients with stable angina, Ranolazine treatment improved exercise performance and reduced exercise-induced myocardial ischemia (Chaitman et al., 2004) (Thadani, 2004). Ranolazine, however, failed to diminish major cardiovascular end point of death, myocardial infarction, or severe recurrent ischemia in patients with non-ST-elevation acute coronary syndromes (ACS) (Morrow et al., 2007). Possibly, the increased expression of FGF12A we found in HF patients might attenuate Ranolazine efficacy. We showed here that the expression of FGF12A can alter the pharmacology of Ranolazine.

Since FGF12A is also the late I_{Na} inhibitor, with an even greater efficiency than Ranolazine, its expression rendered Ranolazine less beneficial, even though it did not change Ranolazine's ability to inhibit late I_{Na}. FGF12A, however, altered the Ranolazine profile on peak current inhibition. Ranolazine conferred greater blocking efficiency towards peak than late current, in the presence of FGF12A for IQM $Na_V1.5$, but not WT $Na_V1.5$. The binding of FGF12A inactivation particle could possibly alter the Ranolazine binding affinity. The binding of FGF12A inactivation particle might be in the similar region as Ranolazine binding site, around the common local anesthetic (LA) drug binding site F1760 (Abrams et al., 2020) (Fredj et al., 2009). Since FGF12A only participated in Na_V channel inactivation when the IFMT motif was compromised, we did not observe the FGF12A modulation of Ranolazine in WT $Na_V1.5$. Another possibility is that FGF12A modulate Ranolazine effect through VSD regulation, as previously shown for Mexilitine (Zhu et al., 2019), and Lidocaine and Ranolazine modulation by β-subunits (Zhu et al., 2021).

3.4.4 Significance of FGF12A in pathophysiology of cardiac diseases

FGF12A demonstrated its high blocking efficiency towards late I_{Na}, suggesting its potential protective roles in HF patients. Even though we reported here an increase in expression of FGF12A in HF patients that should be beneficial, the amount of FGF12A might not be high enough to revert late I_{Na}, or the time of this alteration

happens too late during the stage where it is no longer beneficial. The reduction of late I_{Na} during early stage of HF could provide more benefits for the prevention of HF progression. It remains to be tested whether this FGF12A inactivation particle works in Na_V channel modified by CaMKII, the likely cause of increased late I_{Na} in HF (Maltsev et al., 2007) (Horvath & Bers, 2014). iFGF was also reported to regulate cardiac calcium channel $Ca_V1.2$ (Hennessey et al., 2013). The regulation of iFGF, especially the balance of iFGF isoforms, thus represents the novel therapeutic target for cardiac arrhythmias.

3.4.5 Limitations

Our specific study of $Na_V1.5$ and FGF12A co-expression omits the complicated environment of native cardiomyocytes. A multimolecular complex of Na_V channels is formed by myriad of regulatory subunits. These auxiliary subunits such as β-subunits also modulate $Na_V1.5$ through VSD regulation (Zhu et al., 2017) (Angsutararux et al., 2021). A thorough investigation of multiple subunits combined should be addressed in the future. The difference in an expression system, *Xenous* oocytes vs HEK cells, can also contribute to the disparities reported between different studies, especially when the intracellular CaM and Ca^{2+} concentrations are of significant roles. In this study, we haven't observed the FGF12A effect on a long-term inactivation of $Na_V1.5$, as reported in previous studies (Dover et al., 2010). The discrepancy could be pertaining to the study system, and careful consideration is needed to realize the full potential of FGF12A in antiarrhythmic treatment.

3.5 Conclusion

We have shown the mechanism of FGF12A modulation of $Na_V1.5$ inactivation kinetics and steady state inactivation is through the regulation of VSD-IV kinetics. We presented the novel role of FGF12A as the late I_{Na} inhibitor in pathophysiology of cardiac diseases. FGF12A can effectively reduce late I_{Na} in congenital LQT3-linked $Na_V1.5$ variants, while increasing the channel availability. These combined effects of FGF12A

can be beneficial towards the treatment of cardiac arrhythmias. We proved the potential protective roles of increased FGF12A expression in HF patients and put forward its therapeutic values for the early treatment of HF.

3.6 Materials and Methods

3.6.1 Molecular biology

Plasmid constructs were made for human FGF12A (UniProtKB identifier: **P61328-1**) and human $Na_V1.5$ (UniprotKB identifier: **Q14524-1**) on pBSTA and pMAX vectors, respectively. The constructs for voltage-clamp fluorometry (VCF) studies were made in the background of C373Y and Y1977A mutations, to ensure maximal fluorescence signal expression (Varga et al., 2015). Then, a cysteine mutation was engineered into each voltage sensor domain (VSD): V215C for VSD-I, S805C for VSD-II, M1296C for VSD-III and S1618C for VSD-IV in separate constructs. Our lab has previously shown these mutations yield the optimal sensitivity without significantly altering $Na_V1.5$ gating kinetics (Varga et al., 2015).

All LQT3-linked variants in this study were made using primers with overlap extension and high-fidelity polymerase chain reaction (PCR). The plasmids were purified with Midiprep (MACHEREY-NAGEL) and sequenced to confirm a successful mutagenesis. Then, the capped mRNA was made with mMESSAGE mMACHINE T7 transcription kit (Thermo Fisher Scientific).

3.6.2 *Xenopus* oocyte cut-open recording and voltage-clamp fluorometry

Oocytes were obtained from *Xenopus laevis* by laparotomy according to the protocol #21-0371 (approved by the Washington University Institutional Animal Care and Use Committee). Oocytes were harvested and injected with mRNAs for the total of 40-80 ng per cell. FGF12A was co-injected with $Na_V1.5$ at a 4:1 molar ratio. Oocytes were incubated at 18°C for 3-5 days in ND93 solution (93 mM NaCl, 5 mM KCl, 1.8 mM

$CaCl_2$, 1 mM $MgCl_2$, 5 mM HEPES, 2.5 mM Na-pyruvate, and 1% penicillin-streptomycin, pH7.4). Cut-open oocyte recordings were performed with a CA-1B amplifier (Dagan Corporation) and Clampex software (v10; Molecular Devices). The oocyte chamber was temperature controlled to 19°C with an HCC-100A temperature controller (Dagan Corporation). The external recording solution consists of 25 mM NMG-Mes, 90 mM Na-Mes, 20 mM HEPES, and 2 mM Ca-Mes_2, with pH adjusted to 7.4. The internal recording solution contains 105 mM NMG-Mes, 10 mM Na-Mes, 20 mM HEPES, and 2 mM EGTA, adjusted to pH 7.4. Ranolazine dihydrochloride (SelleckChem) was dissolved in the external recording solution at a concentration of 4 mmol/L, and was perfused manually in the oocyte chamber.

For the VCF protocol (Rudokas et al., 2014), oocytes were labeled with 10 µM methanethiosulfonate-carboxytetramethylrhodamine (MTS-TAMRA; Santa Cruz Biotechnology) in a depolarizing solution (110 mM KCl, 1.5 mM $MgCl_2$, 0.8 mM $CaCl_2$, 0.2 mM EDTA, and 10 mM HEPES, pH 7.1) for 30 minutes on ice in the dark. A teal LED light at 510/25 nM wavelength (SPECTRA X, Lumencor) was used to excite the fluorophore and the emission light was measured with a photodiode PIN-040A (United Detector Technology) and an Axopatch-200A amplifier (Molecular Devices). The fluorescence traces were collected simultaneously with the ionic current over the activation protocol and averaged over 10 runs.

3.6.3 Electrophysiology data analysis

For each recording, the membrane capacitance was compensated and the P/-8 leak subtraction was performed. The data were analyzed with Clampfit software (v10; Molecular Devices) and Excel (Microsoft). The voltage-dependence of activation and steady-state inactivation curves were fitted to a Boltzmann equation

$$G(V) = (1+\exp(V_{1/2}-V)/k)^{-1}$$

where G(V) is the conductance normalized between 0 and 1, V is the test voltage (mV), $V_{1/2}$ is the half-maximal voltage, and k is the slope factor.

The recovery from inactivation is fitted to a double exponential function

$$G(V) = C - A_1 \cdot \exp(-t/T_1) - A_2 \cdot \exp(-t/T_2)$$

where t is the recovery duration (s), C is the constant, A_1 and A_2 are the fractional amplitudes, and T_1 and T_2 are the recovery time constants.

The normalized peak current decay was fitted to a bi-exponential function

$$I(t) = A_{slow} \cdot \exp(-t/T_{slow}) + A_{fast} \cdot \exp(-t/T_{fast})$$

Where t is the decay time (s), A_{slow} and A_{fast} are the fractional amplitudes, and τ_{slow} and τ_{fast} are inactivation time constants.

The % late current was calculated as the average current during the last 10 ms of the 100-ms depolarizing pulse, normalized to the peak current.

The fluorescence data was low pass filtered at 1 kHz before baseline subtracting to correct for photobleaching. At -120 mV, which is the resting potentials before and after activation pulses, the fluorescence trace was fitted to a 4-term exponential function and served as the baseline with no change in fluorescence. The change in fluorescence signal relative to the baseline fluorescence (ΔF) was then calculated for each membrane potential. The voltage-dependence of Fluorescence signal (F-V) curve was fitted to the Boltzmann equation.

3.6.4 Statistical analysis

Statistical analysis was performed via Prism9 software (GraphPad). The data was collected from the sample size of 3-10. The statistical significance between 2 groups was tested by an unpaired student t-test. The significant difference was determined by the p-value of less than 0.05 (*), 0.01 (**) and 0.001 (***).

3.7 References

Abdelsayed, M., Baruteau, A.E., Gibbs, K., Sanatani, S., Krahn, A.D., Probst, V., and Ruben, P.C. 2017. Differential calcium sensitivity in NaV1.5 mixed syndrome mutants. *J Physio*. 595(18):6165-6186.

Abrams, J., Roybal, D., Chakouri, N., Katchman, A.N.,…, and Marx, S.O. 2020. Fibroblast growth factor homologous factors tune arrhythmogenic late NaV1.5 current in calmodulin binding-deficient channels. *JCI Insight*. 5(19):e141736.

Abriel, H., Wehrens, X.H.T., Benhorin, J., Kerem, B., and Kass, R.S. 2000. Molecular pharmacology of the sodium channel mutation D1790G linked to the long-QT syndrome. *Circulation*. 102(8):921-925.

Aiba, T., Hesketh, G.G., Liu, T., Carlisle, R., Villa-Abrille, M.C., O'Rourke, B., Akar, F.G., and Tomaselli, G.F. 2010. Na+ channel regulation by Ca2+/calmodulin and Ca2+/calmodulin-dependent protein kinase II in guinea-pig ventricular myocytes. Cardiovasc Res. 85:454-463.

Antzelevitch, C., Burashnikov, A., Sicouri, S., and Belardinelli, L. 2011. Electrophysiological basis for the antiarrhythmic actions of ranolazine. *Heart Rhythm*. 8:1281-1290.

Antzelevitch, C., and Nesterenko, V. 2015. The role of late INa in development of cardiac arrhythmias. *Handb Exp Pharmacol*. 221:137-168.

Angsutararux, P., Kang, P.W., Zhu, W., and Silva, J.R. 2021a. Conformations of voltage-sensing domain III differentially define NaV channel closed- and open-state inactivation. *J Gen Physiol*. 153(9):e202112891.

Angsutararux, P., Zhu, W., Voelker, T., and Silva, J.R. 2021. Molecular pathology of sodium channel beta subunit variants. *Front Pharmacol*. 12:761275.

Bankston, J.R., Sampson, K.J., Kateriya, S., Glaaser, I.W., Malito, D.L., Chung, W.K., and Kass, R.S. 2007. A novel LQT-3 mutation disrupts an inactivation gate complex with distinct rate-dependent phenotypic consequences. *Channels*. 1(4):273-280.

Barbosa, C., Xiao, Y., Johnson, A.J., Xie, W., Strong, J.A., Zhang, J.M., and Cummins, T.R. 2017. FHF2 isoforms differentially regulate NaV1.6-mediated resurgent sodium currents in dorsal root ganglion neurons. *Pfugers Arch*. 469(3):195-212.

Cha, A., and Bezanilla, F. 1997. Characterizing voltage-dependent conformational changes in the Shaker K+ channel with fluorescence. *Neuron*. 19:1127-1140.

Chaitman, B.R., Skettino, S.L., and Parker, J.O. 2004. MARISA Investigators. Anti-ischemic effects and long term survival during ranolazine monotherapy in patients with chronic severe angina. *J Am Coll Cardiol*. 43:1375-1382.

Chorin, E., Hu, D., Antzelevitch, C., Hochstadt, A.,…, and Viskin, S. 2016. Ranolazine for congenital long-QT syndrome type III : experimental and long-term clinical data. *Circ Arrhythm Electrophysiol*. 9(10):e004370.

Clairfeuille, T., Cloake, A., Infield, D.T., Llongueras, J.P.,…, and Payandeh, J. 2019. Structural basis of α-scorpion toxin action on NaV channels. *Science*. 363(6433):eaav8573.

Dash, R., Kadambi, V., Schmidt, A., Tepe, N.M.,…, and Kranias, E.G. 2001. Interactions between phospholamban and β-adrenergic drive may lead to cardiomyopathy and early motality. *Circulation*. 103:889-896.

Dover, K., Solinas, S., D'Angelo, E., and Goldfarb, M. 2010. Long-term inactivation particle for voltage-gated sodium channels. *J Physiol*. 19:3695-3711.

Dumaine, R., Wang, Q., Keating, M.T., Hartmann, H.A., Schwartz, P.J., Brown, A.M., and Kirsch, G.E. 1996. Multiple mechanisms of Na+ channel-linked long-QT syndrome. *Circ Res*. 78:916-924.

Effraim, P.R., Huang, J., Lampert, A., Stamboulian, S., Zhao, P., Black, J.A., Dib-Haji, S.D., and Waxman, S.G. 2019. Fibroblast growth factor homologous factor 2 (FGF-13) associates with NaV1.7 in DRG neurons and alters its current properties in an isoform-dependent manner. *Neurobiol Pain*. 6:100029.

Fredj, S., Sampson, K.J., Liu, H., and Kass, R.S. 2009. Molecular basis of ranolazine block of LQT3-mutant sodium channels: evidence for site of action. *Br J Pharmacol*. 148(1):16-24.

Gabelli, S.B., Boto, A., Kuhns, V.H., Bianchet, M.A.,…, and Amzel. M.L. 2014. Regulation of the NaV1.5 cytoplasmic domain by calmodulin. *Nat Commun*. 5:5126.

Gade, A.R., Marx, S.O., and Pitt, G.S. 2020. An interaction between the III-IV linker and CTD in NaV1.5 confers regulation of inactivation by CaM and FHF. *J Gen Physiol*. 152(2):e201912434.

Gardill, B.R., Rivera-Acevedo, R.E., Tung, C.C., Okon, M., McIntosh, L.P., and Petegem, F.V. 2018. The voltage-gated sodium channel EF-hands form an interaction with the III-IV linker that is disturbed by disease-causing mutations. *Sci Rep*. 8:4483.

Goetz, R., Dover, K., Laezza, F., Shtraizent, N.,…, and Mohammadi, M. 2009. Crystal structure of a fibroblast growth factor homologous factor (FHF) defines a conserved surface on FHFs for binding and modulation of voltage-gated sodium channels. *J Biol Chem*. 284(26):17883-17896.

Goldfarb, M. 2005. Fibroblast growth factor homologous factors: evolution, structure, and function. *Cytokine Growth Factor Rev*. 16(2):215-220.

Goldfarb, M., Schoorlemmer, J., Williams, A., Diwakar, S.,…, and D'Angelo, E. 2007. Fibroblast growth factor homologous factors control neuronal excitability through modulation of voltage-gated sodium channels. *Neuron*. 55(3):449-463.

Hennessey, J.A., Wei, E., and Pitt, G. 2013. Fibroblast growth factor homologous factors modulate cardiac calcium channel. *Circ Res*. 223(4):381-388.

Hennessey, J.A., Marcou, C.A., Wang, C., Wei, E.Q.,…, and Pitt, G.S. 2014. FGF12 is a candidate Brugada syndrome locus. *Heart Rhythm*. 10(12):10.1016/j.hrthm.2013.09.064.

Horvath, B., Banyasz, T., Jian, Z., Hegyi, B., Kistamas, K., Nanasi, P.P., Izu, L.T., and Izu, Y.C. 2013. Dynamics of the late Na(+) current during cardiac action potential and its contribution to afterdepolarizations. *J Mol Cell Cardiol*. 64:59-68.

Horvath, B., and Bers, D.M. 2014. The late sodium current in heart failure: pathophysiology and clinical relevance. ESC Heart Fail. 1(1):26-40.

Hsu, E.J., Zhu, W., Schubert, A.R., Voelker, T., Varga, Z., and Silva, J.R. 2017. Regulation of Na+ channel inactivation by the DIII and DIV voltage-sensing domains. *J Gen Physiol*. 149(3):389-403.

Huang, B., El-Sherif, T., Gidh-Jain, M., Qin, D., El-Sherif, N. 2001. Alterations of sodium channel kinetics and gene expression in the postinfarction remodeled myocardium. *J Cardiovasc Electrophysiol*. 12:218-225.

Jackson, G., Gibbs, C.R., Davies, M.K., and Lip, G.Y.H. 2000. Pathophysiology. *ABC of heart failure*. 320(7228):167-170.

Jiang, D., Shi, H., Tonggu, L., Gamal El-Din, T.M.,…, and Catterall, W.A. 2020. Structure of the cardiac sodium channel. Cell. 180(1):122-134.

Kang, P.W., Chakouri, N., Diaz, J., Tomaselli, G.F., Yue, D.T., and Ben-Johny, M. 2021. Elementary mechanisms of calmodulin regulation of $Na_V1.5$ producing divergent arrhythmogenic phenotypes. *Proc Natl Acad Sci*. 118(21):e2025085118.

Kapplinger, J.D., Tester, D.J., Salisbury, B.A., Carr, J.L., Harris-Kerr, C., Pollevick, G.D., Wilde, A.A., and Ackerman, M.J. 2009. Spectrum and prevalence of mutations from the first 2,500 consecutive unrelated patients referred for the FAMILION long QT syndrome genetic test. *Heart Rhythm*. 6:1297-1303.

Kapplinger, J.D., Giudicessi, J.R., Ye, D., Tester, D.J., Callis, T.E., Valdivia, C.R., Maakielski, J.C., Wilde, A.A., and Ackerman, M.J. 2015. Enhanced classification of Brugada syndrome-associated and long-QT syndrome-associated genetic variants in the SCN5A-encoded Na(V)1.5 cardiac sodium channel. *Circ Cardiovasc Genet*. 8(4):582-595.

Kemp, C.D., and Conte, J.V. 2012. The pathophysiology of heart failure. *Cardiovascular Pathology*. 21(5):365-371.

Laezza, F., Lampert, A., Kozel, M.A., Gerber, B.R.,…, and Ornitz, D.M. 2009. FGF14 N-terminal splice variants differentially modulate NaV1.2 and NaV1.6-encoded sodium channels. *Mol Cell Neurosci*. 42(2):90-101.

Liu, C.J., Dib-Haji, S.D., Renganathan, M., Cummins, T.R., and Waxman, S.G. 2003. Modulation of the cardiac sodium channel NaV1.5 by fibroblast growth factor homologous factor 1B. *J Biol Chem*. 278(2):1029-1036.

Lou, J.Y., Laezza, F., Gerber, B.R., Xiao, M.,…, and Ornitz, D.M. 2005. Fibroblast growth factor 14 is an intracellular modulator of voltage-gated sodium channels. *J Physiol*. 569(1):179-193.

Ma, J., Luo, A., Wu, L., Wan, W., Zhang, P., Ren, Z., Zhang, S., Qian, C., Shyrock, J.C., and Belardinelli, L. 2012. Calmodulin kinase II and protein kinase C mediate the effect of increased intracellular calcium to augment late sodium current in rabbit ventricular myocytes. *Am J Physiol Cell Physiol*. 302:C1141-1151.

Mahling, R., Rahlf, C.R., Hansen, S.C., Hayden, M.R., and Shea, M.A. 2021. Ca^{2+}-saturated calmodulin binds tightly to the N-terminal domain of A-type fibroblast growth factor homologous factors. *J Biol Chem*. 296: 100458.

Maltsev, V.A., Sabbah, H.N., Higgins, R.S., Silverman, N., Lesch, M., and Undrovinas, A.I. 1998. Novel, ultraslow inactivating sodium current in human ventricular cardiomyocytes. *Circulation*. 98(23):2545-2552.

Maltsev, V.A., Silverman, N., Sabbah, H.N., and Undrovinas, A.I. 2007. Chronic heart failure slows late

sodium current in human and canine ventricular myocytes: implications for repolarization variability. *Eur J heart Fail*. 9(3):219-227.

Maltsev, V.A., Reznikov, V., Undrovinas, N.A., Sabbah, H.N., and Undrovinas, A. 2008. Modulation of late sodium current by Ca2+, calmodulin and CaMKII in normal and failing dog cardiomyocytes: similarities and differences. *Am J Physiol Heart Circ Physiol*. 294:H1597-H1608.

Maltsev, V.A., and Undrovinas, A. 2008. Late sodium current in failing heart: friend or foe? *Prog Biophys Mol Biol*. 96:421-451.

Mangold, K.E., Brumback, B.D., Angsutararux, P., Voelker, T.L.,…, and Silva, J.R. 2017. Mechanisms and models of cardiac sodium channel inactivation. *Channels*. 11(6):517-533.

Mann, D.L., and Bristow, M.R. 2005. Mechanisms and models in heart failure. *Circulation*. 111(21):2837-2849.

Morrow, D.A., Scirica, B.M., Karwatowska-Prokopczuk, E., Murphy, S.A., Budaj, A., Varshavsky, S., Wolff, A.A., Skene, A., McCabe, C.H., and Braunwald, E. 2007. Effects of Ranolazine on recurrent cardiovascular events in patients with non-ST-elevation acute coronary syndromes: The MERLIN-TIMI 36 randomized trial. *JAMA*. 297(16):1775-1783.

Moss, A.J., Zareba, W., Schwarz, K.Q., Rosero, S., McNitt, S., and Robinson, J.L. 2008. Ranolazine shortens repolarization in patients with sustained inward sodium current due to type-3 long-QT syndrome. *J Cardiovasc Electrophysiol*. 19(12):1289-1293.

Munoz-Sanjuan, I., Smallwood, P.M., and Nathans, J. 2000. Isoform diversity among fibroblast growth factor homologous factor is generated by alternative promoter usage and differential splicing. *J Biol Chem*. 275:2589-2597.

Nagatomo, T., January, C.T., and Makielski, J.C. 2000. Preferential block of late sodium current in the LQT3 deltaKPQ mutant by the class I(C) antiarrhythmic flecainide. Mol Pharmacol. 57(1):101-7.

Navarro, M.A., Salari, A., Lin, J.L., Cowan, L.M.,…, and Milescu, L.S. 2020. Sodium channels implement a molecular leaky integrator that detects action potentials and regulates neuronal firing. *eLife*. 9:e54940.

Olsen, S.K., Garbi, M., Zampieri, N., Eliseenkova, A.V., Orniz, D.M., Goldfarb, M., and Mohammadi, M. 2003. Fibroblast growth factor (FGF) homologous factors share structural but not functional homology with FGFs. *J Biol Chem*. 278: 34226-34236.

Ornitz, D.M., and Itoh, N. 2015. The fibroblast growth factor signaling pathway. *Wiley Interdiscip Rev Dev Biol*. 4(3): 215-266.

Pan, X., Li, Z., Zhou, Z., Shen, H.,…, and Yan, N. 2018. Structure of the human voltage-gated sodium channel NaV1.4 in complex with β1. *Science*. 362(6412):eaau2486.

Pitt, G.S., and Lee, S.Y. 2016. Current view on regulation of voltage-gated sodium channels by calcium and auxiliary proteins. *Protein Sci*. 25(9):1573-1584.

Rayner-Hartley, E., and Sedlak, T. 2016. Ranolazine: a contemporary review. *J Am Heart Assoc*. 5:e003196.

Rivolta, I., Abriel, H., Tateyama, M., Liu, H., Memmi, M., Vardas, P., Napolitano, C., Priori, S.G., and Kass,

R.S. 2001. Inherited Brugada and long QT-3 syndrome mutations of a single residue of the cardiac sodium channel confer distinct channel and clinical phenotypes. *J Biol Chem*. 276(33):30623-30630.

Rudoka, M.W., Varga, Z., Schubert, A.R., Asaro, A.B., and Silva, J.R. 2014. The Xenopus oocyte cut-open Vaseline gap voltage-clamp technique with fluorometry. J Vis Exp. 85:e51040.

Rush, A. M., Wittmack, E.K., Tyrrell, L., Black, J.A., Dib-Haji, S.D., and Waxman, S.G. 2006. Differential modulation of sodium channel $Na_V1.6$ by two members of the fibroblast growth factor homologous factor 2 subfamily. *Eur J Neurosci*. 23(10):2551-2562.

Scirica, B.M., Morrow, D.A., Hod, H., Murphy, S.A.,…, and Braunwald, E. 2007. Effect of Ranolazine, an antianginal agent with novel electrphysiological properties, on the incidence of arrhythmias in patients with non-ST-segment-elevation acute coronary syndrome. *Circulation*. 116(15):1647-1652.

Shen, H., Zhou, Q., Pan, X., Li, Z., Wu, J., and Yan, N. 2007. Structural of a eukaryotic voltage-gated sodium channel at near-atomic resolution. *Science*. 355(6328):eaal4326.

Sossalla, S., Maurer, U., Schotola, H., Hartmann, N., Didie, M., Zimmermann, W.H., Jacobshagen, C., Wagner, S., and Maier, L.S. 2011. Diastolic dysfunction and arrhythmias caused by overexpression of CaMKIIdelta(C) can be reversed by inhibition of late Na(+) current. *Basic Res Cardiol*. 106(2):263-272.

Tester, D.J., Will, M.L., Haglund, C.M., and Ackerman, M.J. 2005. Compendium of cardiac channel mutations in 541 consecutive unrelated patients referred for long QT syndrome genetic testing. *Heart Rhythm*. 2:507-517.

Thadani, U. 2004. Current medical management of chronic stable angina. *J Cardiovasc Pharacol Ter*. 9(Supp1):S11-29.

Valdivia, C.R., Chu, W.W., Pu, J.L., Foell, J.D., Haworth, R.A., Wolff, M.R., Kamp, T.J., and Makielski, J.C. 2005. Increased late sodium current in myocytes from a canine heart failure model and from failing human heart. *J Mol Cell Cardiol*. 38(3):475-483.

Varga, Z., Zhu, W., Schubert, A.R., Pardieck, J.L.,…, and Silva, J.R. 2015. Direct measurement of cardiac Na+ channel conformations reveals molecular pathologies of inherited mutations. *Circ Arrhythm Electrophysiol*. 8(5):1228-1239.

Vecchietti, S., Grandi, E., Severi, S., Rivolta, I., Napolitano, C., Priori, S.G., and Cavalcanti, S. 2007. In silico assessment of Y1795C and Y1795H SCN5A mutations: implication for inherited arrhythmogenic syndromes. *Am J Physiol Heart Circ Physiol*. 292(1):H56-65.

Venkatesan, K., Liu, Y., and Goldfarb, M. 2014. Fast-onset long-term open-state block of sodium channels by A-type FHFs mediates classical spike accommodation in hippocampal pyramidal neurons. *J Neurosci*. 34(48):16126-16139.

Wagner, S., Dybkova, N., Rasenack, E.C., Jacobshagen, C.,…, and Maier, L.S. 2006. Ca2+/calmodulin-dependent protein kinase II regulates cardiac Na+ channels. *J Clin Invest*. 116:3127-3138.

Wang, D.W., Yazawa, K., George, Jr., A.L., and Bennett, P.B. 1996. Characterization of human cardiac Na+ channel mutations in the congenital long QT syndrome. *Proc Natl Acad Sci*. 93(23):13200-13205.

Wang, Q., McEwen, D.G., and Ornitz, D.M. 2000. Subcellular and developmental expression of alternatively

spliced forms of fibroblast growth factor 14. *Mech Dev*. 90:283-287.

Wang, C., Hennessey, J.A., Kirkton, R.D., Wang, C.,…, and Pitt, G.S. 2011a. Fibroblast growth factor homologous factor 13 regulates Na+ channels and conduction velocity in murine hearts. *Circ Res*. 109:775-782.

Wang, C., Wang, C., Hoch, E.G., and Pitt, G.S. 2011b. Identification of novel interaction sites that determine specificity between fibroblast growth factor homologous factors and voltage-gated sodium channels. *J Biol Chem*. 286(27):24253-24263.

Wang, C., Chung, B.C., Yan, H., Lee, S.Y., and Pitt., G.S. 2012. Crystal structure of the ternary complex of a NaV C-terminal domain, a fibroblast growth factor homologous factor and calmodulin. *Structure*. 20(7):1167-1176.

Wittmack, E.K., Rush, A.M., Craner, M.J., Goldfarb, M., Waxman, S.G., and Dib-Haji, S.D. 2004. Fibroblast growth factor homologous factor 2B: association with NaV1.6 and selective colocalization at nodes of Ranvier of dorsal root axons. *J Neurosci*. 24(30):6765-6775.

Xiao, M., Bosch, M.K., Nerbonne, J.M., and Ornitz, D.M. 2013. FGF13 localization and organization of the axon initial segment. Mol Cell Neurosci. 56:393-403.

Yan, H., Pablo, J.L., Wang, C., and Pitt, G.S. 2014. FGF14 modulates resurgent sodium current in mouse cerebellar Purkinje neurons. *eLife*. 3:e04193.

Yan, H., Wang, C., Marx, S.O., and Pitt, G.S. 2017. Calmodulin limits pathogenic Na+ channel persistent current. *J Gen Physiol*. 149(2):277-293.

Yang, J., Wang, Z., Sinden, D.S., Wang, X., Shan, B., Yu, X., Zhang, H., Pitt, G.S., and Wang, C. 2016. FGF13 modulates the gating properties of the cardiac sodium channel NaV1.5 in an isoform-specific manner. *Channels (Austin)*. 10(5):410-420.

Yu, F.H., and Catterall, W.A. 2003. Overview of the voltage-gated sodium channel family. Genome Biology. 4:207.

Zhu, W., Varga, Z., and Silva, J.R. 2016. Molecular motions that shape the cardiac action potential: insights from voltage clamp fluorometry. *Prog Biophys Mol Biol*. 120(1-3):3-17.

Zhu, W., Voelker, T.L., Varga, Z., Schubert, A.R., Nerbonne, J.M., and Silva, J.R. 2017. Mechanisms of noncovalent β subunit regulation of Na_V channel gating. *J Gen Physiol*. 149(8):813-831.

Zhu, W., Mazzanti, A., Voelker, T.L., Hou, P.,…, and Silva, J.R. 2019. Predicting patient response to the antiarrhythmic Mexiletine based on genetic variation-Personalized medicine for long QT syndrome. *Circ Res*. 124(4):539-552.

Zhu, W., Wang, Angsutararux, P., Mellor, R.L., Isom, L.L., Nerbonne, J.M., and Silva, J.R. 2021. Modulation of the effects of class Ib antiarrhythmics on cardiac $Na_V1.5$-encoded channels by accessory $Na_V\beta$ subunits. *JCI Insight*. 6(15):e143092.

3.8 Supplementary Figures

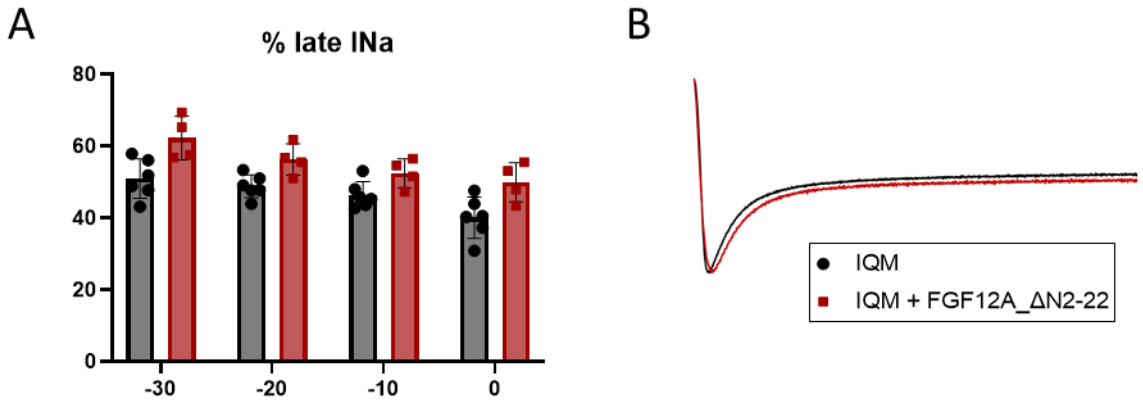

Figure S3.1: The N-terminus of FGF12A is responsible for the late I_{Na} inhibition
(A) The deletion of amino acids 2-22 of FGF12A abolished its ability to reduce late I_{Na} in IQM $Na_V1.5$. (B) Exemplary traces of I_{Na} at -20 mV.

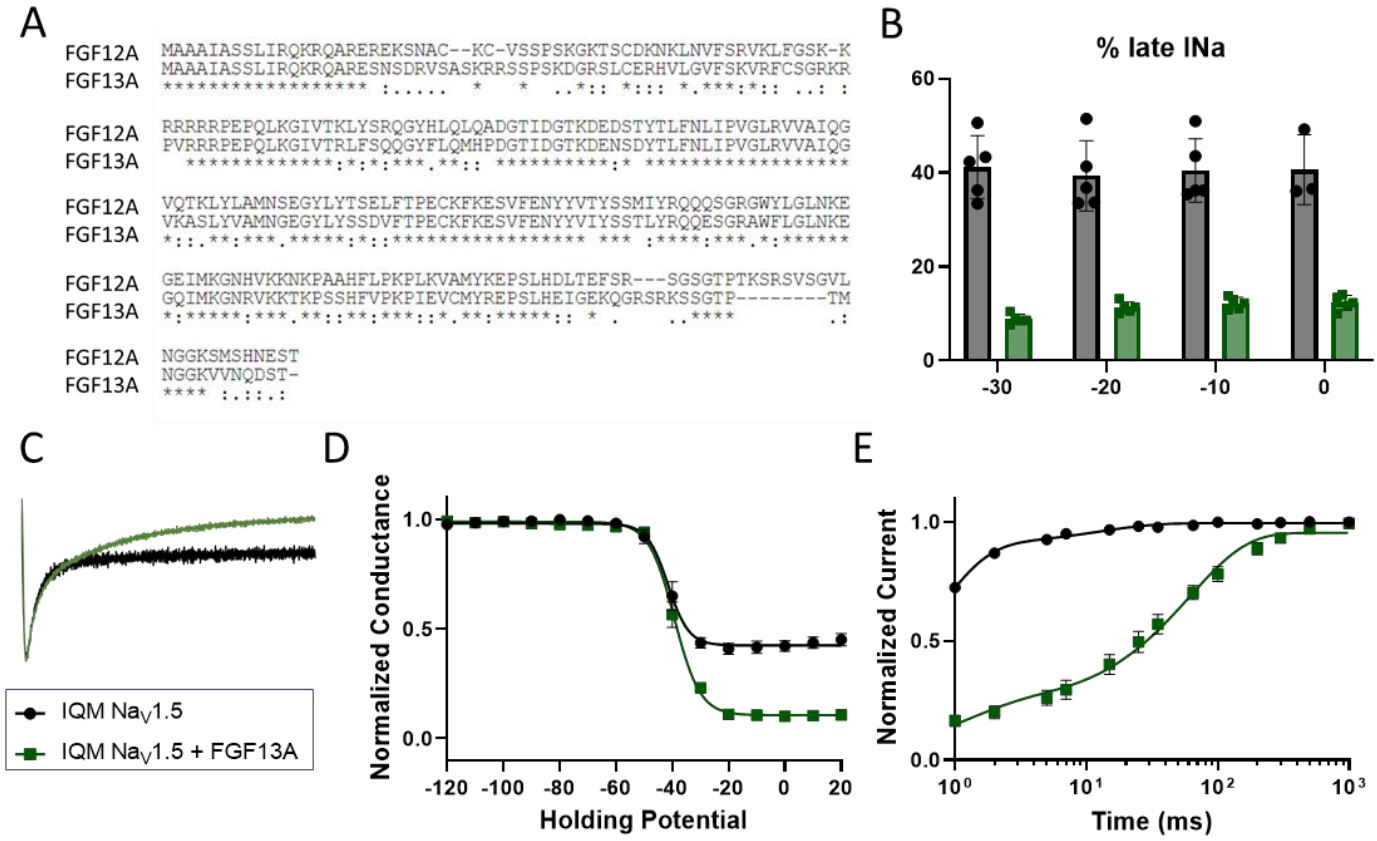

Figure S3.2: FGF13A shows similar effects as FGF12A in IQM $Na_V1.5$
(A) Alignment of FGF12A and FGF13A showed conserved sequence at the N-terminus. (B) FGF13A reduced % late I_{Na} in IQM $Na_V1.5$ at all membrane potentials. **(C)** Exemplary I_{Na} traces at -20 mV showed reduced late I_{Na} in IQM $Na_V1.5$ by FGF13A. **(D)** FGF13A induced more complete inactivation at steady state. **(E)** Recovery from inactivation curve showed unique mechanism of FGF13A as an inactivation particle.

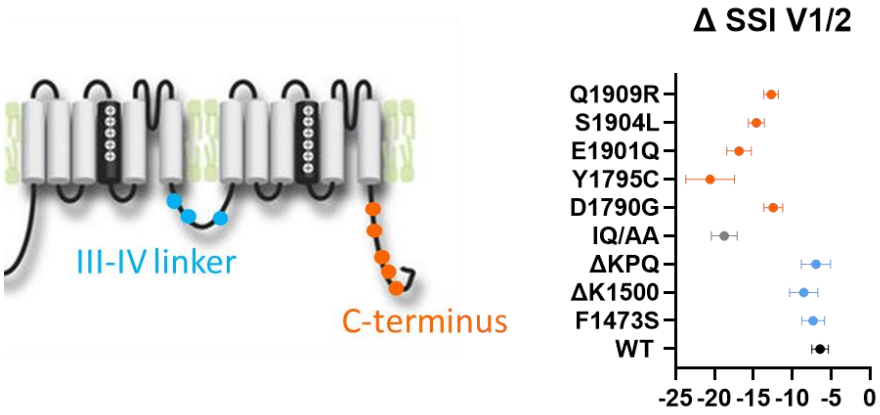

Figure S3.3: FGF12A induced a larger change in SSI $V_{1/2}$ in LQT3-linked variants on the CTD relative to WT $Na_V1.5$
For LQT3-linked $Na_V1.5$ variants that are registered to III-IV linker, FGF12A caused a similar shift in SSI $V_{1/2}$ as in WT $Na_V1.5$. However, when mutations occur in the CTD, that affect the CaM binding affinity, FGF12A induced a larger change in SSI $V_{1/2}$.

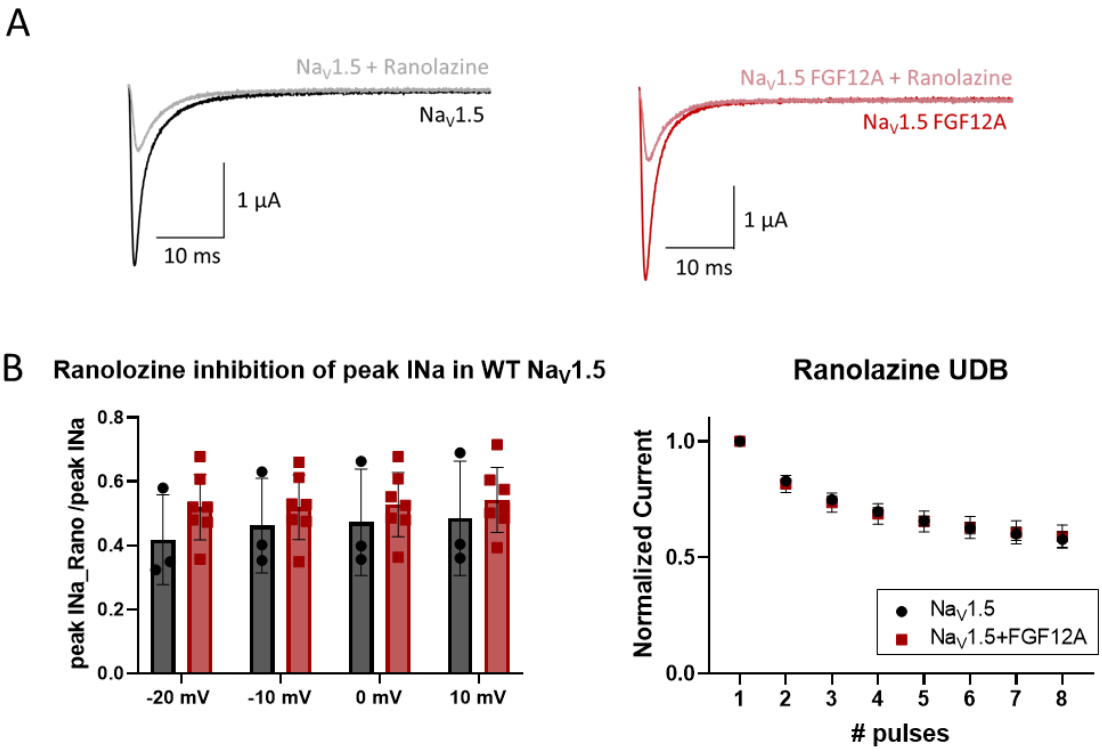

Figure S3.4: FGF12A does not affect Ranolazine pharmacology in WT $Na_V1.5$
(A) Ranolazine reduced peak I_{Na} of WT $Na_V1.5$ and $Na_V1.5$ with FGF12A. **(B)** FGF12A did not alter Ranolazine tonic block (left) nor use-dependent block (right) in WT $Na_V1.5$.

Chapter 4: FlAsH-based FRET assay to investigate dynamics of Na_V channel inactivation

4.1 Abstract

The voltage-gated sodium channels (Na_V) are responsible for initiating and propagating an action potential (AP), the electrical signal generated by excitable cells such as cardiomyocytes and neurons. The inactivation of Na_V channel is a complicated process, involving many parts of the channel and various auxiliary subunits: (1) the Na_V inactivation gate, (2) the Na_V C-terminal domain (CTD), (3) Calmodulin (CaM), and (4) intracellular fibroblast growth factor (iFGF). How these components regulate the Na_V channel inactivation is not well understood. In this study, we developed a Fluoresceine Arsenical Hairpin (FlAsH)-based FRET assay that allows the fluorescent tagging within Na_V channel inactivation gate without disrupting its function. We engineered the short Tetracystein (TC) tag into Na_V channels for the specific FlAsH labeling. We showed that this assay could be applied to test the models and hypotheses of Na_V channel inactivation. This newly developed tool will help us gain insights into the dynamics of Na_V channel inactivation.

4.2 Introduction

An action potential (AP) is the electrical signal generated in excitable cells like myocytes and neurons. Underlying the upstroke or the rising phase of AP is the inward Na^+ current (I_{Na}). Voltage-gated sodium channels (Na_V) are thus responsible for the initiation and propagation of AP. Usually, Na_V channels activate

to depolarize membrane potential, and inactivate within a few milliseconds, to facilitate AP termination. An irregular inactivation of Na_V channel could lead to sustained late I_{Na}, which is pro-arrhythmic.

Na_V α-subunit consists of 4 homologous repeats (I-IV), connected through intracellular linkers. Each repeat contains 6 membrane segments (S1-S6), constituting the voltage-sensor domain (VSD, S1-S4) and the pore module (S5-S6). Between repeats III and IV (III-IV linker) is a short linker where the inactivation gate, also known as the IFMT motif, resides (Hartmann et al., 1994). Na_V channel inactivation also involves another part of the channel, the C-terminal domain (CTD) (Goldin et al., 2003) and auxiliary subunits that bind to the CTD, including Calmodulin (CaM) and intracellular fibroblast growth factor (iFGF) (Wang et al., 2012) (Wang et al., 2014).

Studies of Na_V CTD truncation and the role of CTD in different Na_V subtypes supported the significance of the CTD on Na_V channel inactivation (Descheênes et al., 2001) (Mantegazza et al., 2001). Yet, its regulatory mechanisms are not well understood. Recently, a structure of the cockroach Na_VPaS channel suggested the direct interaction between the III-IV linker and the CTD (Shen et al., 2017) (Clairfeuille et al., 2019). The charge reversal mutations of the interacting interfaces (K1493E and E1784K) yield increased late I_{Na} (Gade et al., 2020) (Gardill et al., 2018). CaM and iFGF were hypothesized to promote this interaction during a closed state through their binding to the CTD (Gade et al., 2020). iFGF interacts with the proximal part of the CTD that forms the globular domain (Chagot et al., 2009), also known as the EF-hand domain, whereas the distal portion of the CTD contains the CaM binding site, or the IQ motif (Bahler & Rhoads, 2002).

CaM is a Ca^{2+}-sensing protein. CaM is postulated to be the key regulator of $Ca2^{+}$-dependent change in Na_V channel inactivation. With elevated Ca^{2+} concentration, CaM caused the depolarizing shifts in steady-state inactivation (Gabelli et al., 2016). CaM consists of two globular domains, N- and C-lobes. Each lobe can bind to 2 Ca^{2+} ions and change its conformation. Based on several available structures of CaM bound to the Na_V CTD under various conditions, the model was proposed that upon Ca^{2+} elevation following Na_V inactivation, CaM is released from the CTD IQ motif to interact with the III-IV linker (Sarhan et al., 2012) (Johnson et al.,

2018). CaM interaction with the III-IV linker destabilizes the inactivation gate and facilitates recovery from inactivation (Johnson et al., 2018). The presence of iFGFs might modulate CaM regulation of Na_V channel gating (Liu, 2003) (Musa, 2015) (Hennessey, 2013) (Wang, 2011).

These mechanistic models were primarily based on the binding affinities, or the NMR structure determined between CaM and purified short peptides of specific Na_V channel segments. So far, the interaction between the III-IV linker and the CTD has not been tested in a whole Na_V channel complex in a cellular environment. In this study, we developed the tool to investigate the interaction between the III-IV linker and the CTD of an intact Na_V channel. Using a Fluorescence Resonance Energy Transfer (FRET) technique combined with the Fluoresceine Arsenical Hairpin (FlAsH) dye, we examined the contributions from auxiliary subunits, CaM and iFGF, to the Na_V channel inactivation. We explored (1) how CaM interact with III-IV linker, (2) whether iFGF interacts with the III-IV linker, and (3) the interaction dynamic between the III-IV linker and the CTD during inactivation.

4.3 Results

4.3.1 Incorporation of the Tetracysteine (TC) tag into $Na_V1.5$ III-IV linker produces functional channel

The main challenge for our study is to introduce fluorescence dye in the III-IV linker without disrupting the Na_V channel function. Conventional fluorescent proteins such as Green Fluorescent Protein (GFP) are too large for our purpose. Instead, we used small fluorescence dye, Fluorescein Arsenical Hairpin binder-Ethanedithiol (FlAsH-EDT_2), that can bind specifically to the short Tetracysteine (TC) tag, consisting of 6 amino acids CCAGCC.

We engineered the TC tag into multiple regions on the III-IV linker of $Na_V1.5$ that is not mutational hotspots **(Fig 4.1A)** through specific point mutations. We measured the ionic sodium currents (I_{Na}) of these III-IV linker TC $Na_V1.5$s in HEK-293 cells and found them all expressed **(Fig 4.1B)**. However, we noticed

alterations in the Na_V channel inactivation for some $Na_V1.5$s with TC tags. Out of the 6 different positions of TC tag we tested (1468TC, 1474TC, 1490TC, 1494TC, 1509TC, and 1515TC), 2 locations showed the most disturbing effects on the Na_V channel inactivation – 1468TC and 1490TC. The incorporation of the TC tag allowed for specific labeling with FlAsH-EDT_2, as demonstrated by HEK cells expressed TC fused to the end of Cerulean **(Fig 4.1C)**.

4.3.2 FlAsH-based FRET assay can be used to probe CaM interaction sites on $Na_V1.5$

Fluorescence Resonance Energy Transfer (FRET) is a distance-dependent nonradiative transfer of energy from the excited fluorophore (Donor) to another fluorophore (Acceptor). FRET efficiency is a good measurement of molecular proximity within short distances (10 – 100 A°) (Babu Sekar & Periasamy, 2003). A previous study showed that Cerulean, an enhanced Cyan Fluorescent Protein (CFP) is a suitable donor for FlAsH-EDT_2 (Hoffmann et al., 2005), which has similar fluorescence as Yellow Fluorescent Protein (YFP). We made the control constructs that link the TC tag to Cerulean at varying linker lengths: 32, 64, and 128 amino acids (Glycine) in between **(Fig. S4.1A)**. We measured FRET efficiency using our custom "three-cube" FRET microscope (see methods) and found an inverse correlation between the linker distances and the FRET efficiencies **(Fig. S4.1B)**.

We tested the FlAsH-based FRET assay by probing the interactions between CaM and its binding site or the IQ motif. We constructed $Na_V1.5$ with the TC tag around the IQ (1908-1909) motif (1896TC, 1911TC, 1917TC, 1922TC, and 1928insTC) **(Fig 4.2A)** and fused Cerulean to the C-terminus of CaM (CaM_Cer). We measured their FRET efficiencies and observed low efficiencies close to the binding sites (1896TC, 1911TC, and 1917TC) **(Fig 4.2B)**. Higher FRET efficiencies were detected when the TC tags were further away (1922TC and 1928insTC), at more than 10 amino acids apart **(Fig 4.2B)**. The low FRET efficiencies at the binding sites could imply that the CaM_Cer binding prevents FlAsH dye from accessing the TC tag, and hence no FRET occurs. This result suggests the pattern of measured FRET efficiencies could estimate the binding site.

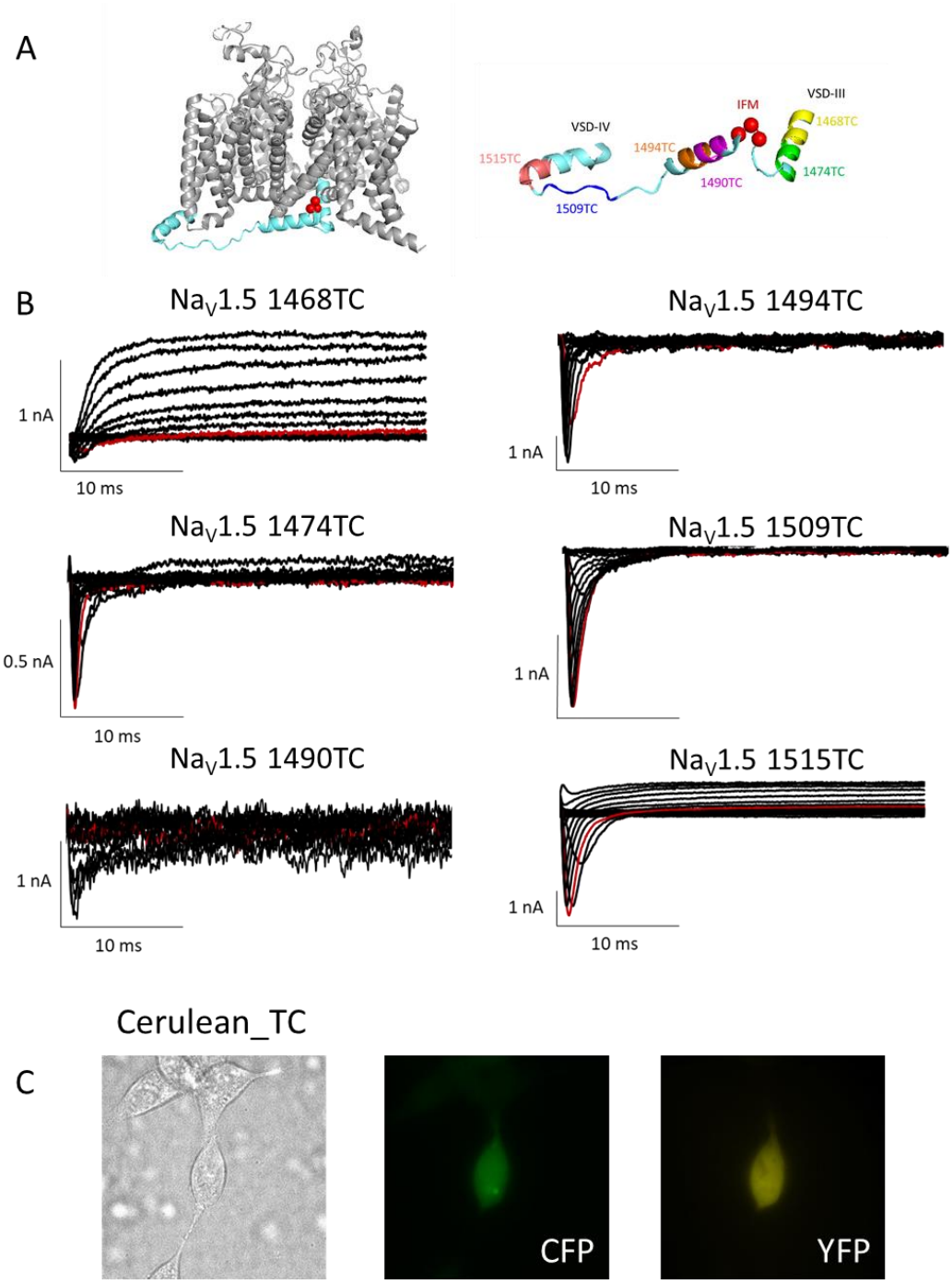

Figure 4.1: Electrophysiology of Na$_V$1.5 with tetracystein (TC) tags engineered to III-IV linker
(A) The structure of cardiac rat Na$_V$1.5 (pdb: 6UZ3), highlighting the III-IV linker (blue) and the inactivation gate IFMT motif (red), showed the sites of engineered TC tags. **(B)** Sodium current (I_{Na}) recordings of all III-IV linker TC Na$_V$1.5s expressed in HEK-293 cells showed functional channels. Some positions of TC tags (1468TC and 1490TC) caused defective inactivation gating in Na$_V$ channels, while other positions (1474TC, 1494TC, 1509TC, and 1515TC) were less disruptive. (C) Cells expressed Cerulean fused with TC tag showed specific labeling with FlAsH-EDT$_2$.

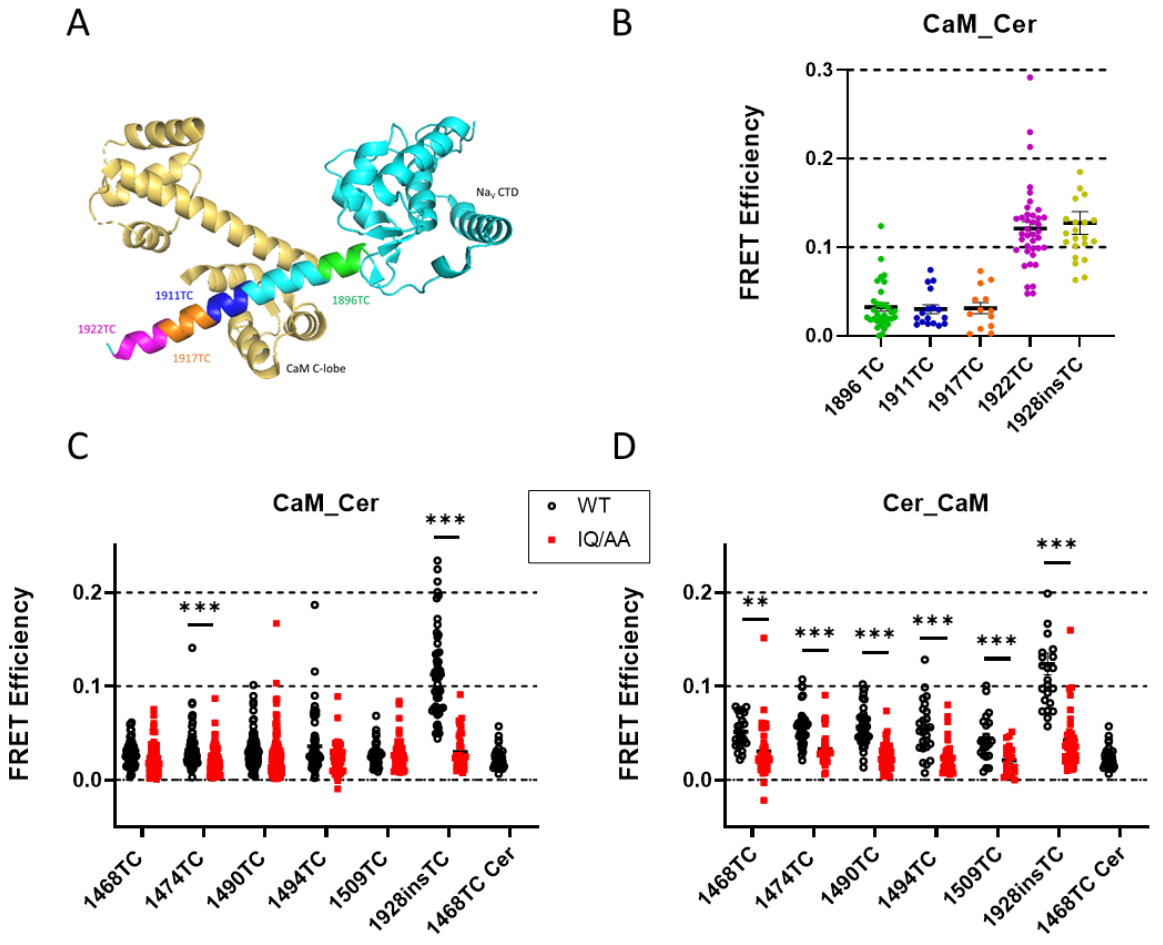

Figure 4.2: FlAsH-based FRET analysis of CaM interactions
(A) The structure of Na$_V$1.5 C-terminal domain (CTD) (blue) in complex with CaM (yellow) (pdb: 4DCK) showed the sites of TC tags around the IQ motif. **(B)** FRET efficiencies can be measured between CaM with Cerulean at the C-terminus (CaM_Cer) and IQ motif TC Na$_V$1.5s labeled with FlAsH-EDT$_2$. The distinct pattern showed no FRET efficiency around the binding sites, but high FRET efficiencies when the TC tags were further away. **(C)** The IQ/AA mutation was introduced into III-IV linker TC Na$_V$1.5s, to use as the negative control when there is no CaM binding. FRET efficiencies between CaM C-lobe (CaM_Cer) and III-IV linker were compared between WT and IQ/AA background and showed no significant difference. **(D)** Cerulean was added to the N-terminus of CaM (Cer_CaM) to test CaM N-lobe interaction with III-IV linker. In comparison to IQ/AA background, higher FRET efficiencies in WT background implied that CaM N-lobe is close to III-IV linker but does not bind to it.

4.3.3 CaM does not bind to the III-IV linker but interacts with it through its N-lobe

Next, we examined whether CaM interacts with the III-IV linker and through which lobe. Cerulean was added to CaM, either its N- or C-terminus (Cer_CaM and CaM_Cer). The IQ/AA mutation that removes CaM binding was a negative control. We compared FRET efficiencies between CaM and III-IV linker TC Na$_V$1.5s in WT background to IQ/AA mutation. There was no FRET efficiency in 1928insTC IQ/AA Na$_V$1.5 with

neither Cer_CaM nor CaM_Cer, confirming the absence of CaM. Using CaM_Cer, we detected small FRET efficiencies with III-IV linker TC $Na_V1.5$s of WT background, which were not significantly higher than IQ/AA background **(Fig 4.2C)**. We concluded that the C-lobe of CaM was not close to the III-IV linker and likely remained bound to the IQ motif.

In contrast, Cerulean attached to the N-lobe of CaM (Cer_CaM) yielded higher FRET efficiencies with almost all III-IV linker TC $Na_V1.5$ in WT background compared to IQ/AA background **(Fig 4.2D)**. All positions of TC tags on the III-IV linker produced similar FRET efficiencies. This result implies the potential interaction between CaM N-lobe and III-IV linker, but not direct binding.

4.3.4 FGF12B also interacts with III-IV linker

We further investigated the interaction between FGF12B and $Na_V1.5$. First, we confirmed the FRET efficiencies between Na_V CTD and FGF12B, by engineering TC tags to the EF-hand domain (1851TC, 1860TC, 1860insTC, 1866TC, 1880TC, and 1887TC) and fusing Cerulean to the N-terminus of FGF12B (Cer_FGF12B) **(Fig 4.3A)**. We selected the positions of TC tags around the FGF12 binding site. As expected, we detected FRET efficiencies between EF-hand TC $Na_V1.5$s and Cer_FGF12B. Interestingly, we did not observe the same pattern of FRET efficiencies as CaM_Cer and IQ-motif TC $Na_V1.5$s. All EF-hand TC $Na_V1.5$s produced similar FRET efficiencies **(Fig 4.3B)**. The difference in the FRET efficiencies pattern implied a difference in interaction nature between FGF12B and CaM on the $Na_V1.5$ CTD. Possibly, FGF12B does not constitutively bind to the EF-hand domain but interact dynamically so that FlAsH-EDT_2 dye can access all TC tags. Another possibility is that FGF12B binds to the EF-hand domain with less affinity than CaM on the IQ motif and thus does not prevent the FlAsH-EDT_2 dye labeling.

Then, we tested FRET efficiencies between Cer_FGF12B and III-IV linker TC $Na_V1.5$s. All positions of TC tags yielded FRET efficiencies that were higher around the IFMT motif (1485-1488) **(Fig 4.3C)**. FRET efficiencies between III-IV linker TC $Na_V1.5$s and Cer_FGF12B were larger than those measured with

Cer_CaM, suggesting FGF12B is closer to III-IV linker than CaM N-lobe.

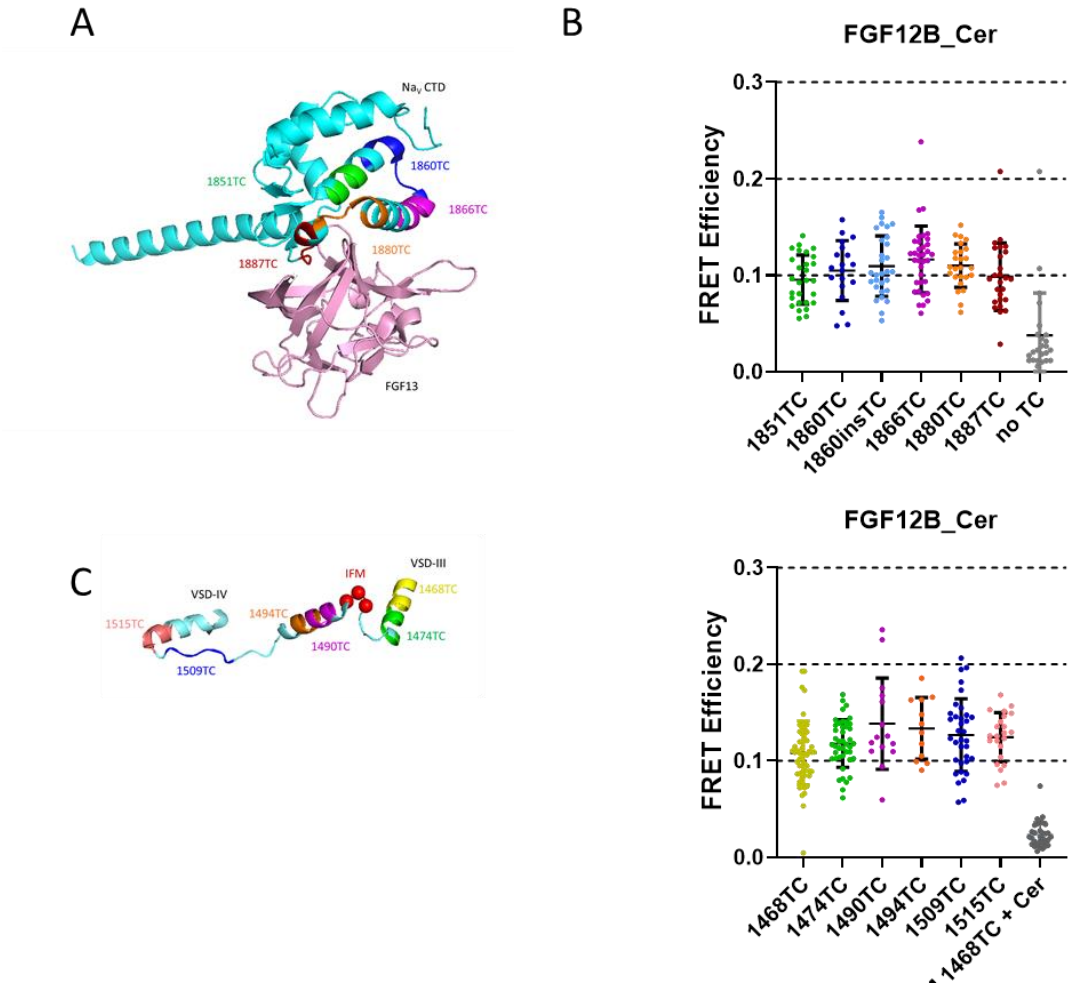

Figure 4.3: FlAsH-based FRET analysis of FGF12B interactions
(A) The structure of Na$_V$1.5 CTD (blue) in complex with FGF13 (blue) (pdb: 4DCK) showed the sites of TC tags around the EF-hand domain. **(B)** FRET efficiencies can be measured between FGF12B with Cerulean at the C-terminus (FGF12B_Cer) and EF-hand TC Na$_V$1.5s labeled with FlAsH-EDT2. All positions of TC tags showed similar FRET efficiencies, implying that FGF12B does not bind tightly to EF-hand domain. **(C)** The IQ/AA mutation was introduced into III-IV linker TC Na$_V$1.5s, to use as the negative control when there is no CaM binding. FRET efficiencies between CaM C-lobe (CaM_Cer) and III-IV linker were compared between WT and IQ/AA background and showed no significant difference. **(D)** FRET efficiencies were measured between FGF12B_Cer and III-IV linker TC Na$_V$1.5s labeled with FlAsH-EDT$_2$. All positions of TC tags showed similar FRET efficiencies.

4.3.5 FGF12B interaction remains in inactivation impaired Na$_V$ channels

Because FGF12B regulates the inactivation of Na$_V$ channel, we tested whether the impaired inactivation affects FGF12B's interaction with the III-IV linker. We mutated the IFMT motif to IQM mutation in the

background of III-IV TC $Na_V1.5$s and measured their FRET efficiencies with Cer_FGF12B. The comparison of FRET efficiencies between WT and IQM backgrounds showed a slight decrease upon IQM mutation, but the mutation did not abolish the interaction **(Fig 4.4A)**.

We introduced another mutation E1784K to sever the interaction between the III-IV linker and the CTD. This mutation also impairs fast inactivation, resulting in increased late I_{Na}. Still, we did not observe a significant reduction in FRET efficiencies between FGF12B and Na_V III-IV linker by E1784K relative to WT **(Fig 4.4B)**. These results informed us that FGF12B is close to III-IV linker, even when the inactivation was compromised.

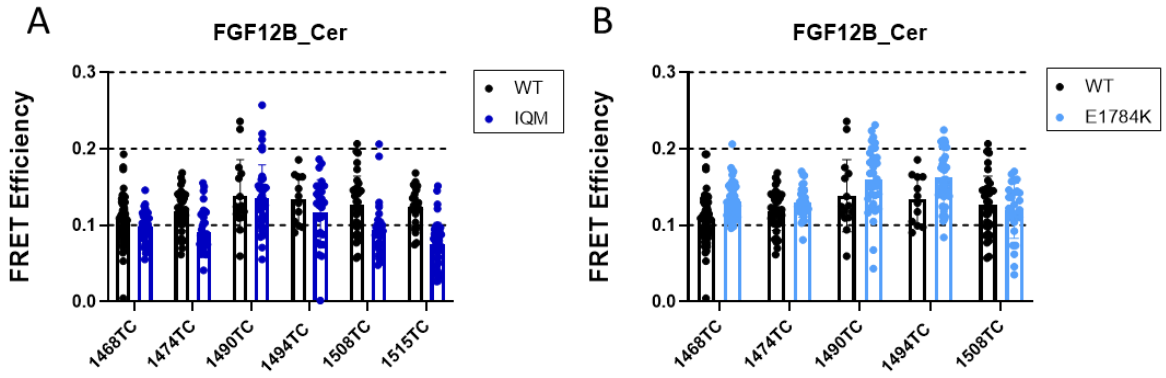

Figure 4.4: FGF12B interaction with III-IV linker remains in inactivation-impaired Na_V channels
(A) The mutation of IFMT motif to IQM impairs fast inactivation. However, the interactions between FGF12B and III-IV linker was not abolished. Slightly decrease in FRET efficiencies was observed. **(B)** The E1784K mutation severs interaction between III-IV linker and the CTD and impairs inactivation. There was no significant difference in FRET efficiencies between FGF12B and III-IV linker of E1784K background, relative to WT.

4.3.6 Conformational changes within the Na_V channel during inactivation

All the FRET results we measured represented the interactions during a closed state. To investigate the interactions during Na_V channel inactivation, we used HEK-293 cells that stably express inward rectifying potassium (K_{ir}) channels (Shandell et al., 2019). K_{ir} channels are common in excitable cells like myocytes. They conduct inward K^+ current (I_{K1}) more than outward current. In low K^+ solution (HBSS), K_{ir} channels conduct outward I_{K1}, resulting in hyperpolarized membrane potential. When the solution was exchanged to high K^+, a huge inward I_{K1} depolarizes the membrane potential, leading to Na_V channels activation. The

perfusion of high K+ solution will induce Na_V channels into the fast inactivated states.

We first determined the change in Na_V CTD by attaching Venus to the very end of $Na_V1.5$ CTD ($Na_V1.5$_Ven). For negative control, we co-expressed $Na_V1.5$_Ven with Cerulean (Cer). As expected, most cells yielded low FRET efficiency. The solution was exchanged from HBSS (pre) to HBSS with high K^+ (100 mM KCl or 140 mM KCl) and back to HBSS (post). We calculated FRET efficiency and the change in FRET efficiency relative to pre-solution exchange value per cell. Cells expressing negative control constructs showed inconsistent FRET efficiency changes upon solution exchange, and the changes post-high K^+ solution did not return to 0 **(Fig 4.5A)**. We then tested the interaction between $Na_V1.5$ CTD and FGF12B with Cerulean attached to the N-terminus (Cer_FGF12B) or CaM with Cerulean attached to the C-terminus (CaM_Cer). With Cer_FGF12B, we noticed most of the changes occurred in the same direction **(Fig 4.5B)**. FRET efficiency increased upon high K^+ solution and returned to almost the same level as pre-solution exchange. The changes in FRET efficiency post-solution exchange were close to 0 for most cells **(Fig 4.5B)**. In contrast, with CaM_Cer, the changes in FRET efficiencies occurred in both directions **(Fig 4.5C)**. Also, post-solution exchange FRET efficiencies did not return to the pre-solution exchange values.

The following experiment examined the change in interactions between the III-IV linker and the CTD, or auxiliary subunits, during inactivation. We picked $Na_V1.5$ with a 1515TC tag because of its functional inactivation gating. First, we tested the interaction with the very end of the CTD by adding Cerulean to the $Na_V1.5$ 1515TC ($Na_V1.5$ 1515TC_Cer). We noticed a homogenous increase in FRET efficiency upon high K^+ solution exchange and the return of FRET efficiencies close to the pre-solution exchange values **(Fig 4.6A)**. This result showed that the III-IV linker was more proximal to the CTD upon Na_V channel inactivation. Then, we studied the interactions between the III-IV linker ($Na_V1.5$ 1515TC) and Cer_FGF12B or CaM_Cer. We observed the non-uniform changes in FRET efficiencies and the deviations in FRET efficiencies post-solution exchange from pre-solution exchange values **(Fig 4.6B, C)**.

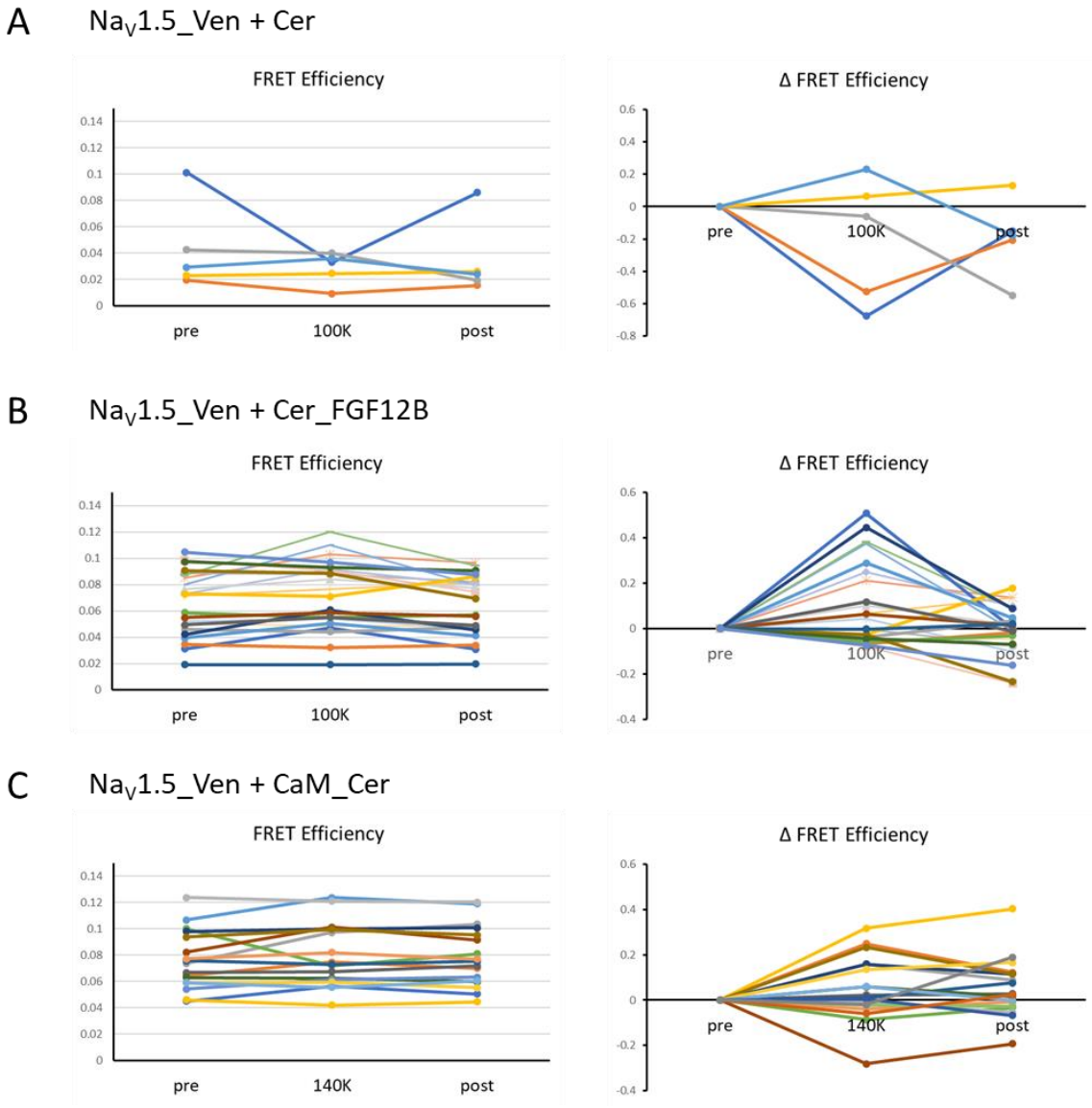

Figure 4.5: Changes in Na$_V$ CTD interactions during inactivation
We employed HEK cells that stably expressed inward rectifier K+ channel (K_{ir}) for the study of Na$_V$ channel inactivation. The exchange of low K+ solution to high K+ solution leads to large influx of K+ current through K_{ir} (I_{K1}) and the depolarization of membrane potential. We measured FRET efficiency in low K^+ solution (pre), then perfused with high K^+ solution (100K and 140K) before switching back to low K+ solution (post). The change in FRET efficiency was calculated, in relative to pre-solution exchange condition. **(A)** FRET efficiency between Cerulean and Venus attached to the end of Na$_V$1.5 CTD (Na$_V$1.5_Ven) served as the negative control. We detected low FRET efficiency and no uniform change during perfusion. **(B)** FRET efficiency between FGF12B with Cerulean attached to its N-terminus and Na$_V$1.5_Ven showed consistent increase in FRET efficiency during inactivation in most cells. The change in FRET efficiency returned to almost 0 in post-solution exchange condition. **(C)** FRET efficiency between CaM with Cerulean attached to its C-terminus and Na$_V$1.5_Ven showed no uniformed change in FRET efficiency, similar to negative control in (A).

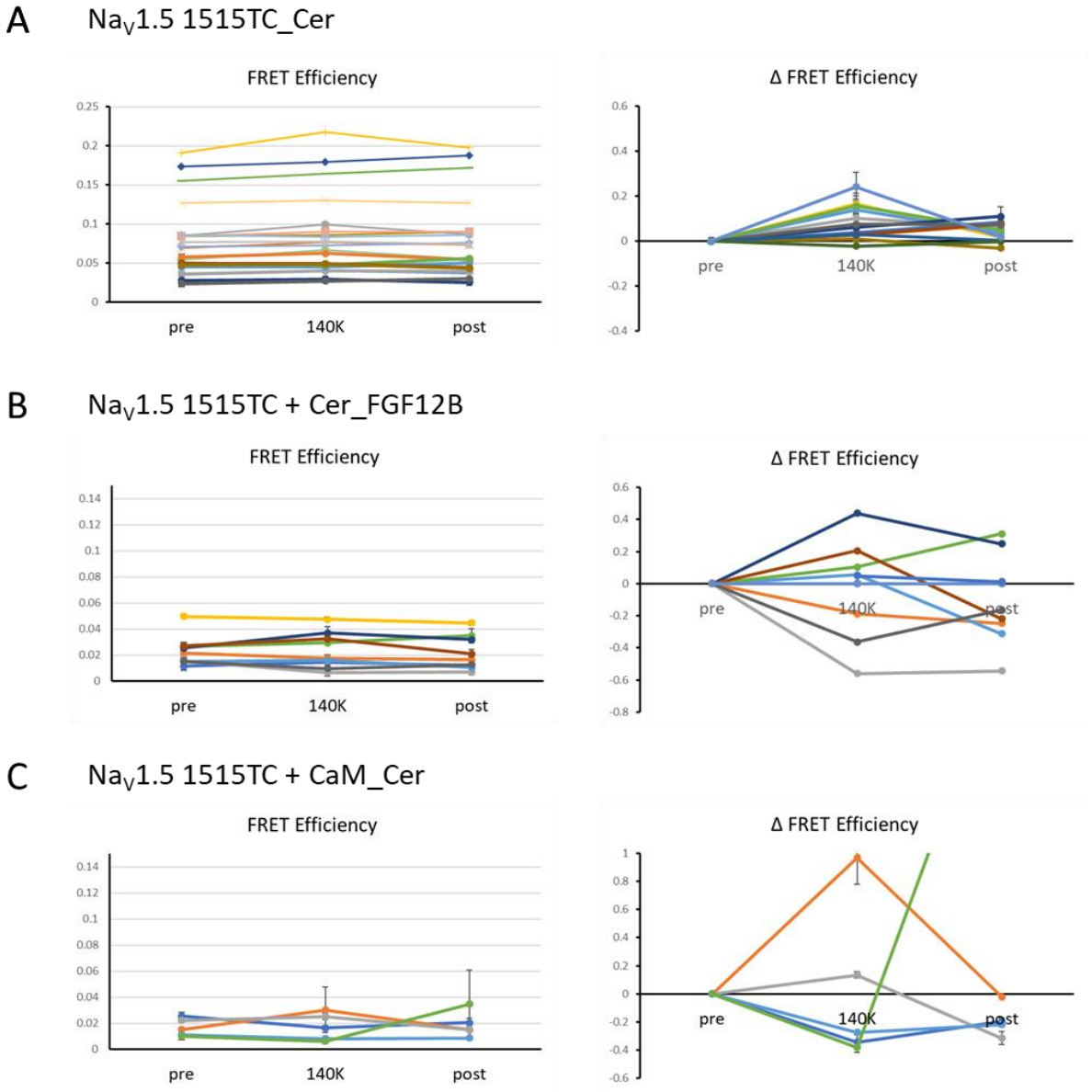

Figure 4.6: Changes in Na$_V$ III-IV linker interactions during inactivation
We used Na$_V$1.5 with 1515TC to test III-IV linker interaction during inactivation. **(A)** Cerulean was added to the C-terminus of Na$_V$1.5 1515TC and FRET efficiency was measured. Homogenous increase in FRET efficiency during inactivation was detected. **(B)** FRET efficiency was measured between Na$_V$1.5 1515TC and FGF12B with Cerulean added to its N-terminus and showed no uniform change upon inactivation. **(C)** There was no consistent change in FRET efficiency between Na$_V$1.5 1515TC and CaM with Cerulean added to its C-terminus during inactivation.

4.4 Discussion

Na_V channel inactivation is a complicated process that involves multiple parts of the channel (III-IV linker and the CTD) and many auxiliary subunits (CaM and iFGF). There is much debate about the mechanisms involving all these components. Recent structures of eukaryotic Na_V channels give insights into molecular details of how the IFMT motif inactivates the Na_V channel. However, the key CTD was missing. Here, we developed the new tool of FlAsH-based FRET assay that incorporated the fluorescent dye into the III-IV linker without disrupting Na_V channel inactivation gating. This tool allows us to investigate the dynamics of Na_V channel inactivation. We can examine the interplay of Na_V channel inactivation gate and the CTD, including auxiliary subunits bound to it.

4.4.1 CaM C-lobe binds to the IQ motif and remains there during inactivation

Through FRET efficiency analysis combined with mutagenesis studies, we showed that CaM binds to the IQ motif, specifically through its C-lobe. CaM N-lobe can interact with the III-IV linker but does not bind to it. It is important to note that these interactions likely reflect closed-state channels in low Ca^{2+} conditions. Depolarizing the membrane potential caused no significant change in FRET efficiencies between CaM C-lobe and the Na_V CTD or III-IV linker. These results implied that CaM C-lobe remains on the IQ motif during inactivation. CaM does not entirely leave the IQ motif to bind to III-IV linker. How CaM N-lobe interacts with III-IV linker change during inactivation or under elevated Ca^{2+} remains to be tested.

4.4.2 FGF12B interacts with the III-IV linker independent of the state of inactivation

Results showed that the C-terminus of FGF12B interacts with the III-IV linker similarly as it interacts with the CTD EF-hand domain. Unlike CaM binding to the IQ motif, FGF12B does not bind tightly to the CTD, as observed by the different patterns of FRET efficiencies. Interacting sites between the III-IV linker and the CTD were identified at K1493-E1784 in $Na_V1.5$. Surprisingly, the charge reversal E1784K mutation did not affect the FRET efficiencies between FGF12B and III-IV linker, suggesting more extensive interactions

between 2 parts. The recent cryo-EM structure of E1784K $Na_V1.5$ also illustrates the exact orientation of the III-IV linker in E1784K, as in WT $Na_V1.5$ (Li et al., 2021).

Further examination of the inactivation impaired channel IFM/IQM $Na_V1.5$ showed a slight reduction in FRET efficiencies between FGF12B and III-IV linker, but not total absence. The structure of the Na_V channel with QQQ mutation in the IFMT motif showed a flexible III-IV linker (Jiang et al., 2021), the IQM mutation might not be as severe as the QQQ mutation, and some helical structure may retain in the III-IV linker allowing for its interaction with the CTD. Altogether, these results implied no substantial change in the interactions between Na_V CTD EF-hand domain and III-IV linker even when inactivation is impaired. Potentially, FGF12B promotes or stabilizes the interaction between the III-IV linker and the CTD (Gade et al., 2020).

We observed no significant change when we measured the change in FRET efficiency between NaV1.5 1515TC and Cer_FGF12B during inactivation. Instead, there was an increase in FRET efficiency between the FGF12B N-terminus and the end of Na_V CTD. This change in FRET efficiency supports the intermolecular interaction model between the CTD of two NaV1.5s, showing contacts between the EF-hand domain of one $Na_V1.5$ and the end of CTD of another $Na_V1.5$ (Gabelli et al., 2014). This model also agrees with the increase in FRET efficiency between the III-IV linker and the end of Na_V CTD that we observed. Our results suggested that during inactivation, the end of one Na_V CTD can interact with the EF-hand domain of another Na_V CTD. This EF-hand domain remains near the III-IV linker and interacts with FGF12B.

4.4.3 Limitations and future directions

In this study, the FRET efficiencies that we measured were relatively low (< 0.2), and low FRET efficiency can limit the assay's sensitivity. We also noticed the wide range of FRET efficiencies, likely due to variable transfection efficiencies among different cells. FRET efficiency depends on the concentration of both Donor and Acceptor fluorophores and their relative ratios. If there is a much higher Donor concentration than

Acceptor, then measured FRET efficiency will be small. On the contrary, the much higher Acceptor concentration relative to Donor will make the FRET correction during analysis inaccurate. We measured FRET efficiency for an individual cell. We cannot control how much each cell will express Donor and Acceptor molecules. Obtaining data from a larger number of cells could help reduce variabilities in FRET efficiencies.

We used a perfusion system to depolarize the membrane potential and induce Na_V channels into inactivation. The slow exchange of the old and the new solution limits our ability to measure the spontaneous change in FRET efficiency. We have to wait for a few minutes to ensure a complete solution exchange before taking the FRET image. This procedure means that we can only observe the change in FRET efficiency over steady-state inactivation. The fast inactivation dynamics within a range of a few milliseconds are impossible to measure with our current perfusion setup. To do so, we will need to apply a patch-clamp fluorometry technique to our FlAsH-based FRET assay. The simultaneous measurements of fluorescence signals and ionic current will allow us to track the rapid conformation changes within the Na_V channel during the fast inactivation.

4.5 Materials and Methods

4.5.1 Molecular biology

All Tetracysteine (TC) tags were introduced into *SCN5A* gene, encoded for $Na_V1.5$ (UniprotKB identifier: Q14524-1), by replacing the 6 amino acids starting from the indicated number with CCPGCC. Primers, with overlap extension, were made commercially (Integrated DNA Technologies, Coralville, IA). We used a two-step PCR approach to engineer the TC tag into $Na_V1.5$ plasmid. We added Cerulean or Venus sequences to either N- or C-terminus of CaM and FGF12B with a GSGSGS linker in between.

The engineered plasmids were transformed into E.coli competent cells. The colony was picked and expanded. We purified the engineered DNA plasmids using Miniprep (MACHEREY-NAGEL), and the plasmids were

sequenced to confirm successful mutagenesis.

4.5.2 Cell culture and plasmid transfection

HEK-293 cells and HEK-293 stably expressed K_{ir} were maintained in HEK medium containing DMEM basal medium (Gibco) with 10% Fetal Bovine Serum (Gibco) and 100 U/ml Penicillin-Streptomycin (Lonza Bioscience), at 37 °C and 5% CO_2. Cells were passaged every 2-3 days when they reached 80% confluency, using TrypLE Express (Gibco). For transfection, HEK-293 cells were seeded one day before the transfection in a 35-mm dish one day to get approximately 60% confluency. A total of 60 ng DNA was transfected per each 35-mm dish, using jetOPTIMUS reagent (Polyplus) following the company's protocol. We used a 2:1 mass ratio between $Na_V1.5$ and CaM or $Na_V1.5$ and FGF12B (equivalent to a 4:1 molar ratio).

4.5.3 FlAsH-EDT_2 labeling

We followed the protocol adapted from Hoffmann et al. (Hoffmann et al., 2010). In brief, cells were washed three times with Hank's balanced salt solution (HBSS) containing $CaCl_2$ and $MgCl_2$ (Gibco) and incubated at 37 °C for 1 hr with 500 nM FlAsH-EDT_2 (Cayman Chemical) and 12.5 μM EDT_2 in HBSS. Next, cells were rinsed and incubated in HBSS containing 50 mM 2,3-dimercaptoproponol (British anti-Lewisite or BAL) wash for 20 min at 37 °C to block nonspecific labeling. Lastly, cells were washed three times with HBSS to remove residual BAL solution. Cells were kept at 37 °C until imagining, usually within a few hours.

4.5.4 FRET imaging

FRET imaging was done within 24-48 hrs after the transfection of the cells. The old medium was aspirated, and cells were washed three times with HBSS. We imaged the cells in either HBSS (low K^+ solution) or HBSS with 100 mM and 140 mM KCl (high K^+ solution). We used a Nikon Eclipse Ti-U inverted microscope customed to the "3-cube" FRET setting. The LED light source Spectra III (Lumencor) provides excitation for Cerulean (excitation filter: 440/20) and Venus or FlAsH (excitation filter: 510/25 nm) via CFP and YFP lines

accordingly. Cerulean is enhanced Cyan Fluorescent Protein (CFP), and Venus is enhanced Yellow Fluorescent Protein (YFP). FlAsH-EDT_2 shares similar fluorescence as YFP.

The microscope was outfitted with a triple-band dichroic beamsplitter (FF459/526/596-Di01, Semrock) and a triple-band emitter (FF01-475/543/702-25, Semrock) to reduce background illumination from the irrelevant wavelength. The fluorescence output was passed into an OptoSplit II Bypass emission image splitter (Cairn Research) fitted with a 505nm beamsplitter (T5051pxr, Chroma Color Corporation). The emission signal was separated into two channels with the filters for Cerulean (emission filter: ET480/40 nm, Chromo Color Corporation) and Venus (emission filter: ET545/50nm, Chroma Color Corporation) wavelengths. The image was acquired via an Andor iXon EMCCD camera (Andor Technology), utilizing one-half of the camera sensor for each emission channel and capturing two signals simultaneously. The Spectra III light engine and Andor iXon EMCCD camera were controlled via a Digidata 1440A (Molecular Devices), driven by pClamp software (Molecular Devices).

The system activated Cerulean excitation for 1 second, and the camera captured the image at a 10-ms delay. Then, the Venus or FlAsH excitation was triggered to repeat the imaging process. Each image displayed the Cerulean emission channel in one half of the screen and the Venus emission channel in the other half. A total of 3 FRET channels were collected per sample: (1) the donor channel (excitation: 440/20, emission: 480/40), (2) the FRET channel (excitation: 440/20, emission: 545/50), and (3) the acceptor channel (excitation: 510/25, emission: 545/50).

4.5.5 FRET Data analysis

FRET data were analyzed with MATLAB (MathWorks) using a code developed in the lab. For each acquired data, three images from (1) donor channel, (2) FRET channel, and (3) acceptor channel were calculated for fluorescence signals as background-subtracted and cell average. We obtained S(Donor), S(FRET), and S(Acceptor) for each data. We used two controls, cells expressed with Donor fluorophore only and cells

expressed with Acceptor fluorophore only, to correct for signal crosstalk or the direct emissions from Donor and Acceptor fluorophores when excited with Cerulean excitation. Two constants, R_{D1} and R_{A1}, were calculated.

$$R_{D1} = \frac{S(FRET)}{S(Donor)} \text{ from cells expressing only Donor fluorophore}$$

$$R_{A1} = \frac{S(FRET)}{S(Acceptor)} \text{ from cells expressing only Acceptor fluorophore}$$

The corrected FRET signal (AFRET) was then calculated from cells expressing both Donor and Acceptor fluorophores by subtracting the direct emission of Donor (DDirect) and Acceptor (ADirect).

$$AFRET = S(FRET) - DDirect - ADirect$$

where $DDirect = R_{D1} \cdot S(Donor)$ and $ADirect = R_{A1} \cdot S(Acceptor)$

The apparent FRET efficiency can be reported using either an acceptor-centric (EA) or a donor-centric (ED) method

$$EA = \frac{AFRET}{ADirect} \cdot \frac{g(A)}{g(D)} \quad \text{and} \quad ED = \frac{AFRET}{AFRET + \frac{f(A)}{f(D)} \cdot DDirect}$$

where g(A)/g(D) and f(A)/f(D) are constants related to the properties of fluorophores used and microscope specification. They can be calculated from the control constructs that link Donor and Acceptor fluorophores directly with linkers of varying lengths (Ben-Johny et al., 2016) (Butz et al., 2016). These constants were obtained multiple times to ensure the stable FRET setup.

The number of Donor and Acceptor molecules could be estimated as the following

$$[Donor] = \frac{R_{D1} \cdot S(Donor)}{(1 - ED) \cdot MD}$$

$$[Receptor] = \frac{R_{A1} \cdot S(Accaptor)}{MA}$$

where $\frac{MA}{MD} = \frac{f(A)/f(D)}{g(A)/g(D)}$ and MD can be set to 1

4.6 References

Babu Sekar, R., and Periasamy, A. 2003. Fluorescence resonance energy transfer (FRET) microscopy imaging of love cell protein localizations. *J Cell Biol*. 160(5):629-633.

Bahler, M., and Rhoads, A. 2002. Calmodulin signaling via the IQ motif. *FEBS Lett*. 513(1):107-113.

Ben-Johny, M., Yue, D.N., and Yue, D.T. 2016. Detecting stoichiometry of macromolecular complexes in live cells using FRET. *Nat Commun*. 7:13709.

Butz, E.S., Ben-Johny, M., Shen, M., Yang, P.S., Sang, L., Biel, M., Yue, D.T., and Wahl-Schott, C. 2016. Quantifying macromolecular interactions in living cells using FRET two-hybrid assays. *Nat Protoc*. 11(12):2470-2498.

Chagot, B., Potet, F., Balser, J.R., and Chazin, W.J. 2009. Solution NMR structure of the C-terminal EF-hand domain of human cardiac sodium channel NaV1.5. *J Biol Chem*. 284(10):6436-6445.

Clairfeuille, T., Cloake, A., Infield, D.T., Llongueras, J.P.,…, and Payandeh, J. 2019. Structural basis of α-scorpion toxin action on NaV channels. *Science*. 363(6433):eaav8573.

Deschênes, I., Trottier, E., and Chahine, M. 2001. Implication of the C-terminal region of the α-subunit of voltage-gated sodium channels in fast inactivation. *J Membr Biol.* 183:103-114.

Gabelli, S.B., Boto, A., Kuhns, V.H., Bianchet, M.A.,…, and Amzel. M.L. 2014. Regulation of the NaV1.5 cytoplasmic domain by calmodulin. *Nat Commun*. 5:5126.

Gabelli S. B., Yoder J. B., Tomaselli G. F., and Amzel M. 2016. Calmodulin and Ca2+ control of voltage gated Na+ channels. *Channels*, 10(1):45-54.

Gade, A.R., Marx, S.O., and Pitt, G.S. 2020. An interaction between the III-IV linker and CTD in NaV1.5 confers regulation of inactivation by CaM and FHF. *J Gen Physiol*. 152(2):e201912434.

Gardill, B.R., Rivera-Acevedo, R.E., Tung, C.C., Okon, M., McIntosh, L.P., and Petegem, F.V. 2018. The voltage-gated sodium channel EF-hands form an interaction with the III-IV linker that is disturbed by disease-causing mutations. *Sci Rep*. 8:4483.

Goldin, A.L. 2001. Resurgence of sodium channel research. Annu Rev Phsyiol. 63:871-894.

Hartmann, H.A., Tiedeman, A.A., Chen, S.F., Brown, A.M., and Kirsch, G.E. 1994. Effects of III-IV linker mutations on human heart Na+ channel inactivation gating. *Circ Res*. 75(1):114-122.

Hennessey, J.A., Wei, E., and Pitt, G. 2013. Fibroblast growth factor homologous factors modulate cardiac calcium channel. *Circ Res*. 223(4):381-388.

Hoffmann, C., Gaietta, G., Bunemann, M., Adams, S.R., Oberdorff-Maass, S., Behr, B., Vilardaga, J., Tsien, R.Y., Ellisman, M.H., and Lohse, M.J. 2005. A FlAsH-base FRET approach to determine G protein-coupled receptor activation in living cells. *Nat Methods*. 2(3):171-176.

Hoffmann, C., Gaietta, G., Zurn, A., Adams, S.R., Terrillon, S., Ellisman, M.H., Tsien, R.Y., and Lohse, M.J. 2010. Fluorescent labeling of tetraceysteine-tagged proteins in intact cells. *Nat Protoc*. 5(10):1666-1677.

Jiang, D., Banh, R., Gamal El-Din, T.M., Tonggu, L., Lenaeus, M.J., Pomes, R., Zheng, N., and Catterall, W.A. 2021. Open-state structure and pore gating mechanism of the cardiac sodium channel. *Cell*. 184(20):5151-5162.

Johnson, C.N., Potet, F., Thompson, M.K., Kroncke, B.M., Glazer, A.M., Voehler, M.W., Knollmann, B.C., George, A.L., and Chazin, W.J. 2018. A mechanism, of calmodulin modulation of the human cardiac sodium channel. *Structure*. 26:683-694.

Li, Z., Jin, X., Wu, T., and Yan, N. 2021. Structure of human NaV1.5 reveals the fast inactivation-related segments as a mutational hotspot for the long QT syndrome. *Proc Natl Acad Sci*. 118(11):e2100069118.

Liu, C.J., Dib-Haji, S.D., Renganathan, M., Cummins, T.R., and Waxman, S.G. 2003. Modulation of the cardiac sodium channel NaV1.5 by fibroblast growth factor homologous factor 1B. *J Biol Chem*. 278(2):1029-1036.

Mantegazza M., Yu F. H., Catterall W. A. and Scheuer T. 2001. Role of the C-terminal domain in inactivation of brain and cardiac sodium channels. *Proc Natl Acad Sci,* 98(26):15348-15353.

Musa, H., Kline, C.F., Sturm, A.C., Murphy, N.,…, and Mohler, P.J. 2015. SCN5A variant that blocks fibroblast growth factor homologous factor regulation causes human arrhythmia. *Proc Natl Acad Sci*. 112(40):12528-12533.

Sarhan M. F., Tung C. C., Petegem F. V., and Ahern C. A. 2012. Crystallographic basis for calcium regulation of sodium channels. *Proc Natl Acad Sci.* 109(9):3558-3563.

Shandell, M.A., Quejada, J.R., Yazawa, M., Cornish, V.W., and Kass, R.S. 2019. Detection of NaV1.5 conformational change in mammalian cells using the noncanonical amino acid ANAP. *Biophys J*. 117(7):1352-1363.

Shen, H., Zhou, Q., Pan, X., Li, Z., Wu, J., and Yan, N. 2007. Structural of a eukaryotic voltage-gated sodium channel at near-atomic resolution. *Science*. 355(6328):eaal4326.

Wang, C., Hennessey, J.A., Kirkton, R.D., Wang, C.,…, and Pitt, G.S. 2011. Fibroblast growth factor homologous factor 13 regulates Na+ channels and conduction velocity in murine hearts. *Circ Res*. 109:775-782.

Wang, C., Chung, B.C., Yan, H., Lee, S.Y., and Pitt., G.S. 2012. Crystal structure of the ternary complex of a NaV C-terminal domain, a fibroblast growth factor homologous factor and calmodulin. *Structure*. 20(7):1167-

1176.

Wang, C., Chung, B.C., Yan, H., Wang, H.G., Lee, S.Y., and Pitt, G.S. 2014. Structural analyses of Ca2+/CaM interaction with NaV channel C-termini reveal mechanisms of calcium-dependent regulation. *Nat Commun*. 5:4896.

4.7 Supplementary Figure

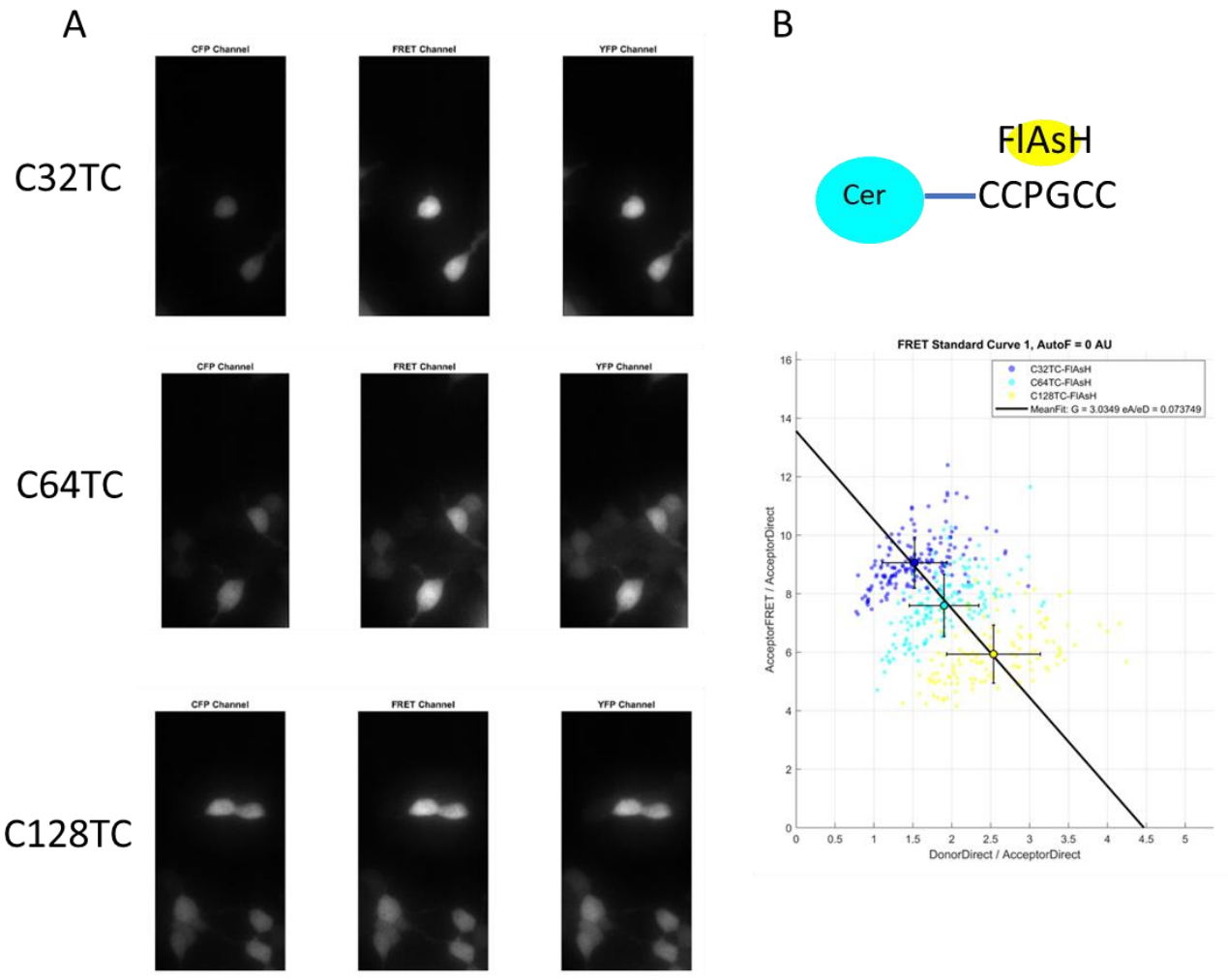

Figure S4.1: Control constructs of Cerulean fused with TC tag at varying linker
(A) Exemplary FRET images of 3 control constructs, Cerulean fused with TC of varying Glycine linker length-32, 64 and 128 residues. Images were shown from Donor, FRET, and Acceptor channels accordingly. (B) FRET efficiencies reduced with Glycine linker lengths. The longer length means the larger distances between Donor and Acceptor fluorophores.

Chapter 5: Conclusions and Future Directions

Na_V channels play a significant role in the regulation of cardiomyocyte excitability. Abnormalities in the channel function could lead to cardiac diseases. Na_V channel activation upon membrane depolarization is followed shortly by its fast inactivation. This inactivation is crucial in limiting the late I_{Na} that sustains over a long period. An incomplete inactivation results in elevated late I_{Na}, which leads to a prolonged AP duration and a predisposition to arrhythmia. Na_V channel inactivation is a complicated process involving multiple parts of the channels and many auxiliary subunits. To fully understand the fast inactivation mechanism, insights into the mechanism of individual components are needed. So far, the Na_V channel auxiliary subunit iFGF mechanism of regulation remains elusive. The interplays between different parts of the channels during inactivation are also unexplored.

In this thesis, I successfully determined the molecular mechanism of iFGF regulation of cardiac $Na_V1.5$ inactivation. I discovered that iFGFs modulate VSD-IV activation and the interactions between the Na_V CTD and III-IV linker. I demonstrated the significance of VSD-IV as a signaling hub for the regulation of Na_V channel inactivation gating. Other factors like the NaV β-subunit can also modulate this hub. I uncovered the specific regulation of VSD-IV activation by different iFGF, which directly affects the composition of fast inactivation. The earlier completion of VSD-IV activation leads to the inhibition of the slower component of fast inactivation. Then, I demonstrated the implications of an alteration in iFGF isoform, an increase in FGF12A expression observed in heart failure (HF) patients. This discovery provides a new paradigm of HF pathophysiology since FGF12A exhibits a natural ability to prevent late I_{Na}. Its expression can also modulate the pharmacological response of a specific late INa inhibitor and should be accounted for in targeted drug therapy. Lastly, I developed a new tool to investigate the interplay between different components involved in Na_V channel inactivation. I can determine the interactions between the Na_V channel inactivation gate on the

III-IV linker and CaM and FGF12B bound to the Na_V CTD. We presented the novel FlAsH-based FRET assay, utilizing the Tetracysteine (TC) tag for fluorescent labeling on the $Na_V1.5$ III-IV linker without disrupting its function. This new tool enabled us to explore the proposed model of Na_V channel inactivation under various conditions.

I hope that our discovery will fill in the knowledge gap of the intricate inactivation process. The mechanistic details of iFGF regulation of $Na_V1.5$ inactivation could serve as a molecular basis for the more elaborate model of Na_V channel macromolecular complex. I hope that our newly developed tool for studying Na_V channel inactivation dynamics will help propel the discovery of new knowledge that will guide us toward more efficient targeted treatment.